Carbon Nanotube Substrates for Tissue Engineering Applications

Analysis of surface nanotopography, cellular adhesion, and elasticity.

Dissertation

zur Erlangung des
naturwissenschaftlichen Doktorgrades
(Dr. rer. nat.)
der
Mathematisch-Naturwissenschaftlichen Fakultät
der
Rheinischen Friedrich-Wilhelms-Universität Bonn

vorgelegt von
Izabela Firkowska
aus Polczyn Zdroj, Polen

Bonn, 2008

Angefertig mit Genehmigung der Mathematisch-Naturwissenschaftlichen Fakultät der Rheinischen Friedrich-Wilhelms-Universität Bonn.

Referent: Prof. Dr. Michael Giersig
Korreferent: Prof. Dr. Manfred Fiebig

Tag der Promotion: 18.12.2008

Erscheinungsjahr: 2009

To Nicolas

Research is to see what everybody else has seen,
and to think what nobody else has thought.

(Albert Szent-Gyorgi)

Abstract

The present study investigates the applicability of multiwalled carbon nanotubes in creating novel nanostructured matrices exhibiting biomimetic designed features. The thus produced CNT-based constructs were employed to gain a deeper insight into the cellular response to nanoscale structures, especially to effects resulting from the local topography.

The first part of the work comprises the mechanical characterization of the CNTs matrices by means of nanoindentation and nanoscratch experiments, revealing a good mechanical stability of the MWNT-based polymer matrices.

The biocompatibility of the MWNTs constructs and cell-matrix surface interaction was assessed using human osteoblast-like cells. In general, osteoblasts were found to adhere and proliferate on all nanostructured matrices. The observed increase of osteoblastic metabolic activity after incubation on CNTs matrices proved their capability to support long-term survival of osteoblast cells and excluded the toxic impact of carbon nanotubes on cell viability. Furthermore, results from immunofluorescence staining revealed the improved cell adhesion capacity to nanostructured matrices and clearly showed the sensitivity of the cell to physical features at the nanoscale.

The atomic force microscopy was applied to investigate the cytomechanical properties of osteoblast cells cultured on diverse CNT matrix topographies. Experimental data showed that cell adhesion and therefore the elastic modulus of the cells are affected by the regularity of the topography, i.e., regular topography contributed to increased Young's modulus, whereas irregular one led to decreased cell stiffness.

Concluding, it could be shown that carbon nanotubes can be effectively used to fabricate various nanoscale topographies, which in turn have a powerful influence on osteoblasts behavior. The results furthermore indicate that carbon nanotubes can mimic nanofeatures of the native extracellular matrix and may therefore find an application in the design of new biomaterials for tissue engineering.

Contents

LIST OF SYMBOLS AND ABBREVIATIONS

AFM	Atomic force microscopy
BSA	Bovine serum albumin
CEAP	2-carboxyethylphosphonic acid
CNTs	Carbon nanotubes
COOH	Carboxylic group
CP	Calcium phosphate
CSK	Cytoskeleton
HOB-C	Human hipbone osteoblast cells
E	Young's modulus
E_r	Reduced modulus
ECM	Extracellular matrix
EDX	Energy dispersive X-ray spectroscopy
FAs	Focal adhesions
H	Hardness
HA	Hydroxyapatite
k	force constant
LbL	Layer-by-Layer
MTT	Tertazolium salt
MWNTs	Multiwalled carbon nanotubes
MWNT-COOH	Oxidized multiwalled carbon nanotubes
MWNT-PAH	PAH-functionalized multiwalled carbon nanotubes
NH_2	Amine group
NPs	Nanoparticles
NSL	Nanosphere lithography
PAH	Poly(allylamine hydrochloride)
PDDA	Poly(diallyldimethyl-ammonium chloride)
PEI	Polyethyleneimine
PECVD	Plasma enhanced chemical vapor deposition
PLGA	poly (lacitc-co-glycolic acid)
PLLA	poly-L-lactc acid
PMMA	Poly(methyl methacrylate)
PS	Polystyrene
PSS	Poly(styrenesulfonate)
RIE	Reactive ion etching
SEM	Scanning electron microscopy
SWNT	Singlewalled carbon nanotube

TE	Tissue engineering
TEM	Transmission electron microscopy
THF	Tetrahydrofuran
VACNTs	Vertically aligned carbon nanotubes
z_c	Contact point
δ	Indentation
μ	Coefficient of friction
ν	Poisson's ratio

Chapter 1
Introduction

Nowadays, nanotechnology poses a new frontier in science and technology. The essence of this highly multi- and interdisciplinary field is the ability to work at atomic and molecular levels and to create structures or devices with a fundamentally new molecular organization. One of the numerous fields, which have benefited from the fast evolution of nanotechnology and in particular from the discovery of nanoscaled materials, is tissue engineering (TE); a field that aims at the development of biological substitutes (artificial extracellular matrices, also called scaffolds) that restore, maintain or improve tissue function [1].

Over the years, the artificial scaffolds, designed to support cell and tissue regeneration, have traditionally been focused on a macroscopic level. Their aim was to match the properties similar to natural tissues without reconstructing the nano-scale features that were observed in native tissues. All tissues of the human body, however, contain differentiated cells living in an extracellular matrix (ECM), which shows hierarchical organization from nano- to macroscopic length scale; therefore, it is obvious that cells are naturally accustomed to interact with nanometer length-scale elements [2]. For that reason, the nanoscale surface features are considered to be a key determinant of the cellular response. It is believed that the topography, engineered with nanoscale structural elements analogous to dimensions present in the extracellular matrix, is critical for the proper function of each specialized tissue. The new discoveries in nanotechnology and the new ability of engineering enable the material scientists and engineers to design and fabricate novel scaffolds by incorporating nanoscale features, thus imitating characteristics of the natural ECM. However, to accomplish the construction of more biomimetic cellular environments, the fundamental design principles that determine how cells and tissues form and function as hierarchical assemblies of nano- micrometer-scale components must first be understood. Accordingly, great attention has been focused on cell-material surface interactions, with particular interest on those, whose properties try to mimic the dimensions present in the natural tissue. In the last years, several studies have shown a powerful influence of nanoscale topography on cellular behavior, starting from changes in cell adhesion, spreading, and/or cytoskeletal organization to the regulation of gene expression [3–5]. Moreover, it has been

demonstrated that nano-scaled topography may induce various responses of the same cell type independent of the underlying material chemistry [6,7].

The nanoscale structure of the ECM provides a natural net of complex nanofibers, which support and guide the cell behavior. Each fiber conceals clues that pave the way for the cell to form tissues as complex as bone, heart, and liver [8]. Until recently, an ECM-mimicking fiber with a nanoscale diameter has been the missing constituent in cell scaffold design [9]. One of the most promising nanometer-sized cylinders that could imitate nanofibers present in native ECM, are carbon nanotubes (CNTs). Zhao *et al*. [10], for example, have shown the potential of nanotubes to mimic the role of collagen, the major component of the ECM protein in the human body, and serve as a scaffold for growth of hydroxyapatite. Apart from nanoscale dimensions, CNTs possess numerous physical, chemical, and mechanical properties, which make them distinct from other nanofibrous materials used for biological applications [11]. In particular, their extremely high strength, lightness, and electrical conductivity enable the creation of biomimetic constructs with highly predictable physical properties. Moreover, the latest expansion and availability of carbon nanotube's chemical modification and bio-functionalization methods [12] make it possible to generate CNTs-based scaffolds with bioactive surfaces, i.e. positively interacting with cells, including enhanced cell adhesion, proliferation, migration, and differentiated function. Although CNTs do not exhibit a biodegradable nature, on contrary to nanofibrous polymers, i.e. PGA, PLLA, and PLGA, frequently used for scaffold fabrications [1], the above-mentioned advantages counterbalance this drawback.

The main objective of this study was to explore the use of multiwalled carbon nanotube constructs (matrices) as a simplified model system to study and gain insights into cellular responses to a nanoenvironment, with particular interests in the effects of local topographies. Since the exploitation of the carbon nanotubes in biomimetic construct fabrication requires their chemical functionalization, both covalent and non-covalent surface functionalization strategies were employed here. Using oxidation and polymer wrapping methods, two differently modified CNTs, either functionalized with carboxyl or amine groups, were obtained. The presence of these groups allowed a further processing of CNTs into polymer matrices and helped to explore the influence of the CNT's surface chemistry on cellular behavior.

Aiming at the creation of unique architectures comprising biomimetic characteristics, MWNT matrices were engineered using various techniques. Thus, in the frame of this thesis, we present a novel concept for the fabrication of highly ordered, lightweight carbon nanotube constructs by means of nanosphere lithography (NSL) and electrostatic layer-by-layer (LbL) self–assembly. Additionally, vertically aligned carbon nanotubes arrays (VACNTs) were produced using chemical vapor deposition (CVD).

The ideal scaffolds should not only posses biomimetic properties of ECM but also provide mechanical support for the growing tissue during *in vitro* or *in vivo* development. From this point of view, the mechanical properties of the CNT-based scaffolds are one of the most important

factors, which have to be evaluated. In this work we used nanoindentation tests to determine the hardness and Young's modulus of the matrices.

The main concern, regarding the use of carbon nanotubes in tissue engineering, is their cytotoxicity. There are several studies that emphasize the harmful effect of carbon nanotubes on cell proliferation and adhesive ability [13,14]. However, there are few reports, which have demonstrated the biocompatibility of CNT-based substrates with various cell cultures [15,16]. Taking these contradictory opinions regarding the toxicity of carbon nanotubes into account, the CNT-based matrices were tested on living organisms (i.e. human osteoblast cells) aiming to verify their biological compatibility by means of metabolic activity assay and cell proliferation studies.

In order to explore and understand the impact of nanoscale architectures and CNTs surface chemistry on cellular behavior, various characterizations and experiments have to be performed. Accordingly, the third part of this work focuses on the biological characterization of CNT-based matrices including protein adsorption, cell proliferation, focal adhesion formation and cytoskeleton organization. Considering the fact that the enhanced protein adsorption improves cell adhesion and function [17], the dependence of the nanoscaled architecture and the surface chemistry of carbon nanotubes on serum protein adsorption was studied. Furthermore, the immunoflueorescence staining was used to investigate the effect of surface periodicity on the distribution of the cytoskeletal elements and focal contacts. Finally, we used atomic force microscopy (AFM) as a new tool to investigate the biocompatibility of produced CNT-based constructs by studying the adhesion behavior of osteoblast-like cells.

References

[1] P.X. Ma, "Biomimetic materials for tissue engineering". *Adv Drug Deliv Rev*. **60**(2), 184 (2008)

[2] S. Weiner, H.D. Wagner, "The material. Bone: Structure-mechanical function. Relations". *Annu. Rev. Mater. Sci.* **28**, 271 (1998)

[3] M.J. Dalby, M.O. Riehle, D.S. Sutherland, H. Agheli, and A.S.G. Curtis, "Fibroblast response to a controlled nanoenvironment produced by colloidal lithography". *J. Biomed. Mat. Res*. **69A**, 314 (2004)

[4] R.G. Flemming, C.J. Murphy, G.A. Abrams, S.L. Goodman, and P.F. Nealey, "Effects of synthetic micro- and nano-structured surfaces on cell behavior". *Biomaterial*s **20**, 573 (1999).

[5] M.J. Dalby, M.O. Riehle, S.J. Yarwood, C.D.W. Wilkinson, and A.S.G. Curtis, "Nucleus alignment and cell signaling in fibroblasts: response to a micro-grooved topography". *Experimental Cell Research* **284**, 274 (2003)

[6] A.-S. Andersson, F.Blasckhed, A.von Euler, A Richter-Dahlfors, D. Sutherland, B. Kasemo, "Nanoscale features influence epithelial cell morphology and cytokine production". *Biomaterials* **24**, 3427 (2003)

[7] E.K. Yim, R.M. Reano, S.W. Pang, A.F. Yee, C.S. Chen and K.W. Leong, "Nanopattern-induced changes in morphology and motility of smooth muscle cells". *Biomaterials* **26**, 5405 (2005)

[8] M.M. Stevens, J.H. George, "Exploring and Engineering the Cell Surface Interface". *Science* **310**, 1135 (2005)

[9] G. L. Bowlin, "A new spin of scaffolds". *Materials Today* **7**(5), 64 (2004)

[10] B. Zhao, H. Hu, S.K. Mandal, R.C. Haddon, "A Bone Mimic Based on the Self-Assembly of Hydroxyapatite on Chemically Functionalized Single-Walled Carbon Nanotubes". *Chem. Mater*. **17**, 3235 (2005)

[11] B.S. Harrison, A. Atala, "Carbon nanotube applications for tissue engineering". *Biomaterials* **28**, 344 (2007)

[12] W. Yang, P. Thordarson, J.J. Gooding, S.P. Ringer and F. Braet, "Carbon nanotubes for biological and biomedical applications". *Nanotechnolgy* **41,** 412002 (2007)

[13] C.-W. Lam, J.T. James, R. McCluskey, R.L. Hunter, "Pulmonary toxicity of single-wall carbon anotubes in mice 7 and 90 days after intratracheal instillation. *Toxicological Sciences* **77**, 126 (2004)

[14] D. Cui, F. Tian, C.S. Ozkan, M. Wang, H. Gao, "Effect of single wall carbon nanotubes on human HEK293 cells". *Toxicology Letters* **155**, 73 (2005)

[15] R.L. Price, K.M. Haberstroh, T.J. Webster, "Improved osteoblast aviability in the presence of smaller nanometre dimensioned carbon fibers". *Nanotechnology* **15**, 892 (2004)

[16] H. Hu, Y.C. Ni, V. Montana, R.C. Haddon, V. Parpura, "Chemically functionalized carbon nanotubes as substrates for neuronal growth". *NanoLetters* **4**, 507 (2004)

[17] Y. Arima, H. Iwata, "Effects of surface functional groups on protein adsorption ans subsequent cell adhesion using self-assembled monolayers". *J. Mater. Chem.* **17**, 4079 (2007)

Chapter 2
Background

2.1 Carbon nanotubes

The first carbon fibers of nanometer dimensions were discovered in 1976 by Endo [1] who synthesized carbon filaments of 7 nm in diameter using a vapor-growth technique. The filaments he produced, however, were not recognized as carbon nanotubes (CNTs) until Sumio Iijima's report in 1991 [2], which brought CNTs to the awareness of the scientific community. Since that time, carbon nanotubes have emerged as one of the most intensively investigated nanomaterial.

The structure of carbon nanotubes can be visualized as a rolled-up graphene sheet (Fig. 2.1). Based on the orientation of the tube axis with respect to the hexagonal lattice the structure of a nanotube can be completely specified by its chiral vector $\vec{C}_h$, which is denoted by the chiral indices (n, m). The chiral vector, also know as the roll-up vector is given by:

$$\vec{C}_h = n\vec{a}_1 + m\vec{a}_2 \qquad \textbf{(Eq.2.1)}$$

The integers (n, m) are the number of steps along the zig-zag carbon bonds of the hexagonal lattice, with $\vec{a}_1$ and $\vec{a}_2$ the unit vectors.

The bonding in carbon nanotubes is essentially sp^2, similar to the bonding in graphite. However, the circular curvature in CNTs cause quantum confinement and σ-π rehybridization in which three σ bonds are slightly out of plane; for compensation, the π orbital is more delocalized outside the tube [3]. This rehybridization of a structural feature, together with the π electron confinement make the nanotubes mechanically stronger, electrically and thermally more conductive, and chemically and biologically more active than graphite.

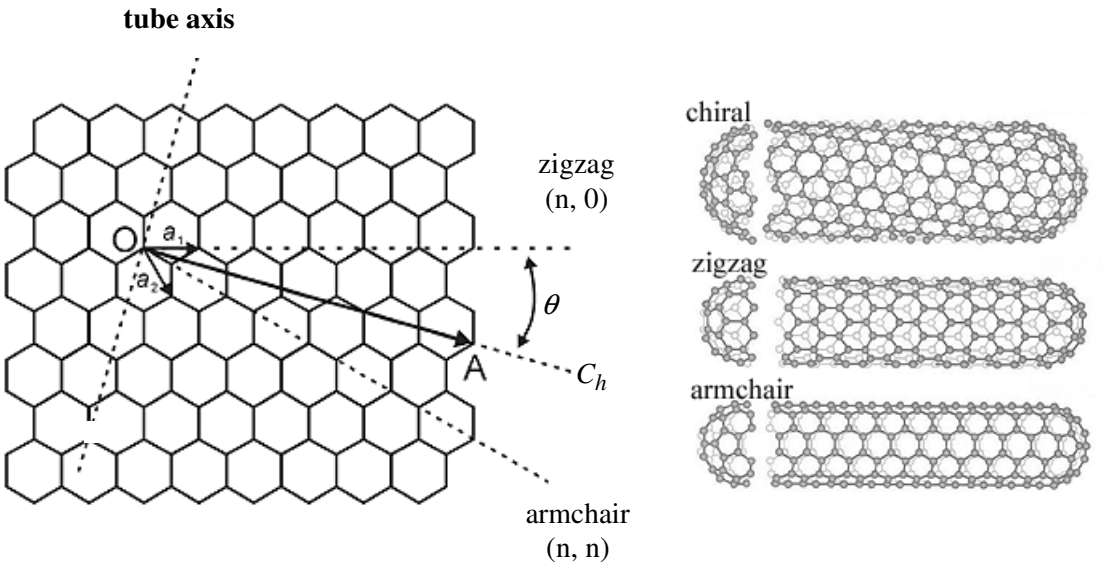

Figure 2.1: *Schematic of a two-dimensional graphene sheet showing lattice vectors a_1 and a_2, and the chiral vector C_h, θ is the chiral angle. By rolling a graphene sheet in different directions typical nanotubes can be obtained: armchair (n,n), zigzag (n, 0), and chiral ($n \neq m$) [3].*

Basically, there are two forms of CNTs: singlewalled and multiwalled. Singlewalled carbon nanotubes (SWNTs) consist of a single rolled-up graphene sheet with diameters ranging from 0.4 to 3 nm. SWNTs may be either metallic or semiconducting, depending on their chirality.

Multiwalled carbon nanotubes (MWNTs) (Fig. 2.2) are composed of a concentric arrangement of numerous SWNTs, often capped at their ends by one half of a fullerene-like molecule. The distance between two layers in MWNTs is 0.34. Multiwalled nanotubes can reach diameters of up to 200 nm [3].

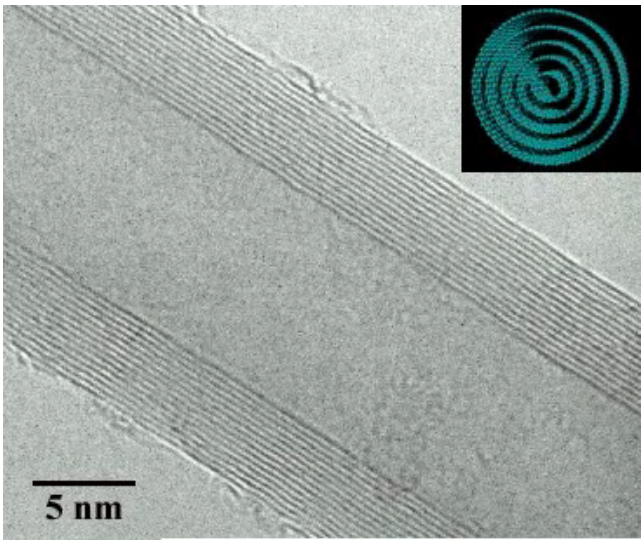

Figure 2.2: *High-resolution transmission electron-microscope image of MWNTs used in this study. (www.endomoribu.shinshu-u.ac.jp).*

2.1.1 Production

CNTs can be produced by different kinds of techniques. In general, there are three well-established methods for the synthesis of CNTs (Table 2.1). A brief description of these techniques is given below.

Chemical Vapor Deposition (CVD): This process involves the decomposition of hydrocarbons (methane, acetylene, ethylene, etc.) over catalyst particles (e.g. Co, Ni, Fe), which are deposited at predefined locations on the substrate. Typically, the hydrocarbons are decomposed in a tube reactor at temperatures ranging from 550 ^{o} to 750 ^{o}C. The synthesis of CNTs is often plasma enhanced (PECVD). Depending on the growth conditions (catalyst material, gas, temperature, flow-rate, and synthesis time), MWNTs range from $10 - 400$ nm in diameter and $0.1 - 50$ µm in length [4]. Additionally, using PECVD, excellent alignment and position control on the nanoscale [5] as well as control over the diameter and the growth rate [6] can be achieved.

Carbon Arc-Discharge: This technique utilizes two carbon electrodes to generate an arc by direct current (dc). The electrodes are kept under an inert gas atmosphere (argon, helium), which increases the speed of carbon deposition. The arc-discharge method produces high-quality SWNTs and MWNTs. However, contrary to MWNTs, SWNTs can only be grown in the presence of a catalyst. A subsequent separation of CNTs from the soot and metal particles is necessary and causes impurities in the final product. The major contaminants are amorphous carbon, fullerenes, catalysts and graphite particles. The CNTs produced by arc-discharge are higly crystalline with diameters in the range of $2 - 20$ nm and a length of several micrometers for MWNTs [7] and diameters of $1.2 - 1.5$ nm and lengths reaching up to 20 µm for SWNTs [3].

Tab. 2.1: Summary and comparison of three most common CNT synthesis methods

METHOD	CVD	LASER ABLATION	ARC-DISCHARGE
PIONEER	Iijima (1991) [2]	Yacaman et al. (1993) [8]	Guo et al. (1995) [9]
YIELD	> 75 %	< 75 %	< 75 %
SWNTs or MWNTs	Both	Both	Both
ADVANTAGES	simple, low temperature, high purity, large-scale production, aligned growth possible	relatively high purity, room-temperature synthesis	simple, inexpensive, high quality nanotubes
DISADVANTAGES	synthesized CNTs are usually MWNTs, defects	method limited to the lab-scale, crude product - purification required	high temperature, purification required, tangled nanotubes

Laser ablation: In this method, a pulsed or continuous laser is used to vaporize a target consisting of a mixture of graphite and metal catalysts (e.g. Co, Ni), in the presence of helium or argon gas. The laser-produced MWNTs are relatively short (ca. 300 nm) with the inner diameter in the range of 1.5 – 3.5 nm, where the SWNTs have length from 5 – 20 μm, and diameter between 1 – 0.4 nm [3].

The methods described above differ with regard to the quality and the kinds of synthesized CNTs. All of them have advantages and disadvantages. At present, however, the foremost issue has become the selection of the best method for commercial applications. In view of the fact that large-scale production of CNTs is becoming a major factor, most industries are opting for the CVD technique.

2.1.2 Mechanical properties

The extraordinary mechanical properties of carbon nanotubes arise from σ bonds between the carbon atoms. Experimental measurements together with theoretical calculations show that nanotubes exhibit the highest Young's modulus (elastic modulus *E*) and tensile strength among known materials. As reported by Overney *et al*. [10], the elastic modulus of singlewalled CNTs can be up to 1.5 TPa. The ultimate strength of CNTs, ranging from 13 to 150 GPa, surpasses that of materials well-known for their high tensile strength, such as steel and synthetic fibers [11,12]. Unlike electrical properties, Young's modulus of CNTs is independent of tube chirality, although it depends on tube diameter.

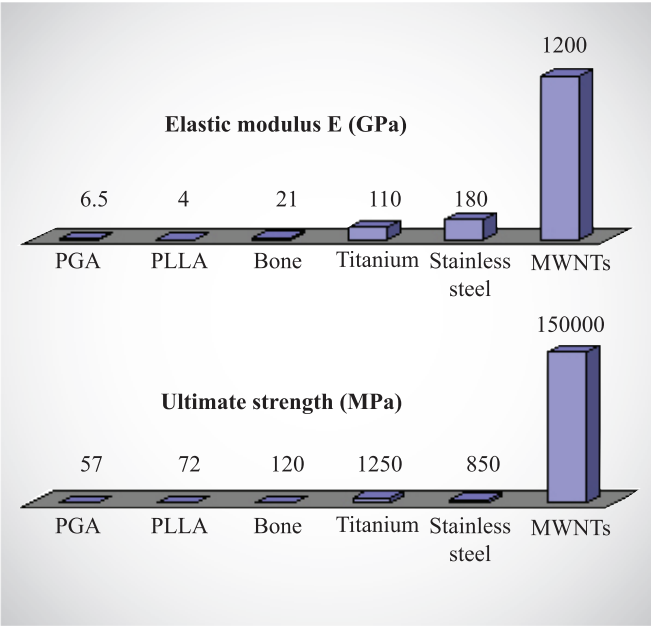

Figure 2.3: *Illustration of the elastic modulus and strength of carbon nanotubes [3] and common tissue engineering materials: PGA, PLLA [14], bone, titanium, steel [15].*

The elastic response of a nanotube to deformation is also outstanding. Both, theory and experiment show that CNTs can sustain up to 15 % of tensile strain before fracture. As shown by Iijima *et al*. [13], CNTs are very flexible with a reversible bending up to angles of 110 ^{o} and 120 ^{o} for MWNTs and SWNTs, respectively.

The extraordinary mechanical properties of CNTs have met great interest in the application of nanotubes in tissue engineering. Properties like the high tensile strength and excellent flexibility give them superiority over popular materials used in TE (PGA, PLLA, titanium, steel) and make them ideal candidates for the production of lightweight, high-strength bone materials. For comparison, Fig. 2.3 shows the elastic modulus and strength of CNTs, bone, and several other common materials used in bone-tissue engineering.

2.1.3 Electrical properties

The electronic structure of carbon nanotubes is determined by their chirality and diameter, or, in other words, by their chiral vector $\overrightarrow{C_h}$. CNTs are conductive if the integers in Eq. 2.1 are: $n = m$ (armchair) and $n - m = 3i$ (where i is an integer). In all other cases, they are semiconducting. The energy band gap E_g for semiconducting nanotubes is given by [3]:

$$E_g = \frac{2\gamma_o a_{c-c}}{d} \quad , \qquad \textbf{(Eq. 2.2)}$$

where γ_o = 2.45 eV is the nearest-neighbour overlap integral [16], $a_{c\text{-}c}$ the nearest neighbor C-C distance (~ 1.42 Å), and d is the diameter of the nanotube. Thus, the E_g of a 1 nm wide semiconducting tube is roughly 0.7 eV to 0.9 eV [3].

It has been experimentally verified that SWNTs and MWNTs behave like quantum wires because of the confinement effect on the tube circumference [17,18]. The conductance for a carbon nanotube is given by [1]:

$$G = G_0 M = \left(2\frac{e^2}{h}\right) M \, , \qquad \textbf{(Eq. 2.3)}$$

where $G_0 = (2e^2/h) = (12.9\ k\Omega)^{-1}$ is the quantum unit of conductance. M is the apparent number of conducting channels including electron-electron coupling and intertube coupling effects in addition to intrinsic channels (M equals 2 for perfect SWNTs), e is the electron charge, and h is Planck's constant.

According to Frank *et al.* [17] the electrical current, which could be passed through a MWNT corresponds to a current density $\vec{j}$ in excess of 10^7 Acm^{-2} (for comparison, $\vec{j}$ for superconductors is typically of the order of 10^5 Acm^{-2}).

2.1.4 Chemical properties

Small radius, large specific surfaces, and σ-π rehybridization make carbon nanotubes very attractive for chemical and biological applications because of their strong sensitivity to chemical or environmental interactions [3].

The chemical functionalization of carbon nanotubes is a very promising target since it can improve solubility, processibility, and moreover allows the exceptional properties of carbon nanotubes to be combined with those of other types of materials. Up to now, several methods for the functionalization of CNTs have been developed. These methods include covalent functionalization of sidewalls, noncovalent exohedral functionalization (for example with surfactants and polymers), endohedral functionalization, and defect functionalization (see Fig. 2.4). Chemical groups on CNTs can serve as anchor groups for further functionalization, e.g. with biological and bio-active species such as proteins or nucleic acids [20,21]. This bioconjugation is especially attractive for biomedical applications of carbon nanotubes.

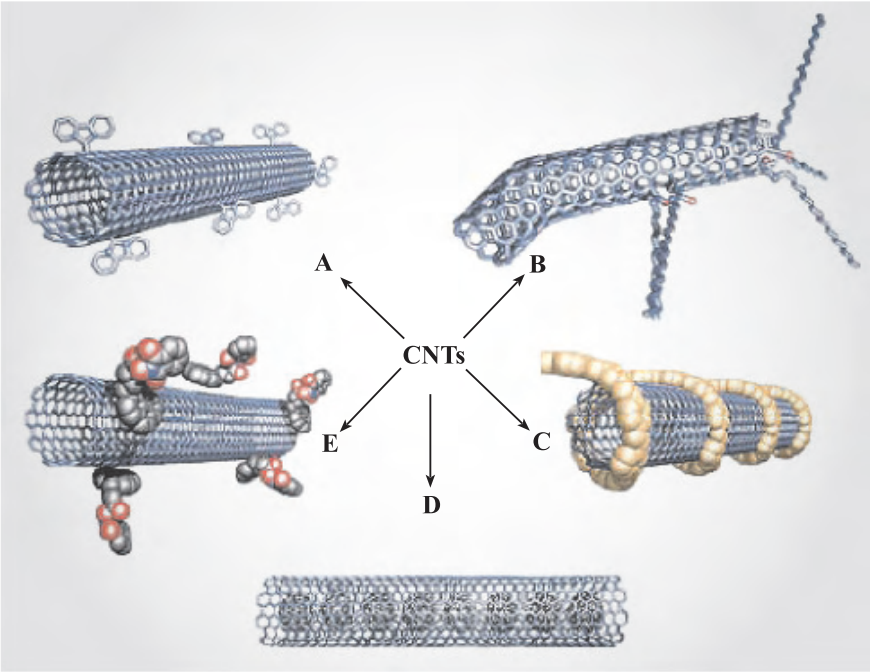

Figure 2.4: *Various functionalizations of carbon nanotubes: (A) covalent sidewall functionalization, (B) defect-group functionalization, (C) noncovalent exohedral functionalization with polymers, (D) endohedral functionalization with, for example, C_{60}, (E) noncovalent exohedral functionalization with surfactants [19].*

2.2 Carbon nanotubes in tissue engineering

Tissue engineering is an interdisciplinary field, which develops biological substitutes (artificial extracellular matrices, also named scaffolds) capable of repairing or regenerating the functions of a damaged tissue. In order to engineer the materials that will support the structure and function of human tissue, a deep understanding of the cell and extracellular matrix (ECM) interactions, which take place within tissues is required. Up to now, most tissue engineering studies have focused on the investigation and creation of macrolevel structures with non-biologically inspired topographies, i.e. structures that are rough at the micron scale, yet smooth at the nanoscale. However, as presented in Fig. 2.5, biological structures formed during tissue development show hierarchical organization from the nano to the macro-length scale. Therefore, it is obvious that the length-scale variation in the extracellular environment plays a crucial role in determining cellular behavior and that cells are naturally accustomed to interact with nanometer length-scale features [22].

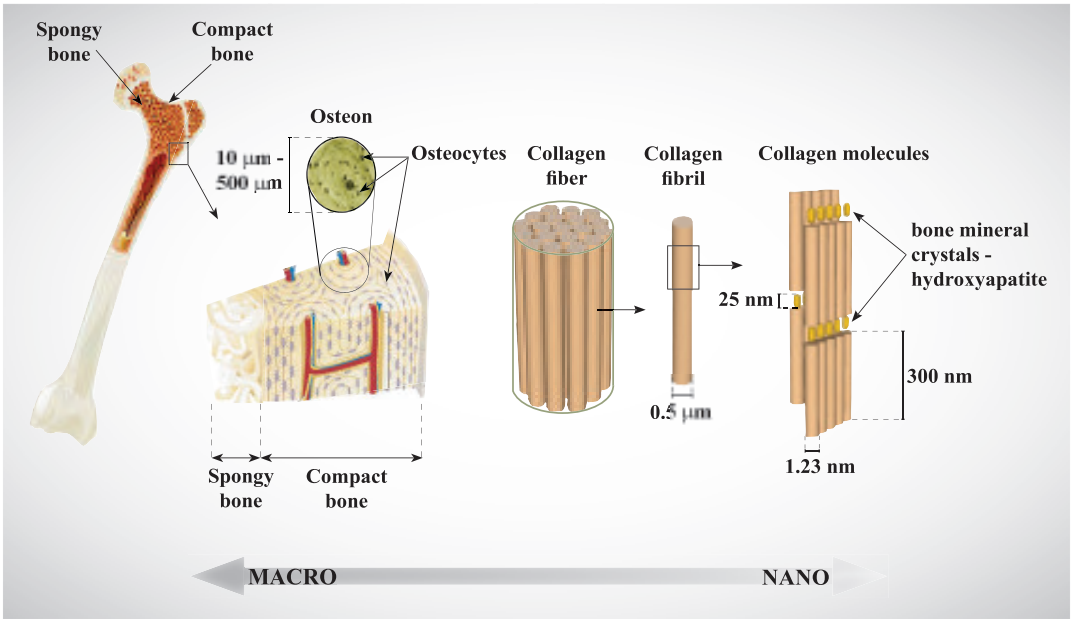

Figure 2.5: *Scheme illustrating the complex hierarchical bone structure [23]. Bone mineralizes to form a calcified outer compact layer, which contains many cylindrical Havaresian systems or osteons. The osteocytes within the osteons are surrounded by a dense network of aligned collagen I fibrils. Fibrils, in turn, are composed of individual collagen molecules oriented parallel to each other. Such packed molecules provide templates for the self-assembly of hydroxyapatite crystals.*

The ECM, which supports and guides cellular behavior, exhibits a rich architecture of nanoscale features like interconnecting pores, ridges and fibers which naturally bind and support cells throughout human tissues [23]. For example, the type I collagen fibrils, one of the major components of the bone, are composed of hydroxyapatite crystals and collagen molecules, where the crystals have an average dimension of about 50 nm, and the molecules have an average of 300 nm in length and 1.23 nm in diameter [24]. Additionally, numerous cellular features have

nanoscaled dimensions like, for example, cell transmebrane receptors (integrins), which contain a globular head of diameter 8 − 14 nm with two rod-like tails extending 14 − 17 nm [25].

Taking into account the presence of nano-features in ECM, it is essential to create the structures with biologically inspired nanoscale dimensions in order to control cellular behavior and subsequently, tissue development. Therefore, this fact has given rise to the use of nanomaterials and nanofabrication techniques for tissue engineering.

One of the most promising nanomaterials, which have a great potential for multiple uses in tissue engineering, are the carbon nanotubes. The appeal of CNTs arises from the fact that they have a structure that can be tailored to mimic closely the nano-scale of native ECM (i.e. collagens). Additionaly, their unique electrical properties, high mechanical strength, excellent flexibility, and low density, can result in creation of constructs with highly-predictable biological and physical properties. More details and examples of applications of carbon nanotubes in tissue engineering are given below.

2.2.1 Matrix enhancement

The artificial matrix plays a very important role in tissue engineering. It is responsible for defining the space the engineered tissue occupies and for aiding the process of tissue development [26]. One of the few requirements that the matrix has to fulfill is mechanical stability, which is crucial for maintaining the predesigned tissue structure. Mechanical stability mainly depends on the selection of the biomaterial and the architectural design of the matrix. Although polymers, such as PLLA (polyl-L-lactide acid) or PLGA (poly(lactic-co-glycolic acid)), are the primary materials for matrices in various tissue engineering applications, but they lack the necessary mechanical strength (see Fig 2.3). Additionally, they cannot be functionalized as easily as carbon nanotubes.

The extraordinary mechanical properties of carbon nanotubes make them very attractive and promising as reinforcing fillers for the production of a new generation of tissue matrices. The functional groups, which can be readily introduced into the CNTs' surface, greatly enhance their connection with a great variety of polymeric matrices, thus improving the mechanical properties of nanocomposites. Data revealing that carbon nanotubes dispersed in a polymer significantly improve the mechanical properties of the composite already exist [27-29]. Up to now, carbon nanotubes have been put into a host of different synthetic polymers as well as into biopolymers. Carbon nanotubes merged with chitosan, for example, showed a significant enhancement in the mechanical strength of the composite [30]. By incorporation of only 0.8 wt% of CNTs into the chitosan matrix, the mechanical properties of the nanocomposite, including Young's modulus and tensile strength, were improved by about 93 % and 99 %, respectively.

Apart from polymer enhancement, carbon nanotubes have also been used to reinforce ceramic matrices. Gao *et al.* [31] successfully fabricated CNTs/$BaTiO_3$ composites, where the addition of 1 wt% of CNTs increased the fracture toughness by about 240 %. Using plasma-sprayed

techniques, CNTs have been uniformly distributed in a brittle hydroxyapatie (HA) bioceramic coating, improving the fracture toughness of the nanocomposite by 56 % [32].

The above-mentioned studies demonstrate that the mechanical properties of matrices can be significantly improved with CNTs. Moreover, the fact that the addition of very small amounts of CNTs is sufficient for matrix enhancement may counterbalance their nondegradable nature.

2.2.2 Cellular response to carbon nanotube-based matrices

Whereas mechanical reinforcement was the initial motivation of using carbon nanotubes, there is evidence that CNTs can accelerate and direct cell growth. Several *in vitro* studies have been conducted investigating the interaction between CNTs or nanocomposites and mammalian cells. It was shown that a collagen matrix with embedded SWNTs sustained a high cell viability of smooth muscle cells [33]. The work by Zanello *et al.* [34] examined the proliferation and function of osteoblast cells seeded onto five differently functionalized carbon nanotubes. This study showed that bone cells prefer electrically neutral CNTs, which sustained osteoblast growth and bone-forming functions. The follow-up study investigated the adhesion properties of osteoblast, fibroblast, neuron, and astrocyte cell on polycarbonate urethane/carbon nanotube (PU/CNT) nanocomposites [22]. The conducted experiments revealed that cell functions that contribute to glial scar-tissue formation (astrocytes) and fibrous-tissue encapsulation (fibroblast) decreased.

The possibility of using nanotubes as substrates for nerve cell growth and as probes of neural functions at the nanometer scale has been reported by Mattson *et al.* [35]. They showed that neurons, which were grown on CNTs functionalized with a bioactive molecule, 4-hydroxynonenal, developed multiple neurites and extensive branching. The ability to control the characteristics of neurite outgrowth also became possible by manipulating the charge carried by the functionalized carbon nanotubes. As shown by Hu *et al.* [36], neurons plated on positively-charged CNTs exhibited more numerous growth cones, longer neurite outgrowth, and more neurite branching in comparison with the neurons grown on negatively-charged nanotubes.

Carbon nanotubes have also been used to create electrically-conductive polymers and tissue matrices with the capacity to provide controlled electrical stimulation. It has been reported that current-conducting CNT/polymer composites promote various osteoblast cell functions. By applying alternating current to these nanocomposites, an increase in osteoblast proliferation by 46 %, and calcium deposition by 307 % has been observed [37]. This result suggests that CNT-based composites may be used to stimulate bone formation. Other studies have been directed toward exploiting the electrical properties of CNTs for the purpose of healing neurological and brain-related injuries. Gheith, *et al.* [38] have used electrically-conductive LbL-assembled, modified SWNT films to stimulate the neurophysiological activity of neural cells. Electrophysiological measurements showed that SWNT films can be used to electrically stimulate significant ion conductance in neuronal cells. This indicates a good electrical coupling between the LbL film and the neuronal cells in the lateral electrical configuration.

Although the above-mentioned studies mostly investigated cell adhesion and proliferation on randomly oriented nanotubes and CNT/polymers, carbon nanotubes can also be arranged into 3D matrices with well defined periodic architectures. Correa-Duarte *et al*. [39], for example, created unique 3D structures from aligned CNTs grown on a silicon substrate, which subsequently formed honeycomb-like polygons in an oxidation process. This 3D CNT-based structure showed a good biocompatibility, proven by the excellent proliferation of mouse fibroblasts. In a related study, Giannona *et al.* [40] investigated the influence of periodic arrays of vertically-aligned carbon nanotubes (VACNTs) on the behavior of osteoblast cells. The authors observed a significant enhancement in cell attachment and proliferation as well as an influence on the cells' shape and orientation due to the periodicity of the CNTs.

As pointed out previously, carbon nanotubes can be chemically functionalized in many different ways. This not only allows to combine but even to replace other types of materials with CNTs. For instance, Zhao *et al*. [41] demonstrated that adequately-functionalized carbon nanotubes can be used as a substitute for collagen to promote new bone growth. In this study, chemically-treated carbon nanotubes served as nucleation sites for the deposition of hydroxyapatite. The negatively charged groups on the CNTs led to a self-assembly of HA crystals reaching a thickness of 3 μm after 14 days of mineralization. Similar observations for hydroxyapatite mineralization onto carbon nanotubes have been reported by other researchers [32,42].

Considering recent publications, it can assumed that the use of carbon nanotubes for tissue engineering appears to be challenging but on the other hand potentially rewarding perspective to develop the next generation of engineered biomaterials.

References

[1] M. Endo, *PhD thesis*. Nagayo University, Japan (1978)

[2] S. Iijima, "Helical microtubules of graphitic carbon". *Nature* **354**, 56 (1991)

[3] M. Meyyappan, "Carbon nanotubes. Science and application". *CRS Press*: Boca Raton, FL (2005)

[4] Z.F. Ren, Z.P. Huang, J.W. Xu, J.H. Wang, P. Bush, M.P. Siegel, P.N. Provencio, "Synthesis of large arrays of well-aligned carbon nanotubes on glass". *Science* **282**, 1105 (1998)

[5] Z.P. Huang, D.L. Carnaham, J. Rybczynski, M. Giersig, M. Sennett, M., D.D Wang, J.G. Wen, K. Kempa, Z.F. Ren, "Growth of large periodic arrays of carbon nanotubes". Appl. Phys. Lett. **82**, 460 (2003)

[6] M. Chhowalla, K.B.K. Teo, C. Ducati, N.L. Rupesinghe, G.A.J. Amaratunga, A.C. Ferrari, D. Roy, J. Robertson, W.I. Milne, "Growth process conditions of vertically aligned carbon nanotubes using plasma enhanced chemical vapor deposition". *J. Appl. Phys.* **90**, 5308 (2001)

[7] T.W. Ebbesen, P.M. Ajayan, "Large scale synthesis of carbon nanotubes". *Nature*, **363**, 603 (1993)

[8] M. Jose-Yacaman, "Catalytic growth of carbon microtubules with fullerene structure". *Appl. Phys. Lett.* **62**, 202(1993)

[9] T. Guo, A. Nikolaev, A**.** Thess, D.T. Colbert, R.E. Smalley, "Catalytic growth of single-walled nanotubes by laser vaporization". *Chem. Phys. Lett.* **243**, 49 (1995)

[10] G. Overney, W. Zhong, D. Tomanek, "Structural rigidity and low frequency vibrational modes of long carbon nanotubes". *Z. Phys.* **27**, 93 (1993)

[11] M.F. Yu, B.S. Files, S. Arepalli, R.S. Ruoff, "Tensile loading of ropes of single wall carbon nanotubes and their mechanical properties". *Phys. Rev. Lett*. **84**, 5552 (2000)

[12] Z.W. Pan, S.S. Xie, L. Lu, B.H. Change, L.F. Sun, W.Y. Zhou, G. Wang, D.L. Zhang, "Tensile test ropes of very long aligned multiwall carbon nanotubes. *Appl. Phys. Lett*. **74**, 3152 (1999)

[13] S. Iijima. C. Brabec, A. Maiti, J. Bernholc, "Structural flexibility of carbon nanotubes". *J. Chem . Phys.* **104**, 2809 (1996)

[14] A.U. Daniels, M.K.O. Chang, K.P. Andriano, "Mechanical properties of biodegradable polymers and composites proposed for internal fixation of bone". *J. Appl. Biomat*. **1**, 57 (1990)

[15] H. Yuehuei, R.A. Draughn, "Mechanical testing of bone and the bone-implant interface". *CRC Press: Boca Raton, FL* (2000)

[16] T.W. Odom, J-L. Huang, P. Kim, C.M. Lieber, "Atomic structure and electricla properties of single-walled carbon nanotubes". *Nature* **391**, 62 (1998)

[17] S. Frank, P. Poncharal, Z.L. Wang, A. de Heer Walt, "Cabon nanotube quantum resistors". *Science* **280**, 1744 (1998)

[18] S. Sanvito, Y-K. Kwon, D. Tomanek, C. Lambert, "Fractional quantum conductance in carbon nanotubes". *Phys. Rev. Lett.* **84**, 2974 (2000)

[19] A. Hirsch, "Functionalization of single-walled carbon nanotubes". *Angew. Chem. Int. Ed*. **41**, 1853 (2004)

[20] R. Prakash, R. Superfine, S. Washbum, M.R. Falvo, "Functionalization of carbon nanotubes with proteins and quantum dots in aqueous buffer solution". *Appl. Phys. Lett.* **88**, 063102, (2006)

[21] K.V. Singh, R.R. Pandey, X. Wang, R. Lake, C.S. Ozkan, K. Wang, M. Ozkan, "Covalent functionalization of single walled carbon nanotubes with peptide nucleic acid: Nanocomponents for molecular level electronics". *Carbon* **44**, 1730 (2006)

[22] T.J. Webster, M.C. Waid, J.L. McKenzie, R.L. Price, J.U. Ejiofor, "Nano-biotechnology: carbon nanofibers as improved neural and orthopaedic implants". *Nanotechnology* **15**, 48 (2004)

[23] S. Mwenifumbo, M.S. Shaffer, M.M. Stevens, "Exploring cellular behaviour with multi-walled carbon nanotube constructs". *J. Mater. Chem.* **17**, 1894 (2007)

[24] S. Weiner, H.D. Wagner, "The materials bone: Structure-Mechanical Function Relations". *Annu. Rev. Mater. Sci.* **28**, 271 (1998)

[25] N.A. Carrell, A. L.B. Fitzgerald, B. Steiner, H.P. Erickson, D.R. Phillips, "Structure of human platelet membrane glycoproteins IIb and IIIa as determined by electron microscopy". *J. Biol. Chem.* **260**, 1743 (1985)

[26] B. Harrison, A. Atala, "Carbon nanotube application for tissue engineering". *Biomat.* **28**, 344 (2007)

[27] J.N. Coleman, M. Cadek, R. Blake, V. Nicolosi, K.P. Ryan, C. Belton, A. Fonseca, J.B. Nagy, Y.K. Gunk'ko, W.J. Blau, "High-performance nanotube-reinforced plastics: understanding the mechanism of strength increase". *Adv. Funct. Mater.* 1**4** (2004)

[28] T. Liu, I.Y. Phang, L. Shen, S.Y. Chow, W-D. Zhang, "Morphology and mechanical properties of multiwalled carbon nanotubes reinforced nylon-6 composites". *Macromolecules* **37**, 7214 (2004)

[29] J.N. Coleman, U.M. Khan, Y.K. Gun'ko, "Mechanical reinforcement of polymers using carbon nanotubes". *Adv. Mater.* **18**, 689 (2006)

[30] S-F. Wang, L. Shen, W-D. Zhang, Y-J. Tong, "Preparation and mechanical properties of chitosan/carbon nanotubes composites". *Biomacromolecules* **6**, 3067 (2005)

[31] L. Gao, L. Jiang, J. Sun, "Carbon nanotube-ceramic composites". *J. Electroceram.* **17**, 51 (2006)

[32] K. Balani, R. Anderson, T. Laha, M. Andara, J. Tercero, E. Crumpler, A. Agarwal, "Plasma-sprayed carbon nanotube reinforced hydroxyapatite coatings and their interaction with human osteoblasts in vitro". *Biomaterials* **28**, 618 (2007)

[33] R.A. MacDonald, B.F. Laurenzi, G. Viswanathan, P.M. Ajayan, J.P. Stegemann, "Collagen-carbon nanotube composite materials as scaffolds in tissue engineering". *J. Biomed. Mater. Res.* **74**A, 489 (2005)

[34] L.P. Zanello, B. Zhao, H. Hu, R.C. Haddon, "Bone cell proliferation on carbon nanotubes". *Nano Lett.* **6**, 562 (2006)

[35] M.P. Mattson, R.C. Haddon, A.M. Rao, "Molecular functionalization of carbon nanotubes and use as substrate for neuronal growth". *J. Mol. Neurosci.* **14**, 175 (2000)

[36] H. Hu, Y. Ni, V. Montana, R.C. Haddon, V. Parpura, "Chemicaly functionalized carbon nanotubes as substrate for neuronal growth". *Nano Lett.* **4**, 507 (2004)

[37] P.R. Supronowicz, P.M. Ajayan, K.R. Ullmann, B.P. Arulanandam, D.W. Metzger, R. Bizios, "Novel current-conducting composite substrates for exposing osteoblasts to alternating current stimulation". *J. Biomed. Mater. Res.* **5**, 499 (2002)

[38] M.K. Gheith, T.C. Pappas, A. Liopo, V.A. Sinani, B.S. Shim, M. Motamedi, J.P. Wicksted, N.A. Kotov, "Stimulation of neural cells by lateral current in conductive Layer-by-Layer films of single-walled carbon nanotubes". *Adv. Mater.* **18**, 2975 (2006)

[39] M.A. Correa-Duarte, N. Wagner, J. Rojas-Chapana, Ch. Morsczeck, M. Thie, M. Giersig, "Fabrication and biocompatibility of carbon nanotube-based 3D networks as scaffolds for cell seeding and growth". *Nano Lett*. **4**, 2233 (2004)

[40] S. Giannona, I. Firkowska, J. Rojas-Chapana, M. Giersig, "Verticaly aligned carbon nanotubes as cytocompatible material for enhanced adhesion and proliferation of oestoblast-like cells". *J. Nanosci. Nanotechnol*. **7**, 1679 (2007)

[41] B. Zhao, H. Hu, S.K. Mandal, R.C. Haddon, "Abone mimic based on the self-assembly of hydroxyapatite on chemically funcyionalized single-walled carbon nanotubes". *Chem. Mater*. **17**, 3235 (2005)

[42] T. Akasaka, F. Watari, Y. Sato, K. Tohji, "Apatite formation on carbon nanotubes". *Mater. Sci. Eng. C*. **26**, 675 (2006)

Chapter 3
Theory

3.1 Nanoindentation

Nanoindentation is a relatively new technique for the characterization of the mechanical properties of nanoscale materials. It has been used to study a wide range of materials, including carbon-based materials, coatings, thin films, and polymers [1-3]. Depth-sensing indentation (DSI) devices allow for the measurement of the indenter tip penetration as a function of an applied controlled load. Additionally, they are able to produce contact areas and indentation depths characterized by sub-micrometer or even nanometer dimensions for hard materials. Obtained load vs. displacement curves, together with the indenter geometry allow for the calculation of the elastic modulus and the hardness of the tested material.

The analysis of indentation load-penetration curves produced by DSI system is based on the work by Oliver and Pharr [4]. Their analysis was, in turn, based upon the relation developed by Sneddon [5] for the penetration of a flat elastic half-space by different probes with particular axisymmetric shapes.
The relationship between penetration depth h, and load P is represented in the form:

$$P = D(h - h_f)^m \ , \qquad \textbf{(Eq. 3.4)}$$

where D contains geometric constants, the sample's elastic modulus and Poisson's ratio, as well as the indenter's elastic modulus, and Poisson's ratio. h_f is the final unloading depth and m is a power law exponent that is related to the geometry of the indenter; for a flat-ended cylindrical punch $m = 1$, for a paraboloid of revolution $m = 1.5$, and for a cone $m = 2$.

The elastic modulus and hardness can be evaluated from the unloading slope of the depth-displacement curve (Fig. 3.6) and are defined as:

$$E_r = \frac{1}{2}\sqrt{\frac{\pi}{A_c}}S \quad , \qquad \textbf{(Eq. 3.5)}$$

$$H = \frac{P_{max}}{A_c} \quad , \qquad \textbf{(Eq. 3.6)}$$

where E_r is the reduced modulus, A_c is the contact area between indenter and sample, H is the local hardness, S is the constant stiffness, defined as a slope of the unloading curve fitted to the power law of Eq. 3.4. The reduced modulus combines the properties of the indenter and the sample, and is given by:

$$\frac{1}{E_r} = \frac{(1-\nu_s^2)}{E_s} + \frac{(1-\nu_i^2)}{E_i} \quad , \qquad \textbf{(Eq. 3.7)}$$

where E_s and v_s are the sample's elastic modulus and Poisson's ratio, and E_i and v_i are the elastic modulus and Poisson's ration of the indenter material. For the indentation of a plane surface of a semi-infinite elastic solid by a rigid tip, the second term in Eq. 3.7 can be neglected.

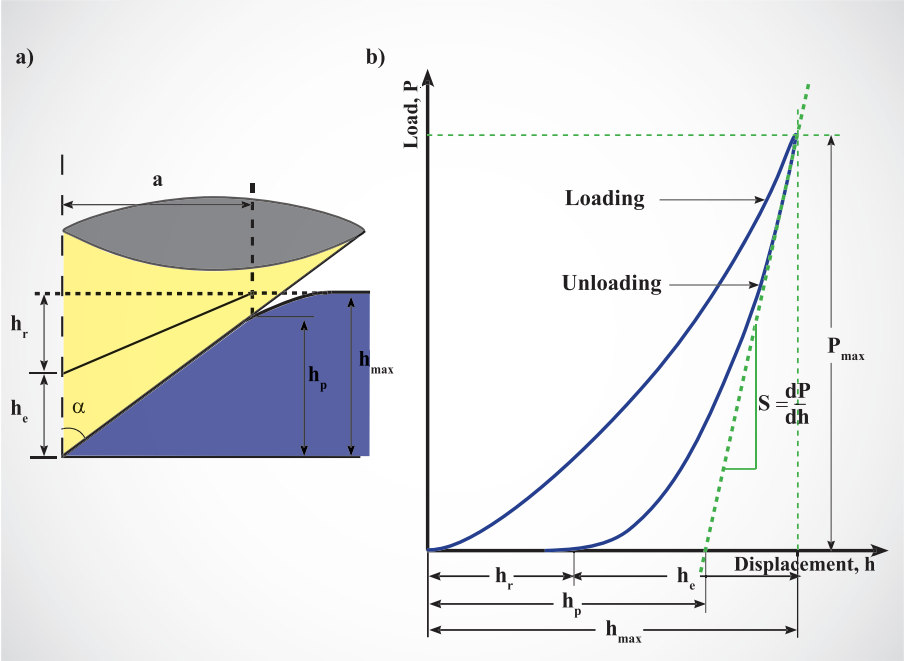

Figure 3.6: *Schematic of indenter and specimen surface at full load and unload for a conical indenter (a). Load-displacement curve with several important parameters used in the Oliver and Pharr analysis (b). h_r is the depth of the residual impression, h_{max} is the depth from the original speciment surface at load P_{max}, and h_e is the elastic displacement during unloading.*

The nanoindentation procedures include the calibration of the tip with the aim to determine the geometry of the indenter tip. Typically, a series of indentation measurements are made on a reference sample, which is homogeneous and isotropic and for which both E and v are known. The dependence of the contact area as a function of contact depth is plotted and the area function is found by using a multiterm polynomial form:

$$A_c(h_p) = C_o h_p^2 + C_1 h_p + C_2 h_p^{\frac{1}{2}} + C_3 h_p^{\frac{1}{4}} + C_4 h_p^{\frac{1}{8}} + .., \qquad \textbf{(Eq. 3.8)}$$

where C (n = 0, 1, 2...) are constant coefficients determined by the curve fit and h_p is the contact depth, determined from:

$$h_p = h_{max} - h_a = h_{max} - \varepsilon \frac{P_{max}}{S} \quad , \qquad \textbf{(Eq. 3.9)}$$

with h_{max} the maximum displacement at maximum load, h_a the elastic displacement of the surface at the contact perimeter, and ε a function of the tip geometry (i.e. for a flat-ended cylindrical punch ε = 1, for a paraboloid of revolution ε = 0.75, and for a cone ε = 2 (π-2)/π).

Nanoindentation tests and the resultant calculated physical quantities are very sensitive to many phenomena occurring during the measurements. The most commonly encountered sources of errors may arise from instrument compliance, thermal drift, indenter geometry, and a sample's surface roughness [6]. Therefore, the calculated values of H and E_r can be faulty and may not reflect the real and actual values. However, if all experiments are carried out under the same experimental conditions, the results for the diverse samples can be related and compared.

3.2 Atomic force microscopy for cell biology

The atomic force microscope (AFM), invented by Binnig in 1986 [7], has found a wide range of applications with regard to the study of biological specimens. One of the greatest benefits of the AFM is its capability of imaging biological samples at high resolution in their natural aqueous environment. This has been demonstrated through the study of a wide range of different samples, from the imaging of molecules like deoxyribonucleic acid (DNA) [8], ribonucleic acid (RNA) [9,10], and proteins [11] to the imaging of tissues [12,13]. AFM has also been applied to direct imaging of intracellular structures such as actin fibers and the nucleus, and of dynamic processes in living cells [14,15].

In addition to imaging, AFM has increasingly been used for the measurement of local mechanical properties of cells at the nanometer scale, where the elastic modulus could be determined from force-displacement curves [16,17].

3.2.1 Operation modes

3.2.1.1 Contact mode

The most common AFM mode applied in cell biology is the contact mode. In this mode, the scanning tip is in contact with the imaged sample surface. Data acquisition in contact mode is done in the following ways: In the so-called constant force mode, when the tip raster scans the samples, a feedback loop keeps the cantilever deflection constant. The tip approximately maps out the topography of the sample and keeps the force on the sample constant. In the second mode, the so-called constant-height mode, the cantilever is held at the same height during the scan with the feedback off. The main advantage of this imaging mode is its high sensitivity in the z axis; however, the force applied to the sample increases with increasing cantilever deflection and may cause damage to the tip and/or sample. Figure 3.7 schematically illustrates the working of an atomic force microscope.

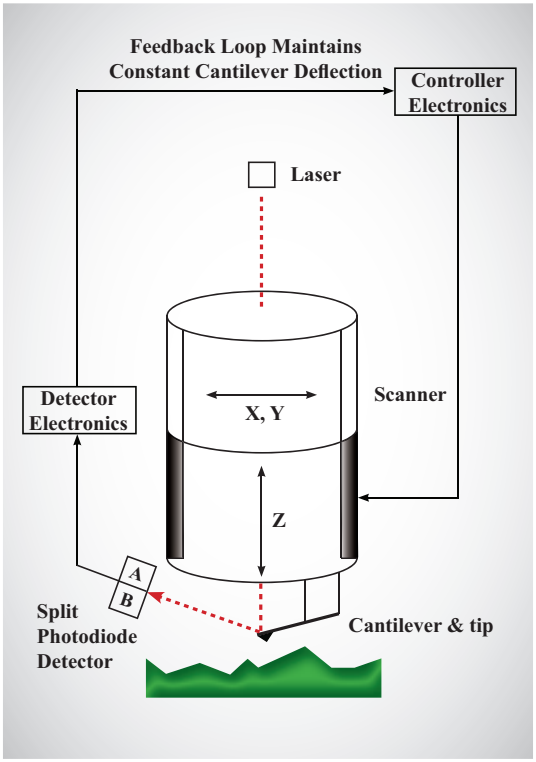

Figure 3.7: *Scheme of AFM.*

Lateral resolution in the contact mode is strictly related to tip geometry, sample roughness, and to the force applied during scanning. As observed for living cells, forces over 1 nN may result in sample deformation and increase the tip-sample contact [18,19]. The latter leads to limitations in the lateral resolution. Thus, to achieve high resolution and reduce sample perturbation, small forces are required when scanning the topography of biological samples.

3.2.1.2 Force mode

As mentioned before, AFM can also be used for the quantitative assessment of the mechanical properties of a surface. To achieve this, AFM requires the use of force-displacement curves. These curves are obtained by monitoring the cantilever deflection while ramping the piezo scanner in z direction and plotting the resulting deflection versus the piezo displacement. A complete force-curve contains both the approaching and the retracting portion. A typical force-curve recorded with a soft cantilever on a glass substrate in air is shown in Fig. 3.8.

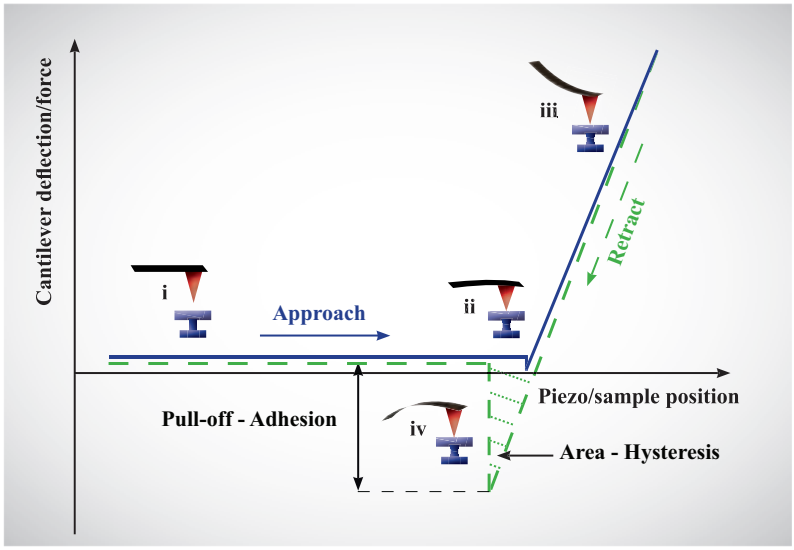

Figure 3.8: *Components of the force-curve with the approaching (solid) and retracting (dashed) portions recorded on a hard substrate.*

There are four regions of interest: At the initial part of the curve, the tip is far away from the sample and there is no interaction and no cantilever deflection (zero deflection line) (i). As the tip gets closer to the surface, the tip-sample interaction increases and shortly before tip and sample get into contact, attractive van-der-Waals forces lead to a "jump to contact" of the tip (ii). Once the tip is in contact with the surface, the cantilever deflection increases (iii). If the sample is much stiffer than the tip, the deflection increases linearly with the piezo movement. If the surface is soft compared to the cantilever's spring constant (e.g. a living cell), surface deformation or indentation will occur. Maximum cantilever deflection is obtained at the maximum extension of the piezo. After that, the piezo starts a retraction movement. The retraction curve can display a hysteresis (iv) owing to a variety of tip-sample interactions, the most common of which is adhesive force. In the case of samples probed in air, the adhesive force is due to the presence of a thin (several nanometers) layer of water adsorbed to the surface. This water layer wicks up the tip and forms a "bridge" between the tip and the sample. Pulling the tip out of that bridge requires a strong force in order to overcome the surface tension [20]. The tip may then undergo long-range interactions before the tip-sample separation distance is large enough for the cantilever to return to zero deflection.

3.2.1.3 Force-volume imaging

A force-volume imaging combines force measurements with topographic imaging. Each force curve is recorded as described above, except that the sample is also translated in the x-y plane (Fig. 3.9). The force-volume height image (FVH) is an array of z-piezo positions at the points of the maximal deflection of the force curves. Typically, the force-curves are collected using relative deflection trigger, so the FVH is a surface of equal force. For an adequate dense collection of force curves, the lateral resolution of force-volume imaging is related to the distance dependence of the interaction. Therefore, the lateral resolution varies within the volume and can not be easily defined.

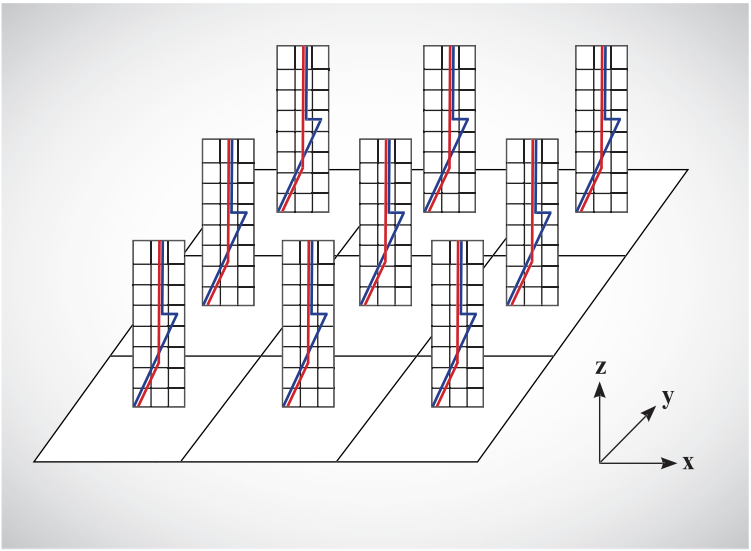

Figure 3.9: *Force-volume array of force-curves.*

Together, the FV and the FVH provide the three dimensional, laterally resolved description of the force over and within a sample. Force-volume imaging is a powerful technique, which can be used to investigate adhesive, electrical, elastic, and chemical properties of samples. Radmacher *et al.* [17] were the first who constructed one of the first AFM-based maps of cellular mechanical properties. Using force-volume imaging, they produced micro-elasticity maps of the biological cells that show local variations in their stiffness. A similar approach was used to study the contribution of the actin cytoskeleton to the local mechanical properties of cardiac myocytes [21].

3.2.2 Data analysis of force-curves

Typically, force-curves are analyzed within a given range of loading forces. Therefore, deflection values first have to be converted into loading force values. Since the cantilever springs are linear with regard to small deflections, Hooke's law can be applied:

$$F = kd \quad , \qquad \textbf{(Eq. 3.10)}$$

where k is the force constant of the cantilever, d is its deflection, and F is the corresponding force exerted by the cantilever. In experiments, the deflection is not necessarily zero when the cantilever is free, e.g., due to the stress in the cantilever, which will deform it even without an external load. Thus, the offset d_0 has to be subtracted from all deflection values. Therefore, Eq. 3.10 is changed to:

$$F = k(d - d_0) \qquad \textbf{(Eq. 3.11)}$$

The indentation is given by the difference between the sample height z and the deflection of the cantilever:

$$\delta = z - d \qquad \textbf{(Eq. 3.12)}$$

Here again, the offset must be considered, so Eq. 3.12 can be rewritten as:

$$\delta = (z - z_0)(d - d_0) \quad , \qquad \textbf{(Eq. 3.13)}$$

where d_0 is the zero deflection as above and z_0 is the z position at the point of contact.

As can be seen in Fig. 3.8, the contact point can easily be identified in the force-curve recorded on a stiff sample by direct visual inspection, with an accuracy of a few nanometers, depending on the noise and short tip-sample interaction. Nevertheless, the identification of z in a soft sample is more difficult, due to the slow increase of the deflection in respect to the piezo translator.

3.2.2.1 Analytical expression for contact elastic models: Hertz and Sneddon

The conical model for the tip has been widely used for elastic measurements on cells [17,21]. The elastic deformation of two spherical surfaces touching each other under a load was calculated theoretically in 1882 by Hertz [22]. Later, Sneddon [5] extended this calculation to other geometries, like a cone pushing onto a flat sample. These contact elastic models assume that the intended body is perfectly elastic, isotropic, smooth, and infinitely thick. Under these conditions, the analytical expression for the F-δ relationship and the radius r for the contact area between the

punch (tip) and the elastic body corresponding to typical geometries are [5]:
(i) Parabolic:

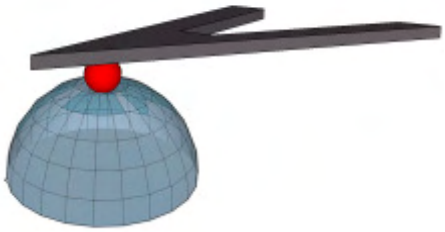

$$r = \sqrt{R\delta}$$

$$F = \frac{4}{3}\frac{E}{(1-\nu^2)}\delta^{\frac{3}{2}}\sqrt{R}\ , \qquad \textbf{(Eq. 3.14)}$$

where R is the radius of curvature at the apex of the tip and E and v are the Young's modulus and the Poisson ratio of the sample, respectively. Eq. 3.14 matches the results reported by Hertz for a spherical geometry for both the indenter and the sample [22]. The parabolic model (or Hertz model) is the most widely reported in AFM literature for sample indentation being of the same order as the radius of the tip apex.

(ii) Cone:

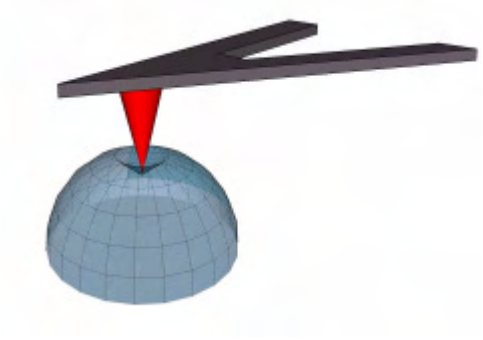

$$r = \frac{2}{\pi\tan\alpha}\delta^2$$

$$F = \frac{2}{\pi}\frac{E}{(1-\nu^2)}\delta^2\tan\alpha\ , \qquad \textbf{(Eq. 3.15)}$$

where α is the half-opening angle of the punch. This model is more useful for sample indentations much larger than the radius of the tip apex (~ 20 nm).

3.2.2.2 Fitting the elastic models in cell measurements

The mathematical function, which is finally used to fit the force-curve data, is obtained combining Eq. 3.13 and Eq. 3.15. For the conical Hertz model this results in:

$$z - z_0 = d - d_0 + \sqrt{\frac{k(d-d_0)(1-\nu^2)}{\frac{2}{\pi}E\tan\alpha}} \qquad \textbf{(Eq. 3.16)}$$

Most of the quantities in Eq. 3.16 are either known or can be measured experimentally. The force constant and the half-opening angle α can be determined before or after the experiment or can be obtained from the manufacturer's data sheet. The Poisson's ratio, which characterizes how much the elastic body extends orthogonally to the direction in which the force is applied [23], is assumed to be constant and, in the case of cells, can be chosen to be 0.5 [24]. The Young's modulus characterizing the stiffness of an elastic body subjected to low strains and the point of contact are two unknown variables. These two quantities can be determined independently using a common method established by Rotsch [25].

3.3 Mechanical properties of a cell

Like engineering materials, cells deform when an external force acts on them. Such a behavior is described by the mechanical properties of cells, and is determined by the cell composition and structure as well as the surrounding with which the cells interact. The contribution of these different factors may vary, yet, there are specific structures in a cell that dominate its deformability.

3.3.1 Structural cell components responsible for the mechanical properties of a cell

The elastic properties of cells are determined in a complex way by the composite shell envelope composed of the lipid-protein bilayer with the associated actin cortex and the internal cytoskeleton, and also by their associated proteins. A brief description of the most relevant cell structures in terms of their contribution to the overall mechanical behavior of the cell is given below.

3.3.1.1 Cell membrane

The cell membrane is a lipid bilayer, which envelopes a cell and creates a selectively permeable barrier. The thickness of this membrane is about 7.5 to 10 nm [26]. Regarding its mechanical properties, it has been reported that the lipid bilayers are several orders of magnitude softer than an AFM cantilever [27]. This result is confirmed by theoretical estimations of the response of cellular membranes to the indentation by AFM cantilevers [28]. Therefore, in terms of AFM measurements, the elastic response of the membrane is not detectable. This is only valid in the case of eucaryotic cells with soft cell membranes.

3.3.1.2 Cytoskeleton (CSK)

The cytoskeleton is an intracellular 3D network consisting of F-actin filaments (6 - 10 nm in diameter), intermediate filaments (7 - 11 nm), microtubules (25 nm), and a huge variety of associated proteins. These associated proteins control the length of the filaments, their growth, cross-linking, or bundling between filaments and anchor them to the cell membrane or other intracellular components. A fluorescence image of different cytoskeleton filaments, labeled with different dyes, can be seen in Fig. 3.10. This network is a dynamic structure that maintains different functions. It has been reported that among these functions, it is the various cytoskeletal

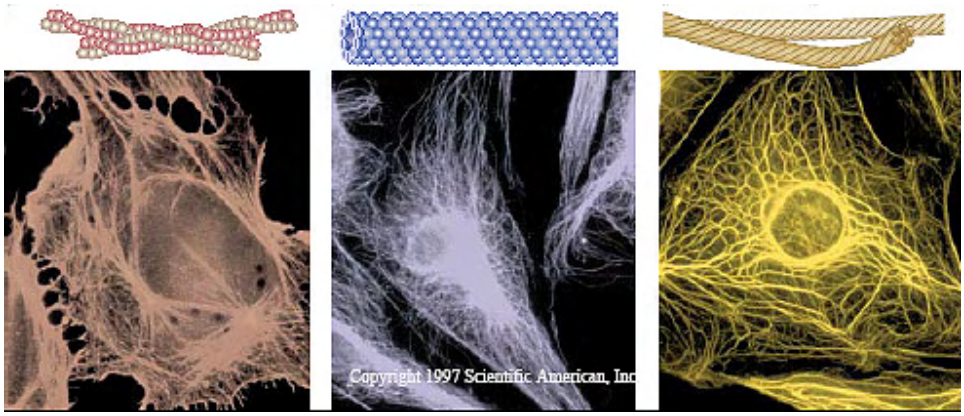

Figure 3.10: *Cytoskeleton of adherent cell consists of F-actin filaments (left), microtubules (center) and intermediate filament. The three components interconnect to create the cytoskeletal lattic which stretches from the cell surface to the nucleus. The molecular structure of each component is shown above the corresponding photograph. [29]*

components, such as actin filaments and microtubules, which contribute to the mechanical stiffness of the cells [30-33]. However, a number of studies have suggested that the different components of the CSK may have distinct mechanical roles within the cell. On the basis of the cellular tensegrity model, which assumes that the cell stiffness results from the collective interaction among all three filament systems, the actin fibers and intermediate filaments provide tension, while the microtubules are load-bearing elements that resist compression [30]. A number of studies on individual cytoskeletal elements, which implemented rheological measurements have suggested that F-actin and intermediate filaments are the components which contribute mostly to cell stiffness, while microtubules play a supportive role for other cytoskeletal elements [32].

3.3.1.3 Cell nucleus

It has been reported that the mechanical properties of the nucleus are likely to play a significant role in the mechanical response of the cell, particularly the central region of attached cells [31]. The nucleus, as well as the actin cytoskeleton, shows almost pure elastic behavior to applied mechanical forces that deform its shape [31]. According to several studies, the nucleus is softer than the rest of the cell body [17,21].

3.3.2 Cell-matrix interaction - influence on the cell deformability

The ECM (*in vivo*) or substrate (*in vitro*) to which a cell adheres plays an important role in modulating cell deformability since it may provide the mechanical support to balance the tension in adherent cells [34].

Cell adhesion to the extracellular matrix (ECM)/substrate is mainly mediated by the integrins, which are transmembrane heterodimeric proteins composed of α and β subunits, which combine to form at least 24 receptors [35]. Depending on the combination, pairing of the integrin subunits has been shown to be specific for binding to various ECM proteins (ligands) [36]. For instance, $\alpha_5\beta_1$ binds to fibronectin, whereas $\alpha_v\beta_6$ binds to collagen [37,38]. The integrins span through the lipid membrane (Fig. 3.11) and bind to ECM proteins via specific peptide domains, for example arginyl-glycyl-aspartic acid (RGD) [40], a sequence that is present in fibronectin and vitronectin [40-42]. The activated integrin receptors cluster to form focal adhesion contacts (FAs) that organize intracellular stress fibers at the plasma membrane and initiate signal transduction, both alone and with other cell surface receptors [42]. Such formed integrin-mediated cell adhesions are particularly important in cell mechanics because they generate passively cell internal prestress, i.e. pre-existing mechanical tension in the CSK even before any external stress is applied [43]. Therefore, it is expected that cell adhering to the substrate and forming many focal adhesions will imply an increase of its initial prestress. Since the stiffness and prestress are closely associated in adherent cells [44], it follows that the cell's stiffness increases in nearly direct proportion to the magnitude of the prestress [45].

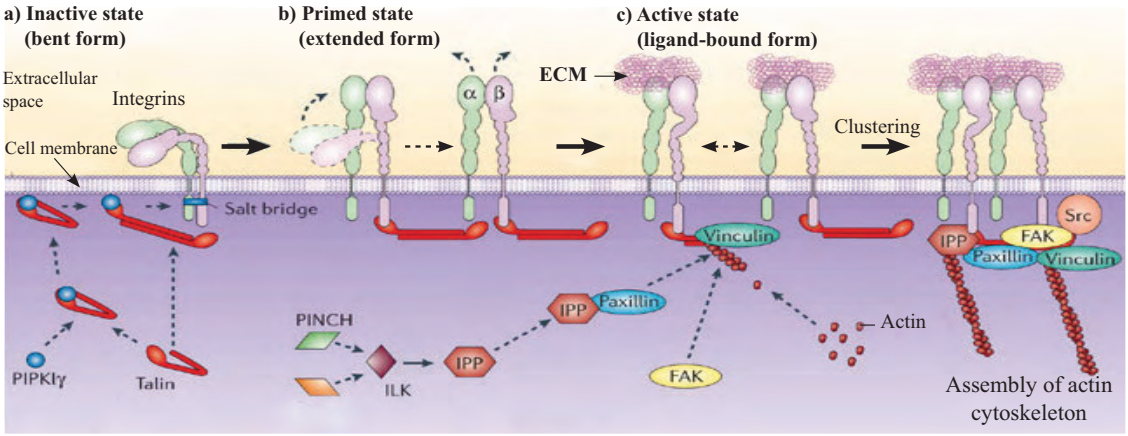

Figure 3.11: *Cell-matrix interaction: Formation of focal adhesions. a) Integrins which are not bound to the ECM are in inactive conformation (characterized by bent extracellular domains). b) Intracellular signallig events prime the integrins, which results in a comformational change that exposes the ligand-bindig site. c) The integrin extracellular domains bind specific ECM proteins. The maturation of focal adhesions involves clustering of active, ligand-bound integrins and the assembly of actin cytoskeleton. [39]*

As the type and quantity of adsorbed ECM proteins is influenced by the surfaces to which cells adhere [46], the formation of focal adhesions, their distribution, and consequently cytoskeleton organization, will vary on distinct substrates [36,47,48]. For that reason, alterations in the cytoskeletal architecture of cells upon adhesion to different ECMs/substrates are expected to lead to changes in the mechanical properties of the cells. This hypothesis has been widely supported by data from adhesion of osteoblasts on various implant materials. For example, Domke *et al*. [49] showed differences in osteoblast cell stiffness by adhering to titanium, titanium-vanadium, and cobalt-chromium materials. The reported elastic modulus values differed up to a factor of four.

References

[1] M. Olek, K. Kempa, S. Jurga, M. Giersig, "Nanomechanical properites of silica-coated multiwall carbon nanotubes-poly(methyl methacrylate) composite". *Langmuir* **21**, 3146 (2005)

[2] Y. Chen, Y.Q. Zhang, T.H. Zhang, C.H. Gan, C.Y. Zheng, G. Yu, "Carbon nanotube reinforced hydroxyapatite composite coatings produced throught laser surface alloying". *Carbon* **44**, 37 (2006)

[3] C. Klapperich, K. Komvopoulos, "Nanomechanical properties of polymers determined from nanoindentation experiments". *Journal of Tribology* **123**, 624 (2001)

[4] W.C. Oliver, G.M. Pharr, "An Improved Technique for Determining Hardness and Elastic Modulus Using Load and Displacement Sensing Indentation Experiment". *J. Mater. Res*. **7**, 1564 (1992)

[5] I.N. Sneddon, "The relaxation between load and penetration in the axisymmetric Boussinesq problem for a punch of arbitrary profile". *Int. J. Eng. Sci*. **3**, 47 (1965)

[6] A. Fischer-Cripps, "Nanoindentation 2nd ed." Springer, New York. (2004)

[7] G. Binning, C.F. Quate, C. Gerber, "Atomic force microscope". *Phys. Rev. Lett.* **56**, 930 (1986)

[8] C. Bustamante, J. Vesenka, C.L. Tang, W. Rees, M. Guthold, R. Keller, "Circular DNA molecules imaged in air by scanning force microscope". *Biochemistry* **31**, 22 (1992)

[9] Y.L. Lyubchenko, A.A. Gall, L.S. Sklyakhtenko, R.E. Harrington, B.L. Jacobs, O.I. Oden, S.M. Lindsay, "Atomic force microscopy of double standed DNA and RNA". *J. Biomol. Struct. Dynam*. **10**, 589 (1992)

[10] Y.L. Lyubchenko, B.L. Jacobs, S.M. Lindsay, "Atomic force microscopy of reovirus dsRNA: A routine technique for length measurements". *Nucleic Acids Res.* **20**, 3983 (1992)

[11] S. Karrasch, R. Hegerl, J.H. Hoh, W. Baumeister, A. Engel, "Atomic force microscopy produces faithful high-resolution images of protein surfaces in an aqueous environment". *Proc. Natl. Acad. Sci.* **91**, 836 (1994)

[12] N.J. Fullwood, A. Hammiche, H.M. Pollock, D.J. Hourston, M. Song, "Atomic force microscopy of the cornea and sclera". *Curr. Eye Res*. **14**, 529 (1995)

[13] T. Ushiki, M. Shigeno, K. Abe, "Atomic force microscopy of embedment-free sections of cells and tissues". *Arch. Histol. Cytol*. **57**, 427 (1994)

[14] E. Henderson, P.G. Haydon, D.S. Sakaguchi, "Actin filament dynamics in living gial cells imaging by atomic force microscopy". *Science* **257**, 1944 (1992)

[15] L. Chang, T. Kious, M. Yorgancioglu, D. Keller, J. Pfeiffer, "Cytoskeleton of living, unstained cells imaged by scanning force microscopy". *Biophys. J.* **65**, 1282 (1993)

[16] M. Radmacher, J.P. Cleveland, M. Fritz, H.G. Hansma, P.K. Hansma, "Mapping interaction forces with the atomic force microscope". *Biophys. J.* **66**, 2159 (1994)

[17] M. Radmacher, M. Fritz, C.M. Kacher, J.P. Cleveland, P.K. Hansam, "Measuring the viscoelasticelastic properties of human platelets with the atomic force microscope". *Biophys. J.* **70**, 556 (1996)

[18] M. Radmacher, "Measuring the Elastic Properties of Biological Samples with the AFM". *IEEE* **16**, 47 (1997)

[19] F. Braet, C. Rotsch, E. Wisse, M. Radmacher, "Comparison of fixed and living liver endothelial cells by atomic force microscopy". *Appl. Phys. A* **66**, 575 (1998)

[20] A.L. Weisenhorn, P.K. Hansma, T.R. Albrecht, C.F. Quate, "Forces in atomice force microscopy in air and water". *Appl. Phys. Lett*. 54, 2651 (1989)

[21] U.G. Hofmann, Ch. Rotsch, W.J. Parak, M. Radmacher, "Investigating the Cytoskeleton of Chicken Cardiocytes with the Atomic Force Microscope". *J. Str. Biol*. **119**, 84 (1997).

[22] K.L. Johnson "Contact Mechanics". Cambridge University Press (1985)

[23] A. Vinckier, G. Semenza, "Measuring elasticity of bilogical materials by atomic force microscopy". *Febs. Letters* **430**, 12 (1998)

[24] L.R. Treloar, The Physicis of Rubber Elasticity. Clarendon Press, Oxford (1975)

[25] C. Rotsch, K. Jacobson, M. Radmacher, "Dimensional and mechanical dynamics of active and stable edges in motile fibroblasts investigated by using atomic force microscopy. *Proc. Natl. Acad. Sci*. **96**, 921 (1999)

[26] R.A. Freitas, Nanomedicine, Volume I: Basic capabilities. *Landes Bioscience* (1999)

[27] M. Radmacher, "Measuring the elastic properties of living cells by atomic force microscope". *Methods in Cell Biology*, **68** (2002)

[28] A.A. Boulbitch, "Deflection of a cell membrane under application of local forces". *Phys. Rev. Lett.* **57**, 2123 (1998)

[29] D.E. Ingber, "The architecture of life" *Scientific American* **278**, 48 (1998).

[30] D.E. Ingber, "Tensegrity I. Cell structure and hierarchical systems biology". *J. Cell Sci*. **116**, 1157 (2003)

[31] S.R. Heidemann, S. Kaech, R.E. Buxbaum, A. Matus, "Direct Observation of the Mechanical Behaviors of the Cytoskeleton in Living Fibroblasts". *J. Cell. Biol*. **145**, 109 (2007)

[32] P.A. Janmey. U. Euteneuer P. Traub, M. Schliwa, "Viscoelastic Properties of Vimentin Compared with other Filamentous Biopolymer Networks". *J. Cell. Biol*. **113**, 155 (1991)

[33] H. Haga, S. Sasaki, K. Kawabata, E. Ito, T. Ushiki, T. Sambongi, "Elasticity mapping of living fibroblasts by AFM and immunofluoroscence observation of the cytoskeleton". *Ultramicroscopy* **82**, 253 (2000)

[34] C. Zhu., G. Bao, N. Wang, "Cell mechanics: mechanical response, cell adhesion and molecular deformation". A*nn. Rev. Biomed. Eng*. **2**, 189 (2000)

[35] M.C. Siebers, P.J. Brugge, X.F. Walboomers, J.A. Jansen, "Integrins as linker proteins between osteoblasts and bone replacing materials. A critical review". *Biomaterials* **26**, 137 (2005)

[36] S.F. El-Amin, H.H. Lu, Y. Khan, J. Burems, J. Mitchell, R.S. Taun, C.T. Laurencin, "Extracellular matrix production by human osteoblasts cultured on biodegradable polymers applicable for tissue engineering". *Biomaterials* **24**, 1213 (2003)

[37] A.J. Garcia, D. Boettiger, "Integrin-fibronectin interaction at the cell-material interface: initial integrin binding and signaling". *Biomaterials* **20**, 2427 (1999)

[38] T. Saito, S.M. Albelda, C.T. Brighton, "Identification of integrin receptors on cultured human bone cells". *J. Orthop. Res*. **12**, 384 (1994)

[39] K.R. Legate, E. Montanez, O. Kudlacek, R. Fassler, "ILK, PINCH and parvin: the tIPP of integrin signaling". *Nature* **7**, 20 (2006)

[40] E. Stanley, D. Souza, M.H. Ginsberg, E.F. Plow, "Arginyl-glycyl-aspartic acid (RGD): a cell adhesion motif". *TIBS* **16**, 246 (1991)

[41] A.K. Shah, J. Lazatin, R.K. Sinah, T. Lennox, N.J. Hickok, R.S. Tuan, "Mechanism of BMP - 2 stimulated adhesion of osteoblastic cells to titanium alloy". *Biology of the Cell* **91**, 131 (1999)

[42] K. Burridge, M. Chrzanowska-Wodnicak, "Focal adhesions, contractility, and signaling".

Ann. Rev. Cell Dev. Biol. **12**, 463 (1996)

[43] D. Stamenowic, M.F. Coughlin, "The role of prestress and architecture of the cytoskeleton and deformability of cytoskeletal filaments in mechanics of adherent cells: a quantitative analysis". *T. Theor. Biol.* **201**, 63 (1999)

[44] N. Wang, I.M. Tolic-Nørrelykke, J. Chen, S.M. Mijailovich, J.P. Butler, J.J. Fredberg, D. Stamenowic, "Cell prestress. I. Stiffness and prestress are closely associated in adherent contractile cell". *Am. J. Physiol. Cell. Physiol*. **282**, C606 (2002)

[45] D. Stamenowic, J.J. Fredberg, N. Wang, J.P. Butler, D.E. Ingber, "A microstructural approch to cytoskeletal mechanics based on tensigrity". *T. Theor. Biol*. **181**, 125 (1996)

[46] K. Webb, V. Hladly, P.A. Tresco, "Relationships among cell attachment, spreading, cytoskeletal organization, and migration rate for anchor-dependent cells on model surfaces". *J. Biomed. Mater. Res*. **49**, 362 (2000)

[47] A. Krause, E.A. Cowles, G. Gronowicz, "Integrin-mediated signaling in osteoblasts on titanium implant materials". *J. Biomed. Mater. Res*. **52**, 738 (2000)

[48] G. Schneider, K. Burridge, "Formation of Focal Adhesions by Osteoblasts Adhering to Different Substrata". *Exp. Cell Res.* **214**, 264 (1994)

[49] J. Domke, S. Dannohl, W.J. Parak, O. Muller, W.A. Aicher, M. Radmacher, "Substrate dependent differences in morphology and elasticity of living osteoblast investigated by atomic force microscopy". *Colloids Surf. B. Biointerfaces*. **19**, 367 (2000)

Chapter 4
Experimental

4.1 Sample preparation

4.1.1 Functionalization of MWNTs

The MWNTs used were obtained from NanoLab Inc., synthesized by chemical vapor deposition with flowing acetylene gas as the carbon source. Alumina particles, coated with iron catalyst, were used as seeds for the CNT growth. Multiwalled carbon nanotubes had a purity of 95 %, a diameter in the range of 15 - 45 nm, and lengths between 1 - 20 μm.

Generating functional groups on the surface of carbon nanotubes is necessary to overcome their poor solubility in solvents, to improve their specificity, and to provide an avenue for further chemical modification. In this study, both covalent and non-covalent methods were used to introduce desired chemical groups to the nanotubes.

4.1.1.1 Oxidation with acids

Multiwalled carbon nanotubes were covalently functionalized by the following oxidation procedure [1]: 16 mg of MWNTs were suspended in a concentrated nitric and sulfuric acid mixture (1:3 v/v, 80 mL), (HNO_3; Sigma-Aldrich, > 70 %; H_2SO_4: Sigma-Aldrich, > 95 %) and subsequently sonicated for 2 h (ultrasonic bath 200, W) and left aside for 20 h. The resultant mixture was centrifuged (18514g, 60 min.), and the resulting black sediment was washed throughly with pure water (35 mL); this process was repeated four times. Finally, the carbon nanotubes were re-dispersed in 200 mL of water followed by a short treatment in the ultrasonic bath (200 W, 30 min.). As shown [1], this oxidation treatment disrupts the π bonding symmetry of sp^2 hybridize carbon atoms and produces a high density of functional groups along the entire length of CNTs, such as carboxyl, carbonyl, and phenolic groups.

Carboxyl groups are dominant, therefore, the CNT-COOH abbreviation is used to refer to oxidized nanotubes (Fig. 4.12).

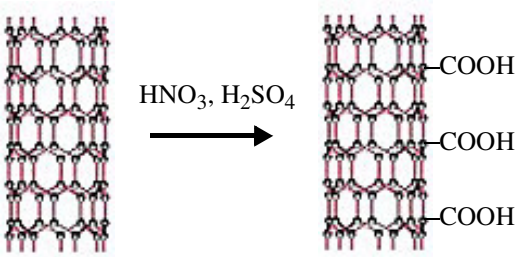

Figure 4.12: *Scheme of covalent functionalization of MWNTs with acids.*

With these groups present, carbon nanotubes show a very good dispersibility in aqueous solvents, where they remain stable for months.

4.1.1.2 Polymer wrapping

Another functionalization of carbon nanotubes was done by means of a polymer wrapping method [2]. In this procedure, the positively charged polyelectrolyte poly(allylamine hydrochloride) (PAH), could be non-covalently adsorbed around the carbon nanotubes due to van -der-Waals interactions, mechanical wrapping, and anchoring (Fig. 4.13).

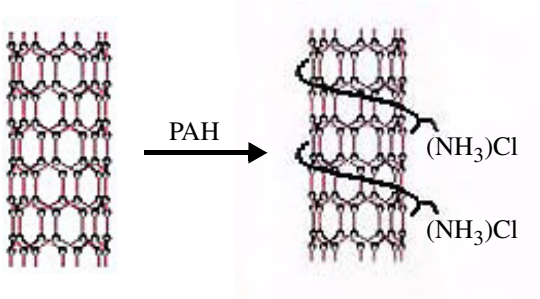

Figure 4.13: *Schematic of non-covalent functionalization of MWNTs with PAH.*

An amount of 50 mg of MWNTs was dispersed in a 0.5 wt% PAH (Sigma-Aldrich, Mw = 70 000) salt solution (0.5 M NaCl, 500 mL) and sonicated (200 W) for 4h, then stirred overnight at 80 ^{o}C and again left in an ultrasonic bath for 3 h. Excess polymer was removed by centrifugation (18514 g, 90 min.) and the sediment was washed with pure water; this process was repeated 3 times. Finally, the residual black solid was re-dispersed in water (500 mL) by short ultrasonication (200 W, 120 min), giving a stable, homogenous suspension of nanotubes.

The amine functionalities on the surface of the nanotubes ensure good separation and stability due to electrostatic interactions (repulsions) in aqueous solutions.

4.1.2 Free-standing CNT-based matrix preparation

Free-standing CNT-based matrices were fabricated using the conventional lithographic technique combined with the Layer-by-Layer assembly process [3]. A brief description of these methods is given below.

4.1.2.1 Nanosphere lithography

The preparation of CNT-based matrices started from the creation of a monolayer mask using nanosphere lithography (NSL) [4]. This technique is based on the self-assembly of latex spheres (PS) into hexagonally closed-packed (hcp) monolayers. Aqueous dispersion of latex spheres (MicroParticles) with a diameter of 1.71 μm (10 wt%) were diluted in an organic solvent (PS/methanol, 1:1 v/v) and slowly applied to the water surface using a glass pipette with a curved ending. All suspensions were spread inside a Petri dish (15 cm in diameter). To avoid crack formation in the lattice and to leave enough place for stress relaxation, the transfer of PS suspensions was stopped when the monolayer covered about 70 % of the water surface. At this point, the particles are arranged into a colloidal multicrystalline monolayer. To improve the monolayer i.e. to create monocrystals, the water with the floating mask was gently waved by slow tilting of the dish (about 30 min). After this treatment, the silicon substrates were submerged in the water and aligned under the PS mask. Next, the water from the Petri dish was pumped out slowly, until the PS monolayer approached the underlying substrates.

All masks were deposited on silicon substrates (1 x 3 cm^2), previously cleaned in a solution of H_2O_2/H_2SO_4 (1:4 v/v) for 10 min, rinsed in pure water, and dried in an argon stream. Additionaly, they were covered with a so-called sacrificial layer, created by deposition of polystyrene solution (150 mg of polystyrene dissolved in 2 mL of chloroform) via a spin-coating process. Coating was performed at 2850 rpm and resulted in a layer thickness of 2.5 μm. This layer was necessary in order to obtain a free-standing CNT-based film.

4.1.2.2 Layer-by-Layer assembly

The LbL matrices were created on solid substrates by alternate deposition of oppositely charged polyelectrolytes and functionalized MWNTs (see Fig. 4.14) [3,5]. All samples were prepared in an automatic process using an dipping machine (Dipping Robot DR3, Kirstein GmbH, Germany). The silicon substrates, already covered with a sacrificial layer and PS mask, were vertically arranged in a custom-made holder, and were immersed into the first polyelectrolyte solution (.5

wt% of PE salt solution (0.5 M NaCl).). Subsequently, the slides were rinsed successively in three different beakers containing pure water, for 5, 2, and 1 min., respectively. Next, they were dipped into the carbon nanotube solution followed by the same rinsing procedure. After every fifth deposition cycle, a layer of nanotubes was replaced with a layer of contrarily charged polyelectrolyte. In a typical experiment, a deposition time of 10 min was used for the polyelectrolyte and of 20 min for the carbon nanotubes.

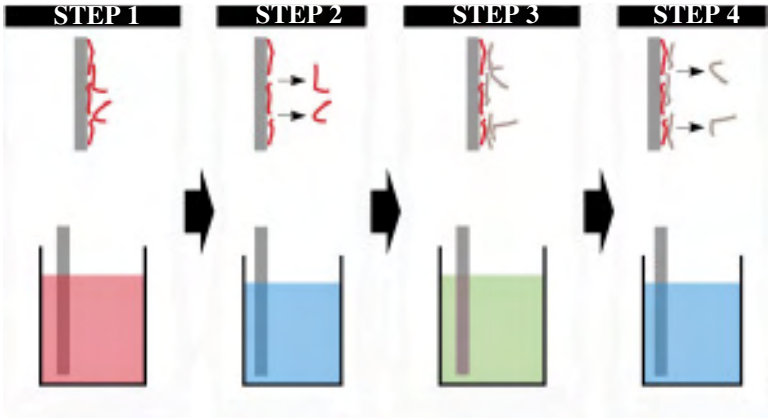

Figure 4.14: *Layer-by-Layer assembly method. Step 1 adsorption of positively charged polyelectrolyte, Step 2 washing stage, Step 3 deposition of negatively charged CNTs, Step 4 washing.*

The thus-produced LbL-films were investigated in terms of their mechanical and biocompatible properties. Therefore, different combinations of polyelectrolytes and chemically-modified carbon nanotubes were used (Table. 4.2)

Tab. 4.2: Carbon nanotubes and polyelectrolytes used to prepared different LbL structures.

MWNTs	Polyelectrolytes	LbL Structure	Outermost layer	n	Thickness [μm]
MWNT-COOH	PEI (M_w = 70 000), PSS (M_w = 70 000)	$[(PEI/MWNT\text{-}COOH)_5(PEI/PSS)]_n$	MWNT-COOH	30	~ 2
MWNT-COOH	PDDA (M_w = 350 000), PSS (M_w = 70 000)	$[(PDDA/MWNT\text{-}COOH)_5(PDDA/PSS)]_n$	MWNT-COOH	30	~ 2
MWNT-COOH	PAH (M_w = 70 000), PSS (M_w = 70 000)	$[(PAH/MWNT\text{-}COOH)_5(PAH/PSS)]_n$	MWNT-COOH	30	~ 2
MWNT-PAH	PSS (M_w = 70 000), PAH (M_w = 70 000)	$[(PSS/MWNT\text{-}PAH)_5(PSS/PAH)]_n$	MWNT-PAH	30	~ 2
–	PSS (M_w = 70 000), PAH(M_w = 70 000)	$[PSS/PAH]_n$	PAH	5	–
–	PSS (M_w = 70 000), PAH (M_w = 70 000)	$[PDDA/PSS]_n$	PSS	5	–

To obtain free-standing films, the LbL composites were peeled off from the substrates by means of chemical delamination. The samples were immersed into tetrahydrofuran (THF, Sigma-Aldrich) for 5 min and then washed in pure water. Free-standing films were picked up from the suspended state with tweezers and subsequently dried and cut to the desired size and shape.

CNT-based films were additionally modified by a reactive ion etching process (RIE). The RIE was performed in an oxygen atmosphere with the addition of argon. The flow ratio was controlled by changing the flow rate of each gas, while the total flow rate was held constant at 20 sccm. The total gas pressure was 100 mTorr and the input power was 80 W.

4.1.3 MWNT-based matrices surface modification

Calcium phosphate nanoparticles (CP NPs) were kindly provided by the Kotov Lab. (University of Michigan, USA). They were synthesized from aqueous calcium nitrate and phosphoric acid in the presence of 2-carboxyethylphosphonic acid (CEPA). The produced negatively-charged nanoparticles had a discoidal shape with a diameter of 30-80 nm and a height of less than 5 nm [6]. CP NPs were covalently attached to the functionalized carbon nanotubes. Shortly, matrices assembled from PAH-functionalized carbon nanotubes were placed in vials with a solution containing CP NPs. The samples were kept in solution at room temperature for 1 h. The matrices were then removed from the vials and rinsed with pure water.

4.1.4 Vertically-aligned CNT matrices

Both carpets of vertically-aligned carbon nanotubes (VACNTs) and periodical VACNT-arrays were produced at NanoLab (nano-lab.com). They were fabricated by using plasma-enhanced hot filament chemical vapor deposition (PECVD), described in detail elsewhere [7]. The carpet of VACNTs was produced on nickle nanoparticle-coated substrates, which were subsequently placed into a CVD chamber. In the case of the periodic arrays of VACNTs, nanosphere litography was involved. In brief, the self-assembled monolayer of latex spheres with a diameter of 540 nm was used as a mask to deposit Ni dots on a chromium-coated sapphire substrate. Nickel deposition was done by electron beam evaporation. All PS-spheres were then removed from the substrate by ultrasonication in toluene. As a result, quasi-triangular-shaped catalytic Ni dots in a honeycomb lattice pattern were created. The substrates were then placed in a PECVD system under NH_3 plasma yelding high-quality aligned arrays of nanotubes with long-range periodicity and controlled length [7].

4.1.5 Cell cultures

All experiments were carried out using HOB-C, human hipbone osteoblast cells, which were purchased from PromCell. The cells were cultivated in Dulbbeco's Modified Eagle Medium with GlutaMAX^{TM}, 4500 mg/L D-glucose and sodium pyruvate (DMEM, Gibco), supplemented with heat-inactivated (30 min at 56 ^{o}C in a wather bath) 10 % fetal bovine serum (FBS, Gibco), 1 X Insulin-Transferrin-Sodium Selenite Media Supplement (Sigma), 100 µg/mL Penicillin and 100 µg/mL Streptomycin (Penicillin-Streptomycin, Gibco). In order to offer a biologically-friendly enviroment to the cells, they were incubated at 37 ^{o}C in humidified air with 5 % CO_2. The medium was replaced every two days. After reaching subconfluence, the cells were detached from the culture flask using a 0.25 % trypsin-EDTA solution. Subsequently, the dissociated cells were centrifuged, washed, and resuspended in supplemented DMEM medium.

4.1.5.1 Seeding of osteoblast-like cells on matrices

First, the samples were sterilized with UV light (30 min) and placed into conventional 6-well culture plates. To investigate cell growth on the substrate, osteoblast-like cells were counted and seeded onto the substrates at a density of 2000 cells/cm^2 on the sample surface. The cells were allowed to grow under standard cell culture conditions (described above). After the third and seventh day of the incubation period, osteoblast-like cells were observed under a light microscope or fixed for the investigation via scanning electron microscopy.

4.1.5.2 Direct-contact toxicity study (mitochondrial activity)

A toxicity study was performed using MTT assays (Sigma), which is based on the reduction of the yellow tetrazolium salt 1-(4,5-dimethylthiazol-2-yl)-3,5-diphenylformazan (Sigma) into an insoluble formazan product by the mitochondria of living cells. Briefly, HOB-C cells at a density of 2000 cells/cm^2 were incubated in 24-well plates for 7 days on four samples of each group (CNT-based matrices and glass conntrols) in a volume of 100 µL DMEM, supplemented with 10 % FBS and 1 % Penicilin/Streptomycine, at 37 ^{o}C in a humidified 5 % CO_2. After 7 days, 10 µL of MTT (5 mg/mL) was added to each well, resulting in a final MTT concentration of 0.5 mg/mL. Afterwards the cells were incubated for another 3 hours. At the end of the assay, the blue formazan reaction product was dissolved by adding 100 µL of dimethylsulfoxide (DMSO) (Sigma) and leaving in the incubator overnight. Then, the complete solubilization of the blue formazan crystals was verified and the solution was transferred to a 96-well plate. The light absorbance of dissolved formazan was measured at 570 nm using an ELISA microplate reader (Packard Instrument Co.).

4.1.5.3 Preparation of cell samples for AFM measurements

For the measurement of Young's modulus, the cells were plated on prepared substrates (1 x 1 cm^2) at a density of approx. 2000 cell/cm^2 and were placed in an incubator for 48 hours before the experiments in order to obtain 80 % of confluence stage, where isolated cells could be identified. Just before the AFM measurements, the growth medium was replaced with CO_2-independent DMEM medium.

4.1.5.4 Cell fixation for SEM investigation

Prior to fixation, the cells were washed once with Earle's buffered saline solution (EBSS, Gibco) and fixed with 2.5 % glutardialdehyde (50 % solution in water, Merck,) buffered in 0.1 M cacodylate (Carl Roth), pH 7.4, for 2 h at 4 °C. After washing in 0.1M cacodylate buffer (3 x 10 min), the samples were dehydrated through a series of ethanol concentrations (30 %, 50 %, 70 %, 80 %, 90 %, 95 %, each 15 min), followed by further dehydration (3 x 3 min in 100 % ethanol). The final dehydration was done in hexamethyldisilazane (Carl Roth) for 1 h, followed by air-drying over night under the hood.

4.1.5.5 Cell proliferation-MTT assay

For the evaluation of cell proliferation MTT assay was used (see 4.1.5.2). HOB cells were seeded on prepared MWNT-based substrates (1 x 1 cm^2) at a density of 2500 cell/cm^2 and placed in standard culture conditions for a period of 1, 3 and 7 days. After the prescribed time period, the substrates were rinsed in phosphate-buffered saline to remove any nonadherent cells. Subsequently, the samples were incubated in MTT reagent for approximately 3 h. After this time, a detergent solution was added to solubilize the colored crystal. The samples were read using an ELISA plate reader at a wavelength of 570 nm. The number of viable cells was calculated from the amount of the created formazan product.

4.1.5.6 Immunofluorescent staining

For the visualization of the actin filaments and vinculins, osteoblast cells were seeded on the substates for 24 h, then washed with PBS, and fixed with 1.5 % paraformaldehyde in PBS for 10 min. Afterwards, the cells were permeabilized with 0.1 % Triton X-100, blocked with 1 % BSA in PBS for 20 min and incubated with a 1:50 dilution of mouse anti-human vinculin (Sigma) for 1 h at room temperature. Subsequently, the cells were labeled with Alexa 647 conjugated secondary antibody (antibody dilution 1:100). The actin filaments were labeled with TRITC-conjugated phalloidin (Sigma). The cells were visualized on an inverted microscope (Nikon Elipse 1000).

4.1.5.7 Adsorption of serum proteins onto CNT-based matrices

Bovine serum albumin (BSA) was used as a model protein in this study. 100 µL of BSA solution (1mg/ml protein/PBS solution) were pipetted onto CNT-based matrices (CNT-PAH and CNT-COOH) and polyelectrolyte films (PSS/PAH and PDDA/PSS) in a six-well plate. The experiment was conducted in a sterile humidified incubator at 37 ^{o}C over 1 h. The solution with non-adherent proteins was then removed and saved as total volume. The substrates with adsorbed proteins were washed a few times and incubated for 10 min in Coomassie G-250 dye (Sigma). The samples were investigated using UV-vis absorption spectroscopy.

To obtain quantitative information about protein adsorption, 5 µL of the removed initial solution were mixed with 200 µL of Coomassie G-250 dye in a 96-well plate and incubated at room temperature for a few minutes. Protein adsorption was analyzed using the micro Bradford protein assay (Sigma) and measured using an ELISA microplate reader (Packard Instrument Co.) at a wavelength of 595 nm. Each protein concentration was calibrated using a standard curve. The degree of adsorption was determined by subtracting the residual protein from the initially added proteins. Measurements were performed in triplicate for each sample.

4.2 Experimental techniques

The MWNT-based matrices were characterized in terms of their structural, mechanical, and biocompatible properties. A brief description of the equipment used during these studies and the conditions of each experiment is given below.

4.2.1 Structural characterization (SEM, AFM)

The topography and the morphology of the MWNT-based matrices as well as of the osteoblast cells were characterized with electron and atomic force microscopes:

Scanning electron microscope (SEM) images were obtained using a LEO Supra 55 (Zeiss), operating at an acceleration voltage of up to 20 kV.

Transmission electron microscopy (TEM) was conducted on a Leo 922A with an acceleration voltage of 200 kV. An Oxford X-ray system at the TEM was used for Energy Dispersive X-ray Analysis (EDX).

The atomic force microscope (AFM) measurements were performed in air and water using a Multimode Nanoscope IV (Veeco/Digital Instrument), operating in contact and tapping mode.

4.2.2 Nanoindentation

Nanoindentation tests were carried out using an AFM (NanoScope IV Digital Instruments) with a conjugated TriboScope nanomechanical test instrument from Hysitron Inc. In this study, diamond conical and Berkovich tips were used as indenters. The total included angle of the Berkovich tip was 142.3 ^{o}, with a half angle of 65.35 ^{o}, which makes this tip very flat and efficient for a wide range of materials, including polymers. A conical tip with a nominal radius of curvature equal to 1 μm was used for scratching experiments due to the non-directional geometry.

The hardness and elastic modulus were calculated from the recorded unloading step of the depth-displacement curves. The typical indentation experiment was carried out using a triangular force profile with an indentation force ranging from 25 to 250 μN and a loading/unloading rate of 40 μN/s. In general, indents with a contact depth ranging from 50 to 500 nm were performed. To minimize the effect of material creep, a 20 s hold time was implied at the maximum load. Prior to indentation, the tip was used for surface scanning, in order to find a resonably smooth area and to avoid roughness effects on the mechanical properties. The indentation depth was maintained at less than 15 % of the film thickness, in order to avoid and minimize substrate contributions to the measured nanomechanical properties. At least eight indents were performed for each maximum applied load over the whole area of the sample, but at a reasonable distance from the sample edges to avoid boundary influence on the mechanical properties of the tested composites. The data from the indents, gained under the same maximum load, were averaged to obtain the mean and standard deviation for all samples.

The coefficient of friction was obtained in the nanoscratch experiment and measured as a ratio of the lateral force to the normal force [8]. In all tests, the scratch length was set to 5 μm. In the ramp force test, the maximum normal force of 200 μN was applied. The load was applied for 20 s giving a scratching rate of 0.5 μN/s. Each sample was tested repeatedly, and a plot of the coefficient of friction vs. lateral displacement was used to characterize the sample's properties. In the constant load experiment, the lateral force and normal displacement were obtained by applying a constant normal force ranging from 15 to 100 μN and a scratch displacement of 5 μm. At least four scratches were conducted for different normal force values. The average values of the coefficient of friction of four scratches at the same maximum constant normal load were used to estimate the friction behavior of the samples.

Tip calibration was carried out on poly(methyl methacrylate) (PMMA) with an elastic modulus equal to 3.6 GPa [8]. The calibration procedure was repeated for three independent PMMA samples, and a high reproducibility was observed.

4.2.3 AFM elasticity measurements

The elastic measurements were carried out on a Multimode Nanoscope IV (Veeco/Digital Instrument). In this study, soft V-shaped, gold-coated silicon nitride cantilevers with a nominal

spring constant of k = 0.06 N/m (DNP-NP, Veeco) were used. The pyramidal tip of the cantilevers had a nominal radius curvature of R ~ 20 - 60 nm and an opening angle of $\alpha = 35^{o}$. Before each experiment, the cantilevers were cleaned in *piranha* solution ($H_2SO_4 + H_2O_2$, 70:30) for 30 min and subsequently rinsed with pure water.

The photodiode sensitivity calibration for each cantilever was assessed from the slope of the contact straight line of a force curve recorded in a region where the substrate was free of cells.

Young's modulus was calculated from the loading part of the force-curves. Force-curves were taken only in the central location of the cell with the aim to avoid variability arising from probing different cellular structures. Additionally, to minimize the influence of the stiff substrate, force-curves were recorded on cells with a height of more than 2 μm. The applied loading force was around 2 nN for living and 5 nN for fixed cells, respectively. This protocol was used for 10 cells from each sample. Young's modulus was calculated from at least 10 curves per cell. The obtained data were averaged to get the mean and standard deviation for all samples.

To produce micro-elasticity maps of the biological cells showing local variation in their stiffness, the force volume mode (FV) was used. All FV images were recorded in a relative trigger mode, with a trigger threshold of 20 nm, giving 1.2 nN maximum loading force.

References

[1] R. Yu, L. Chen, Q. Liu, J. Lin, K.L. Tan, S.C. Ng, H.S.O. Chan, G.Q. Xu, G-Q, T.S.A. Hor, "Platinum deposition on carbon nanotubes via chemical modification". *Chem. Mater.* **10**, 718 (1998)

[2] M. Olek, K. Kempa, S. Jurga, M. Giersig, "Nanomechanical properties of silica-coated multiwall carbon nanotubes-poly(methyl methacrylate) composit". *Langmuir* **21**, 3146 (2005)

[3] I. Firkowska, M. Olek, N. Pazos-Perez, J. Rojas-Chapana, M. Giersig, "Highly ordered MWNT-based matrixes: topography at the nanoscale conceived for tissue engineering". *Langmuir* **22**, 5427 (2006)

[4] A. Kosiorek, W. Kandulski, P. Chudzinski, K. Kempa, M. Giersig, "Shadow nanosphere litography: symulation and experiment". *Nano Lett.* **4**, 1359 (2004)

[5] G. Decher, Fuzzy nanoassemblies: toward layered polymeric multicomposites", *Science*, **227**, 1232 (1997)

[6] C. Andres, V. Sinani, D. Lee, Y. Gun'ko, N. Kotov, "Anisotropic calcium phosphate nanoparticles coated with 2-carboxyethylphosphonic acid". J. *Mater. Chem.* **16**, 3964 (2006)

[7] K. Kempa, B. Kimball, J. Rybczynski, Z.P. Huang, P.F. Wu, D. Steeves, M. Sennett, M. Giersig, D. Rao, D.L. Carnaham, D.Z. Wand, J.Y. Lao, W.Z. Li, Z.F. Ren, "Photonic crystals based on periodic arrays of alligned carbon nanotubes". *Nano Lett*. **3**, 13 (2003)

[8] K. Rau, R. Singh, E. Goldberg, "Nanoindentation and nanoscratch measurements on silicone thin films synthesized by pulsed laser ablation deposition". *Mater. Res. Innovat*. **5**, 151 (2002)

Chapter 5
Results and Discussion

5.1 Structural properties of the samples

Prior to the evaluation of the mechanical properties of the MWNT-based matrices and the cellular response to their diverse nanotopographies, the morphology and structure of the samples have been characterized using scanning electron microscopy and atomic force microscopy.

5.1.1 Free-standing MWNT-based matrices

The method used to produce free-standing MWNT-based matrices is based on the self-organization of colloidal particles [1]. This method affords the creation of a hexagonal close-packed (hcp) monolayer of polystyrene microspheres (PS). Figure 5.15 shows 1.71 µm PS-particles, which are arranged in a close-packed monolayer. The AFM image (Fig. 5.15 C) reveals a well ordered structure, which is nearly free from dislocations over a large area. However, a number of point defects are visible. The thus-obtained masks were used as templates for the assembly of MWNTs.

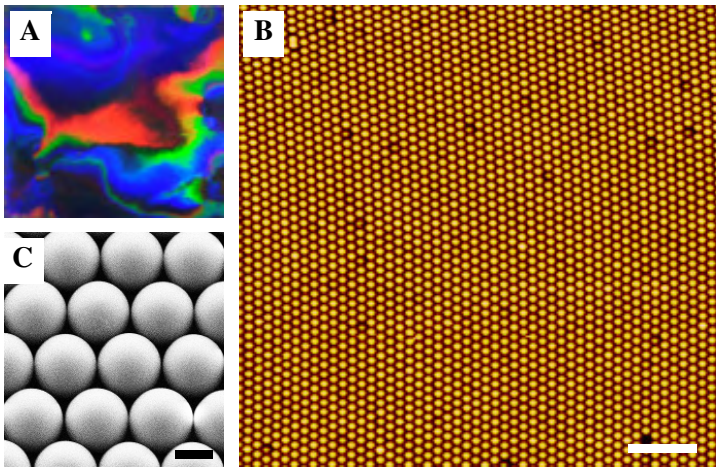

Figure 5.15: *Digital camera picture (A), SEM (B) and AFM (C) images of a typical polystyrene mask deposited on a silicon substrate and subsequently used for carbon nanotube assembly. Scale bar: 10 µm (B) and 1 µm (C).*

The growth of MWNT/PE multilayer films was examined using SEM. Figure 5.16 shows a carbon nanotube layer after the first deposition cycle. MWNTs follow the morphology of the spheres,

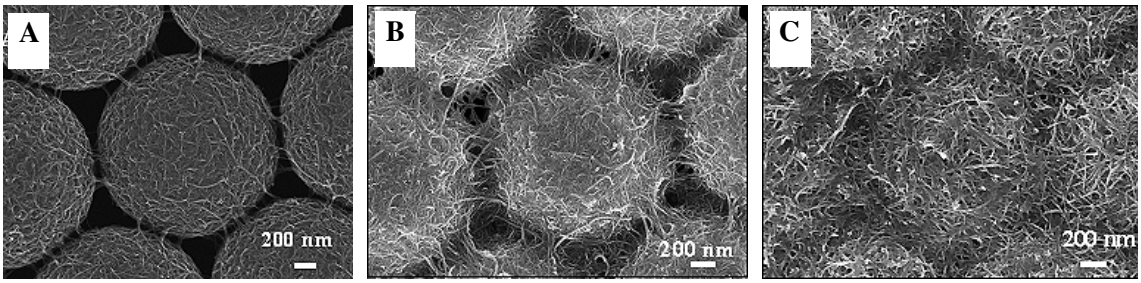

Figure 5.16: *SEM images of the LBL-grown MWNT-PEI/PSS composites deposited on polystyrene particles after various numbers of deposition cycles: one bi-layer (A), four bi-layers (B), ten bi-layers (C) of MWNT-PEI/PSS.*

thereby maintaining the 2D ordered structure. As a consequence, the deposition process leads to the formation of a layer with well-defined micro-nanotopography. The created layer possesses sufficient depth to wrap the entire surface around the spheres. In addition, only few carbon nanotubes provide bridge connections between neighboring spheres. The presence of these connections indicates that carbon nanotube deposition takes place only on the upper surface of the particles, without infiltration within the interstices. Moreover, the individual carbon nanotubes are interpenetrated and homogeneously dispersed within the polylelectrolyte, without any sign of phase segregation. As shown in Fig. 5.16, MWNTs connections increase with the growth of MWNT/PE multilayers. After deposition of ten carbon nanotube layers, the gaps between the spheres are fully covered (Fig. 5.16 C).

To obtain free-standing MWNT-based matrices, the films were peeled off from the substrate through chemical delamination (see section 4.1.2.2). The thus-obtained black compact films could be cut into pieces of a desired size. Fig. 5.17 shows a CNT-based film on a polystyrene mask covering the silicon substrate (A) and a free-standing LBL film after delamination from the substrate (B). The thickness of the free-standing film could be determined from SEM images and was found to be around 2 µm (deposition cycles n = 30).

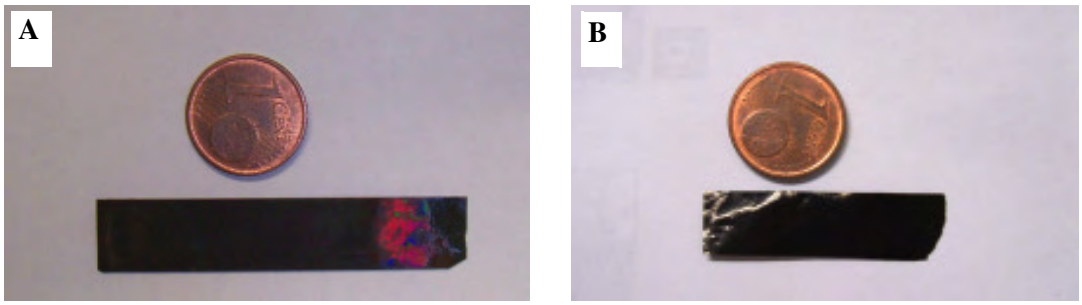

Figure 5.17: *Digital camera pictures of a CNT-based film created on a polystyrene mask (A) and its free-standing form obtained after chemical delamination (B).*

Figure 5.18 shows a scanning electron micrograph of the morphology of the film before and after chemical delamination. THF etching completely removes the latex particles. However, it leaves a thin polyelectrolyte membrane. This polymer residuum was created due to the infiltration of the polyelectrolytes into the gaps between the microspheres during the LbL composite fabrication.

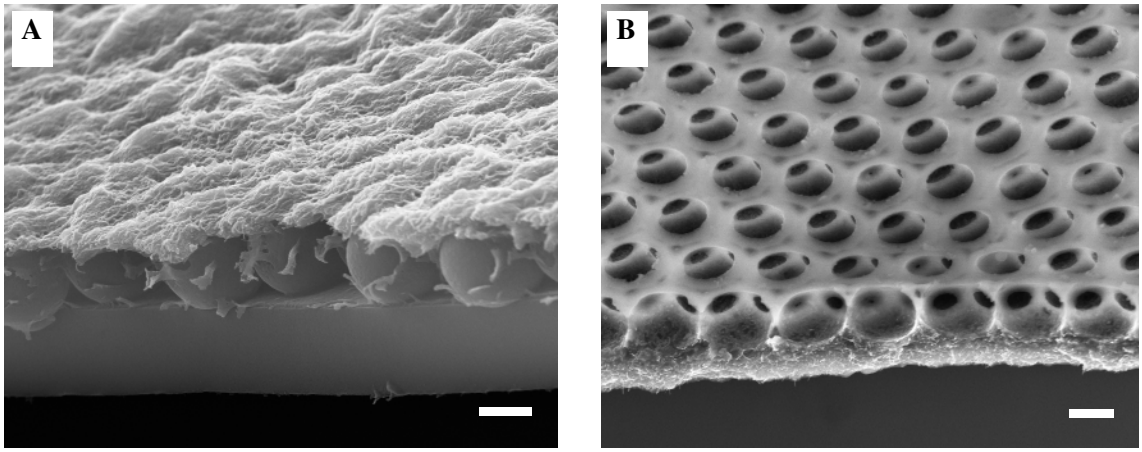

Figure 5.18: *SEM micrograph of a MWNT-based film (A) before and (B) after chemical delamination of the latex. Scale bar: 1 µm.*

Despite THF treatment, it was not possible to remove this polymer membrane. Therefore, to dislodge residual material from the surface, reactive ion etching (RIE) was employed. During RIE, the ions of the plasma react with the surface atoms forming compounds or molecules, which subsequently leave the surface thermally or as a result of the ion bombardment. The etch rates were determined by controlling the structural changes of the film after 40 s of etching. SEM investigations show the morphology of the film during various stages of O_2 and O_2 + Ar etching. For 25 % O_2 + 75 % Ar, the initially porous membrane disappeared leaving a polystyrene residuum on the edge of the cavities (Fig. 5.19 A).

Progressively decreasing the argon flow rate and thereby, increasing the oxygen ion concentration, leads to efficient polymer etching. As shown in Fig. 5.19 D, optimal etch conditions have been found for O_2 flow rates equaling 20 sccm. Moreover, the same image reveals that the RIE process induces morphological changes affecting the surface. The originally smooth surfaces became rough with the carbon nanotubes randomly sticking out. A detailed examination of these exposed MWNTs indicates that the oxygen plasma not only removes the polymer residuum but also the superficial polyelectrolyte layer. Figure 5.19 D also indicates that carbon nanotubes can withstand this etching process, which leaves them practically undamaged [1,3]. As has previously been reported, plasma etching results in the formation of highly polar surfaces of the carbon nanotubes [4] and does not affect the mechanical properties of the MWNT-based matrices [5]. Thus, we can assume that oxygen etching under these experimental conditions results in no detectable change in the mechanical properties of the MWNT-based matrices.

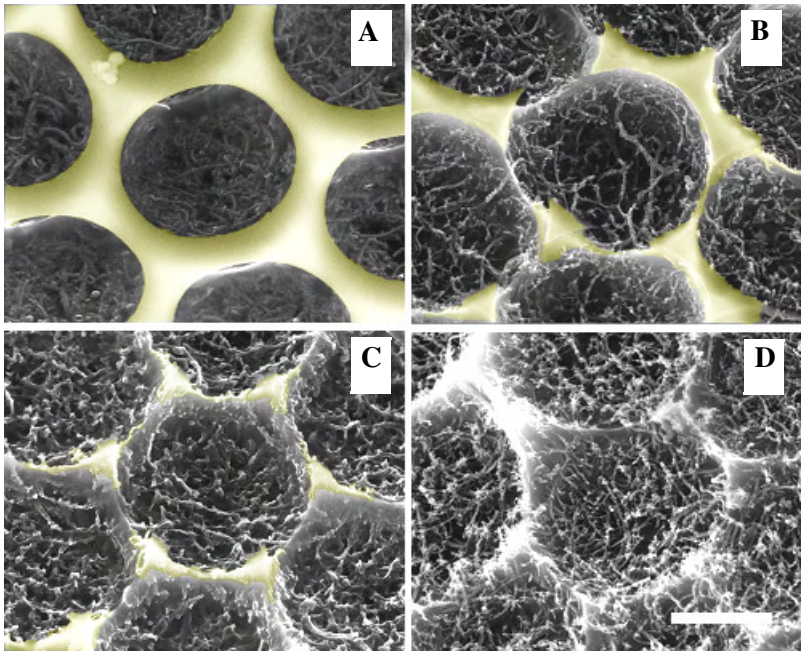

Figure 5.19: *SEM images after following RIE processes: (A) 25 % O_2 + 75 % Ar, (B) 50 % O_2 + 50 % Ar, (C) 75 % O_2 + 25 % Ar, (D) 100 % O_2. Scale bar: 1 µm.*

Figure 5.20 shows the final complete network architecture consisting of successive layers of cross-linked carbon nanotubes that self-assemble into ordered structures. The film, as a free-standing matrix, is characterized by controlled geometry, surface topography, and chemical composition [5].

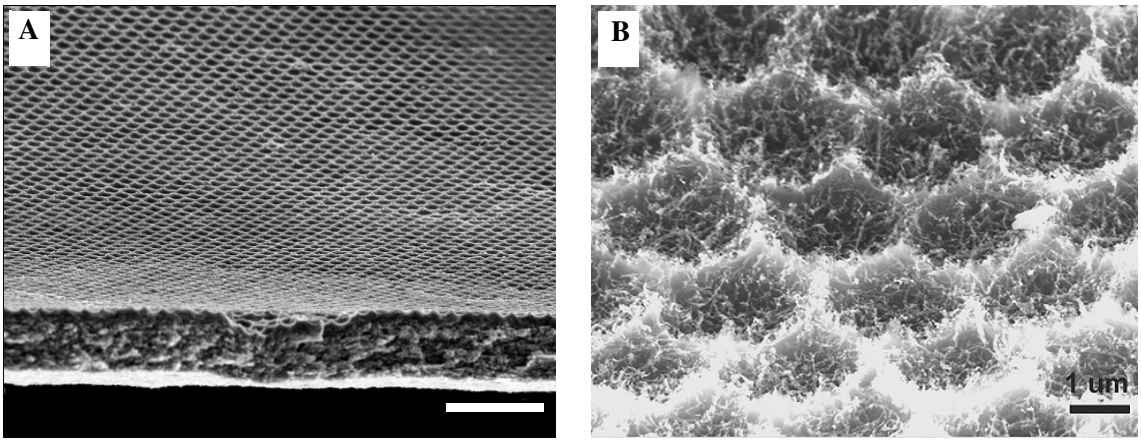

Figure 5.20: *SEM image of the final free-standing matrix made up of carbon nanotubes arranged in a regular network of micro-cavities. Scale bar in A: 10 µm.*

As mentioned before, the NSL technique combined with a LbL assembly process was employed to produce a model system with both the exceptional nanotopography and nanochemistry to explore the cellular response to carbon nanotube-based materials. The methods presented here offer many advantages. In a simple manner, carbon nanotubes can be assembled into monolayers

with a cavity-like structure. Since the cavity dimension is related to the polystyrene microspheres, their diameter can easily be changed by formation of the polystyrene mask from particles of various sizes. Additionally, the methods used guarantee considerable chemical stability of the self-assembled monolayers and allow for high reproducibility in manufacturing.

5.1.2 VACNT matrices

Vertically-aligned carbon nanotubes were obtained using a plasma enhanced chemical vapor deposition process (PECVD), described in detail in section 4.1.4.

A typical image of catalytically-grown carbon nanotubes is presented in Fig. 5.21. The produced nanotube arrays exhibit perfect vertical alignment and a very good separation between the individual CNTs. The diameters and lengths of randomly distributed nanotubes is around 50 nm and 10 µm, respectively.

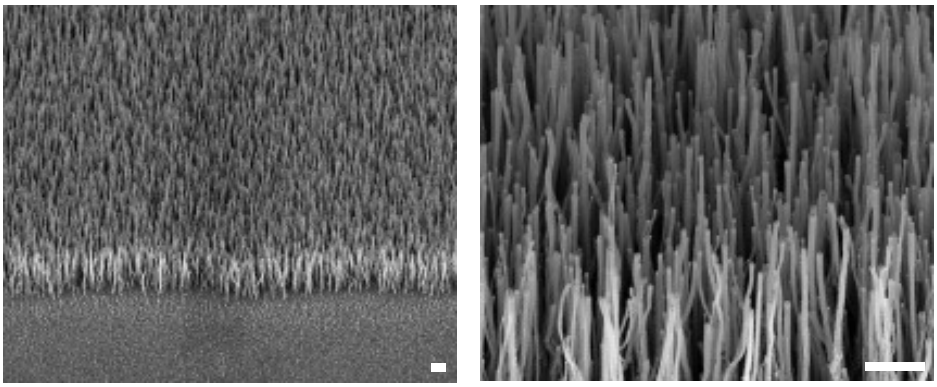

Figure 5.21: *SEM image of a "carpet" composed of aligned nanotubes grown perpendicular to the silicon substrate. Scale bar: 1 µm.*

Substrates with periodically-aligned nanotubes show that the position of the nanotubes corresponds to the honeycomb pattern of the nickel catalysts. On most of the periodic islands, only single nanotubes were grown. However, as illustrated in the enlarged SEM image (Fig. 5.22, right), double growth also took place. This defect may arise from improper PECVD

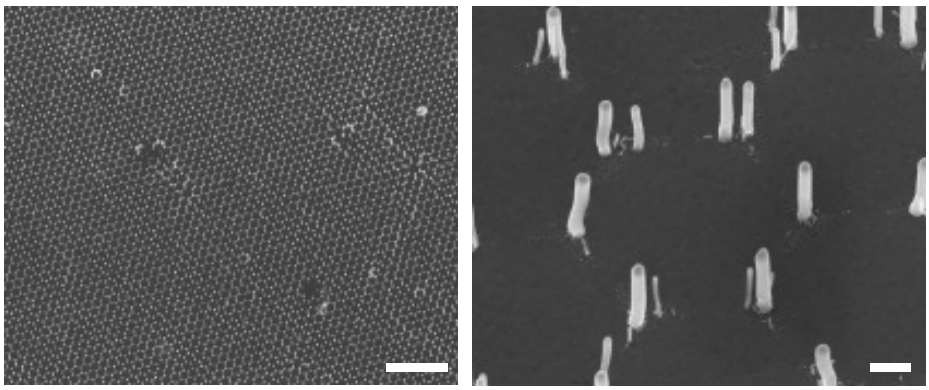

Figure 5.22: *SEM images showing an array of vertically-aligned carbon nanotubes with periodic distribution on a sapphire substrate. Scale bar: 5 µm (left) and 100 nm (right).*

parameters as well as from improper preparation of the nickel structure. Probably, the final step in the substrate preparation, i.e. the annealing phase, influences the creation of additional smaller catalytic centers surrounding the main growth core, which subsequently contributes to the growth of shorter and thinner carbon nanotubes. This imperfection can be eliminated by replacing the quasi-triangular catalyst islands by round catalyst dots [7]. Periodically-aligned CNTs are 50 nm in diameter and ~ 5 μm in length.

5.2 Nanoindentation experiments

In addition to a controlled geometry and surface chemistry, the predescribed matrices (section 5.1.1) need to possess specific mechanical properties to be able to maintain the predesigned structure and correct tissue reconstruction. The mechanical strength and flexibility of these matrices is particularly important in bone tissue engineering where scaffolds are placed in load-bearing regions. Carbon nanotubes, which are used in this study as the main building material, exhibit outstanding mechanical properties (see section 2.1.2). Therefore, the produced matrices are expected to fulfill the mechanical requirements for the scaffolds. Moreover, the used LbL deposition technique allows the fabrication of a matrix with a high concentration of carbon nanotube contents, even up to 50 % [8] and a uniform distribution of the CNTs in the polymer matrix.

While numerous studies have focused on the characterization of the tensile properties of LbL composites [8-10], in this study the mechanical properties of CNT-based matrices have been evaluated using a nanoindentation technique. All tests were conducted for each sample under the same, fixed experimental conditions (see 4.2.2) with a Berkovich and a conical tip. Young's modulus and hardness were calculated from recorded load-displacement curves.

The elastic modulus and the hardness of MWNT-PEI/PSS composites are presented in Fig. 5.23 as a function of contact depth. The results obtained using a Berkovich and a conical tip are consistent for each sample.

Figure 5.23 reveals that the elastic modulus is relatively independent of the indent depth for all polymeric composites. However, the hardness exhibits a monotonically decrease with regard to small loads. This behavior of H and E_r as a function of the contact depth is consistent with previously-reported observations [11]. Since nanoindentation tests were carried out in at least seven independent areas of the samples, the relatively small standard deviation of the data points indicates the high homogeneity of the composites.
The reduced modulus of the MWNTs-PEI/PSS films (0.49 ± 0.15 GPa) is comparable to that obtained for PEI/PSS composites (0.44 ± 0.02 GPa). The same refers to the hardness (0.015 ± 0.006 GPa and 0.007 ± 0.002 GPa).

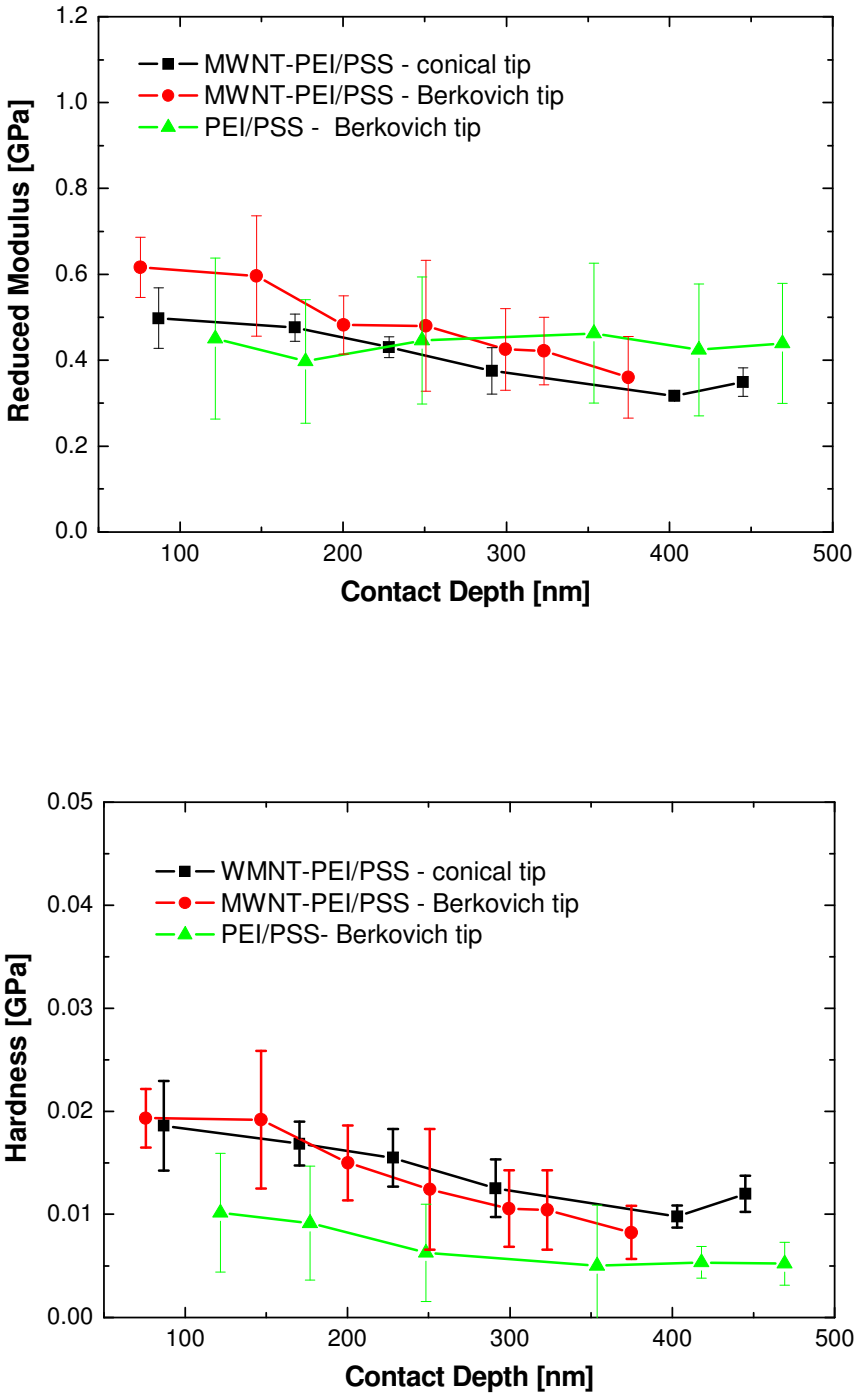

Figure 5.23: *Reduced modulus and hardness as a function of contact depth. Data obtained for different LbL heterostructures at a load/unload rate of 40 μN/s and 20 s hold time, probed with a Berkovich and a conical diamond tip.*

The obtained results clearly demonstrate that the presence of carbon nanotubes within the polymeric matrix does not improve the nanomechanical properties of the composite. These observations are consistent with the previously-mentioned study on nanoindentation of LBL multilayers from MWNTs and PAH [12]. Pavoor *et al.* showed that MWNT/PAH composites possess poorer mechanical properties in comparison to the corresponding polymeric matrices. These results confirm that a high concentration and a homogeneous distribution of MWNTs within a polymer matrix as well as a strong adhesion between the structural components are insufficient to provide a reinforcement of the composites (in terms of hardness and Young's modulus obtained from nanoindentation experiments). Carbon nanotubes have extraordinary axial mechanical properties that play an important role in the reinforcement of the tensile properties of the materials. It was shown that LBL assembly composites from MWNTs exhibit a remarkably high tensile strength that is as high as that observed for ceramics [13]. It has been suggested that the flexibility of carbon nanotubes and their curved morphology reduce the reinforcement action [6]. Even strong interconnectivity between the CNTs and the host polymer does not lead to a significant increase of the nanomechanical reinforcement under indentation load. The indenter can easily displace carbon nanotubes; thus, the mechanical response of the composite is close to that of the local polymer matrix.

The nanoindentation tests reveal that the mechanical response of the investigated samples is mainly affected by the polymer matrix. To support this claim, carbon nanotube-based heterostructures with different polymer compositions were fabricated. The differences in the mechanical response of these samples are presented in Fig. 5.24.

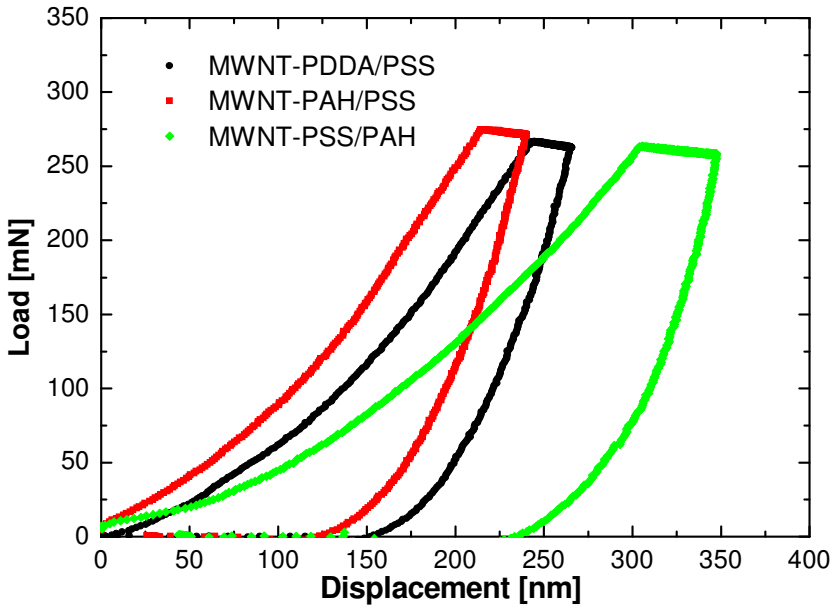

Figure 5.24: *Load-displacement curves of different samples. Reduced modulus and hardness calculated from those plots are: MWNT-PDDA/PSS E_r = 1.84 GPa and H=0.043 GPa; MWNT-PAH/PSS E_r = 2.39 GPa and H = 0.062 GPa; MWNTS-PSS/PAH E_r = 1.52 GPa and H = 0.021 GPa.*

Load-displacement curves show that MWNT-PSS/PAH composites exhibit a softer nature than the other structures. At the maximum indentation force (300 μN), the indenter penetrates deeper, resulting in a displacement of 350 nm. For the MWNT-PAH/PSS, the indenter reaches a depth of 240 nm, which points to a larger hardness of this matrix. The corresponding values of Young's modulus and hardness confirm those observations: E_r = 2.23(43) GPa and H = 0.062(17) for MWNT-PAH/PSS, E_r = 1.84(39) GPa and H = 0.043(12) for MWNT-PDDA/PSS, E_r = 1.52(28) GPa and H = 0.021(7) for MWNT-PSS/PAH.
The obtained results demonstrate the great influence of the composition of the polymer on the mechanical response of the composites.

In order to estimate the coefficient of friction of MWNT-based composites, nanoscratch experiments were performed. A conical diamond tip was used for these experiments. The coefficient of friction was calculated for all samples using data from the constant force tests. Several scratches were made in different areas of the samples. The collected data were then averaged and the coefficient of friction calculated as the ratio of lateral to normal force. In Fig. 5.25 the average values of μ (coefficient of friction) are presented as a function of scratch length. There are no sudden changes in the coefficient of friction indicating that any cracking or failure of the film occurred [14]. The MWNT-PEI/PSS film displays a significantly higher coefficient of friction compared to the PEI/PSS composite. The average value of μ of the MWNT-PEI/PSS film against a diamond tip is calculated to be 0.69(3) and the average coefficient of friction of PEI/PSS: 0.35(2). These data display a considerable adhesion and friction for MWNT-PEI/PSS films. We assume that the increased value of the coefficient of friction of the MWNT-based composite is a result of high composite homogeneity and strong interconnectivity between

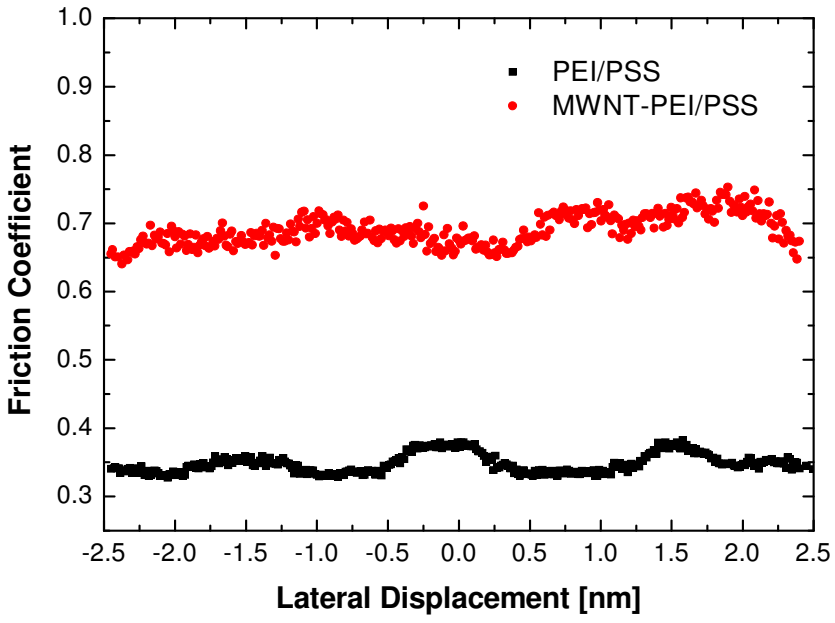

Figure 5.25: *Coefficient of friction as a function of the lateral displacement.*

the polymer matrix and the carbon nanotubes. Moreover, the LBL method ensures a high concentration of carbon nanotubes; thus, they may form a well-tangled network that may play an important role as a resistant against the diamond tip during the scratch experiments.

Nanomechanical tests carried out on the different compositions of polymers and carbon nanotubes show that the presence of MWNTs within polymeric matrices does not considerably improve the mechanical properties of the respective composite. Due to the flexibility of the nanotubes and their curvy morphology, the obtained elastic modulus and hardness have been found to reflect the mechanical response of the surrounding matrix. Additionally, data obtained from the nanoscratch tests reveal that carbon nanotube-based composites display significant adhesion and friction. This can be explained by the strong interconnectivity and adhesion between the MWNTs and the polymer as well as the resistive role of tangled nanotubes against the tip.

5.3 Cellular response to the CNT-based matrices

The topography and the surface chemistry of the fabricated matrices are very interesting features for fundamental studies of cell interactions. It has been shown that *in vitro* cells sense the surface topography and chemistry of artificial extracellular matrices [15-18]. Therefore, CNT-based matrices with unique micro- and nanotopographical structures and chemistry may have significant effects on cellular behaviors. However, the possible cytotoxicity of carbon nanotubes may rule out an *in vivo* use of CNT-based matrices [19-21]. For that reason, one of the most important tasks is the evaluation of the biocompatibility of the fabricated samples. In this section, the morphology, mitochondrial activity, and adhesion of the osteoblast cells are used as an indication of the relative cytocompatibility of the CNT-based substrates *in vitro*.

5.3.1 MWNT-based matrix

The role of nano-sized features in complex nanostructured substrates as well as their surface chemistry were tested for their ability to promote cell growth. For these experiments, nanostructured matrices were incubated with HOB-C, human hipbone osteoblast cells, in full culture medium at 37 ^{o}C (for details, see section 4.1.5.1) and investigated by SEM, MTT- and Bradford-assay.

5.3.1.1 Cell morphology

SEM was the primary tool used to determine the morphology of osteoblast-like cells. Figure 1.12 shows SEM micrographs of osteoblast cells grown for 7 days on a MWNT-based matrix. The cells are flat with a visible cell nucleus protruding in the center (Fig. 1.12 B). Moreover, the cells are

well-spread and cover nearly the entire surface. Typical cell diameters for flat osteoblasts were of the order of 40 µm, which is similar to the one for osteoblasts found on the surface of natural bone [22]. The shape of the osteoblast cells is an indication of the biomedical compatibility of the CNT-based matrix. It is known that cells in a rounded configuration divide at a lower rate than flattened ones. Moreover, cells attached to a surface but barely spread will show lower proliferation rates than those with a greater spreading. Conducted SEM studies reveal that the produced MWNT-based matrices allow a flattening and spreading of the osteoblasts, showing an adequate cell shape for proliferation.

Cell adhesion to a substrate influences cell morphology as well as cell proliferation and differentiation [23]. Therefore, one can say that the adhesion of cells to the surface of a matrix is one of the major factors responsible for its biocompatibility. SEM investigations, carried out at high magnification, reveal the morphology of physical contacts between the cells and the carbon nanotube matrix. As shown in Fig. 1.12 C, the cavity-like structure can be seen beneath the part

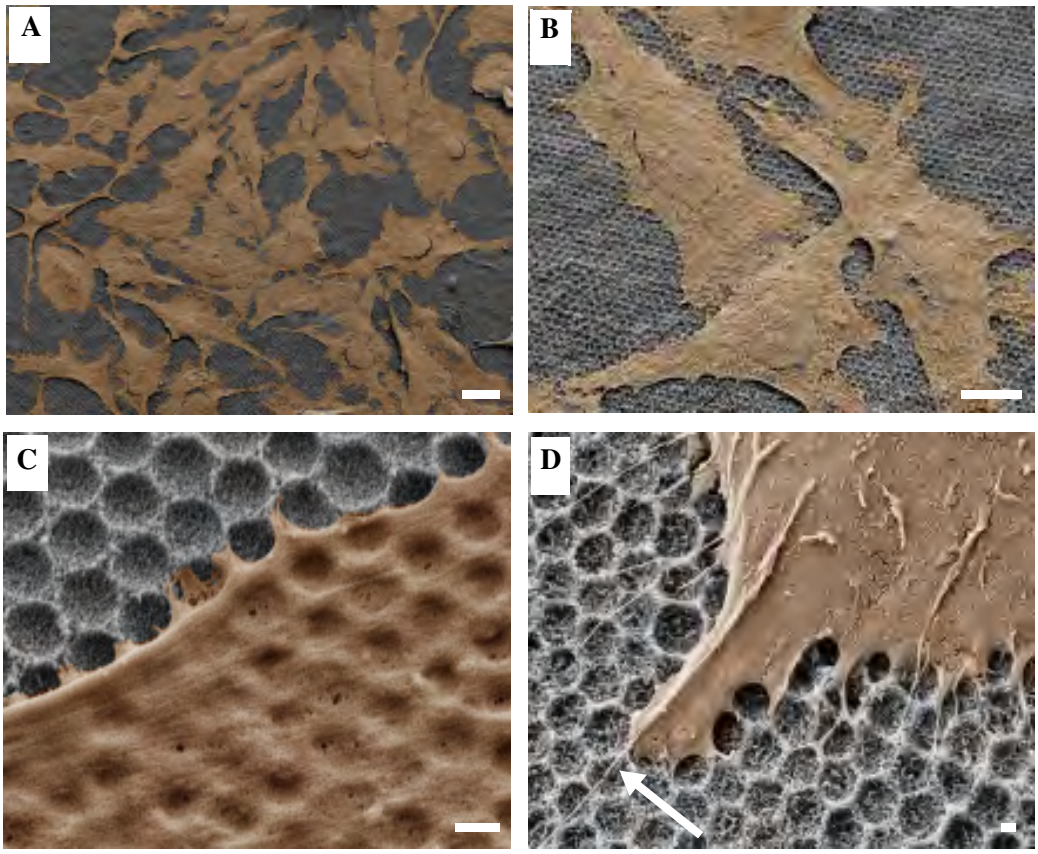

Figure 5.26: *SEM pictures showing the morphology of osteoblast-like cells and their physical contact with the carbon nanotube structure. (A) The flat cell bodies extend over almost the entire area of observation. (B) The cell nucleus protrudes in the center. Scale bar: 10 µm. (C), (D) A cell with a long threadlike cytoplasmic prolongation (arrow). Scale bar: 1 µm. For better cells visualization, the gray-scale was pseudo-colored with graphic software.*

of the cell body, which strongly suggests the presence of tight junctions and adhesion mechanisms in the matrix. Since osteoblast cells are anchorage-dependent cells, adhesion is a precondition for

subsequent cell functions [23]. SEM investigations also reveal the presence of thin, threadlike cytoplasmic prolongations (Fig. 1.12 D). These pseudopods have a diameter in the range of 10 to 20 nm, close to the size of the MWNT's diameters.

The qualitative assessment of the cell morphology showed no significant difference between osteoblasts attached to a CNT-based topography and a standard plastic coverslip used as a control.

5.3.1.2 Cellular viability

The main concern regarding the use of carbon nanotubes in biomedical applications is their possible cytotoxicity [19-21]. Therefore, testing of CNT-based composites on living organisms is essential for the successful utilization of such materials. Up to now, only a few reports have demonstrated the biocompatibility of CNT-based substrates with various cell cultures. MacDonald *et al*. [24], for example, showed that collagen-CNT hybrids sustain smooth muscle cell viability. Chemically-modified carbon nanotubes have been demonstrated to be a suitable scaffold material to grow neuron and osteoblast cells without affecting cell activity [10,26,27]. Taking into account these contradictory opinions regarding CNT's toxicity, the produced matrices were tested for their biological compatibility with an osteoblast cell culture. To examine this compatibility, the mitochondrial activity as well as the proliferation of the cells were observed.

Qualitative information about the biocompatibility of MWNT-based matrices was obtained from observations with an optical microscope. It has been figured out that cells were viable on all matrices and continued to grow for at least 10 days in culture.

Furthermore, the viability of osteoblast-like cells seeded onto MWNT-based matrices was studied by an MTT cell viability assay. In this test, yellow tetrazolium salt (MTT) is reduced to purple formazan in the mitochondria of living cells. This reduction only takes place when mitochondrial reductase enzymes are active. Thus, the conversion can directly be related to the number of viable cells. Figure 5.27 shows the viability data of HOB-cells cultivated for 7 days on the CNT-based surface with the cavity-like topography. In contrast to cells on glass, osteoblasts on the CNT matrix exhibit higher absorbance. This optical density measurement of the solubilized formazan crystals shows that the carbon nanotubes do not interfere with osteoblast viability. In other words, the produced matrices are able to support a long-term survival of cells, which suggest that CNT-based matrices are non-toxic to this particular cell-culture line.

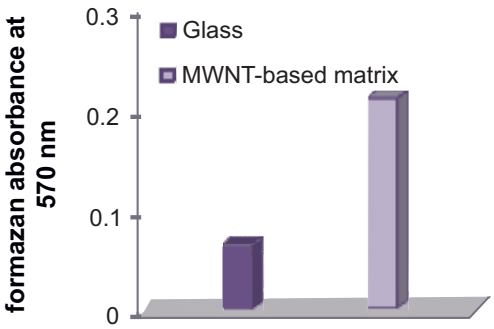

Figure 5.27: *Viability of osteoblast cells evaluated by an MTT assay after 7 days. Optical density measurement of the solubilized formazan crystal shows an increase in osteoblast viability in the contact with the CNT matrix.*

Figure 5.28 shows the number of proliferated cells after 1, 3 and 7 days, respectively. It can be seen from the graph that the proliferation rate of the cells grown on the carbon nanotube matrices is higher than those of the control in each case. The results of this experiment indicate that the greater cell number on MWNT-based matrices might be attributed to the cavity-like topography with nanoscale roughness. Based on the characteristics of MWNT-based matrices presented in chapter 5.1.1 it is known that created matrices possess an exceptional topography with an average diameter of 50 nm for the CNTs and 1.5 µm for the cavities being periodically arranged on the surface. These size features, similar to the nanoscale protein fibrils in natural ECM, are expected to promote osteoblast cell proliferation.

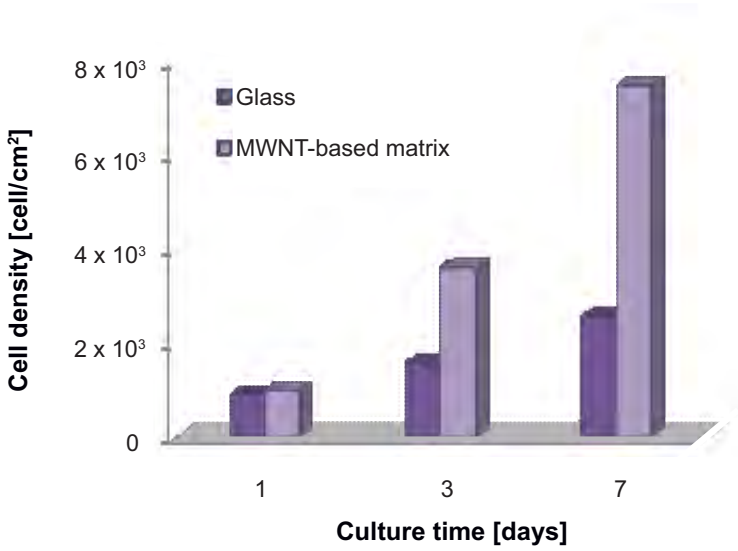

Figure 5.28: *Osteoblast proliferation on glass coverslip and CNT-based matrix with cavity-like structure after 1, 3 and 7 days.*

These observations are consistent with earlier studies, which demonstrated the importance of nanometer roughness for the controlling of osteoblast functions [25]. Some *in vitro* studies with nanophase biomaterials have shown that cells respond differently to materials with nanoscale roughness compared to microsize roughness materials. Price *et al*. [26], for example, reported that nanometer dimensions of fibers promote osteoblast cell proliferation.

5.3.1.3 Surface chemistry

It is well-known that apart from the surface topography, cells are also sensitive to differences in the chemical properties of materials. Many studies reported that variations in the chemistry of the outermost functional groups of a surface evidently affect the cell response [27-31]. This phenomenon is related to the extracellular protein adsorption [32]. Shortly, the first molecular event that takes place by exposure of the scaffold to a biological fluid, whether it is a serum or a cell culture medium, is the protein adsorption [33]. These proteins form a conditioned interface to

which the cell responds. Moreover, accessibility of cell adhesive domains (i.e. RGD sequence of adsorbed fibronectin) may either enhance or inhibit following cellular adhesion and growth. The type, concentration, conformation, and bioactivity of proteins adsorbed onto materials depend on surface chemistry but also on charge, hydrophilicity or hydrophobicity, topography, roughness and energy [34]. This paragraph, however, will focus on the surface charge and chemistry, and its influence on the concentration of adsorbed proteins.

It is commonly accepted, that possible protein adsorption may be driven by various interactions, which can arise from (i) van-der-Waals forces, (ii) dipolar or hydrogen bonds, (iii) electrostatic forces, and (iv) hydrophobic effects. Given the apparent range and strength of electrostatic forces, it is generally accepted that the surface charge plays a major role in protein adsorption [35].

To address the role of chemical functionalities on carbon nanotubes, protein adhesion and subsequent cell proliferation were studied on MWNTs with amine ($–NH_2$) and carboxyl groups (–COOH). Additionally, polyelectrolyte films with various surface charges were studied. The carbon nanotubes were chemically modified and deposited on silicon substrates according to the methods described in section (see 4.1.2.2). Because of its stability and the fact that it is the most abundant protein found in human blood [36], bovine serum albumin (BSA) was chosen as a model for protein adsorption. Since the net charge of the BSA as well as the degree of weak polyelectrolyte ionization, such as PAH, is pH dependent, all experiments were conducted at the same physiological pH of 7.4. Surface charges of functionalized CNTs, polyelectrolytes, and BSA are summarized in Table 5.3.

Tab. 5.3: Protein, polyelectrolytes, and CNTs used in this study

protein/polyelectrolyte/ functionalized CNTs	isoelectric point (pI)	net charge at pH 7.4
BSA	4.9 [35]	–
PAH	8.8 [35]	+
PSS	negative charge in the whole pH range [37]	–
PDDA		+
CNT-PAH		+
CNT-COOH	negative charge in the whole pH range [38]	–

A qualitative estimation of BSA adsorption onto various LbL composites was obtained by incubation of LbL-matrices in Coomassie Blue G-250. This dye, commonly used for protein quantification, binds to amino acids, which shifts the absorption of the dye from 465 nm to 595 nm. The color change or dye-protein complex formation is shown in the digital camera picture in Fig. 5.29. In the case of a control sample (A) without adsorbed proteins, the dye keeps its reddish/brown color, in contrast to the samples B-F, where the blue color clearly confirms the

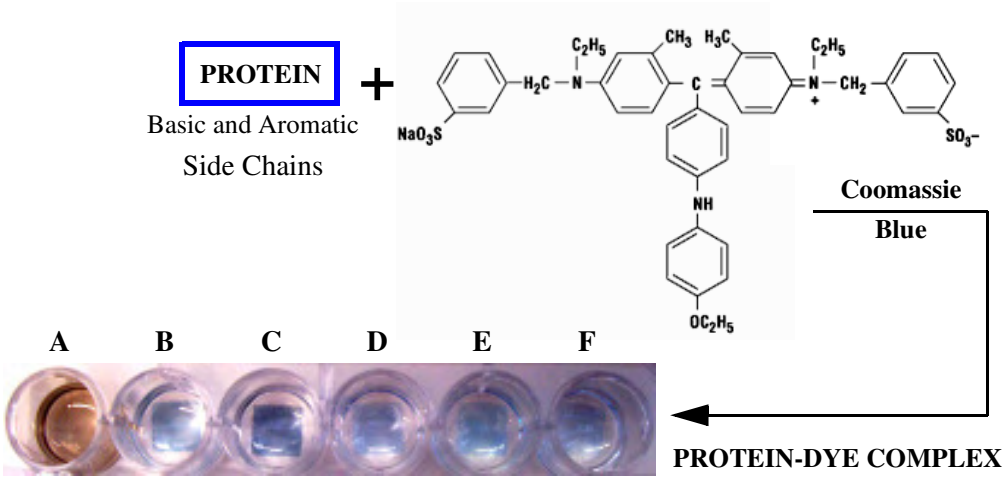

Figure 5.29: *Schematic reaction for the Coomassie dye with the BSA protein adsorbed on substrates with multilayers of (B) MWNT-PAH, (C) MWNT-COOH, (D) PDDA/PSS, (E) PSS/PAH, (F) glass and (A) glass without protein, immersed in Coomassie G-250.*

presence of BSA on the LbL multilayers. UV-vis absorption spectra taken from these substrates are presented in Fig. 5.30. These spectra show an absorption peak at around 600 nm, which is characteristic for the dye-protein complex. The height of the absorption peak differs for each sample. This is due to the difference in the amount of adsorbed BSA protein onto a particular substrate. Therefore, the height of these peaks gives qualitative information on the BSA adsorption with respect to the surface charge.

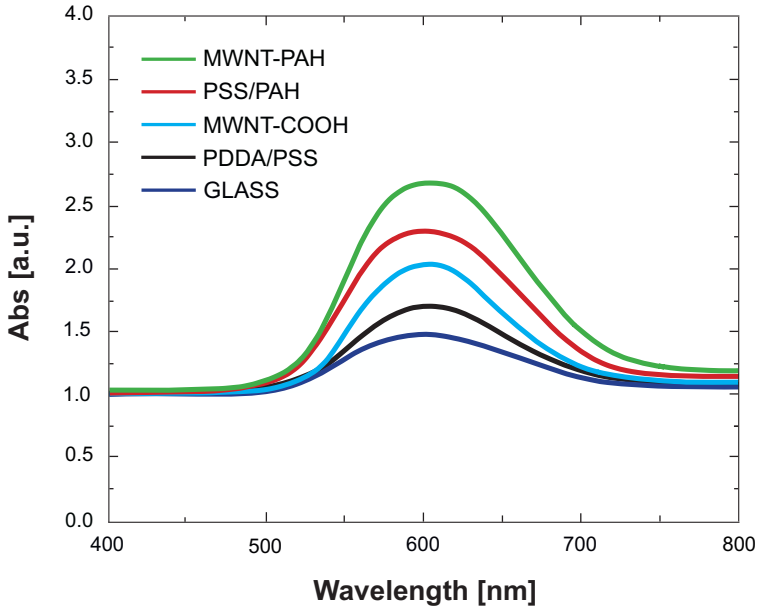

Figure 5.30: *Absorption spectra taken from MWNT-PAH, PSS/PAH (PAH - upper layer), MWNT-COOH, PDDA/PSS (PSS - upper layer) and glass with adsorbed BSA protein. BSA (1 mg/ml) was deposited for 1 h at 37 ^{o}C.*

A significant difference in protein adsorption can be observed between positively and negatively-charged surfaces. The films made up from MWNT-PAH and PSS/PAH, which have oppositely-charged surfaces with regard to the protein are more effective at promoting protein adsorption. The lowest protein adsorption was found for glass. The thus-obtained results suggest the major role of electrostatic interactions in BSA adsorption, but it is clear that BSA still adsorbs on like-charged surfaces. As the protein charge is the net sum of positive and negative charges on the biomolecules, it could be possible that patches of positive charge are responsible for adsorption on negative surface [39]. However, Salloum *et al.* have shown that by decreasing the strength of electrostatic interactions, the adsorption of BSA was independent of the ionic strength for the like-charged surface; leading to the conclusion that adsorption on like-charged surface is due to nonelectrostatic interactions [35].

To quantify the total amount of BSA protein adsorbed on the multilayers, a Bradford protein microassay was used [40]. Each protein concentration was calibrated using a calibration curve. The achieved results, summarized in Table 5.4, confirm the qualitative information obtained from UV-vis spectra. The LbL film with a MWNT-PAH as an outer layer is particularly effective in BSA adsorption (0.054 mg/cm^2). For comparison, the adsorption of protein on the film with MWNT-COOH was 0.033 mg/cm^2. The difference in BSA quantity on both positively-charged MWNTs-PAH and PSS/PAH films can be explained by the differences in the topography of the multilayers. This factor complicates the interpretation of the protein adsorption between polymeric and CNT-based LbL films, but simultaneously indicates that not only surface chemistry but also roughness influence protein adsorption.

Tab. 5.4: BSA protein adsorption quantity on various LbL multilayers.

MULTILAYERS	**SURFACE CHARGE**	**PROTEIN ADSORPTION AMOUNT mg/cm^2**
$(PSS/MWNT\text{-}PAH)_5$	positive	0.054(11)
$(PDDA/MWNT\text{-}COOH)_5$	negative	0.033(8)
$(PSS/PAH)_5$	positive	0.040(12)
$(PDDA/PSS)_5$	negative	0.023(4)
GLASS	negative	0.013(2)

These results are compliant with previously reported studies of the surface charge effect on the adsorption behavior of various proteins. Salloum *et at.* [41] and Muller *et al*. [42], for instance, found that the interaction of proteins with polyelectrolyte multilayers strongly depends on the sign of the charges for both, the multilayers and the proteins. Schwinte *et. al*. [43] showed the differences in BSA adsorption among polyelectrolyte mulitilayers with PSS and PAH-outer layers, which was highest for positively-charged PAH.

As mentioned before, proteins adsorbed on the substrate mediate the interaction of the material with the cells. Cells, in turn, attach and adhere to these adsorbed proteins through adhesive molecules called integrins [44]. These transmembrane molecules interact with the matrix through their extracellular domains, with components of the cytoskeleton, and they also signal molecules through their intracellular domains. For that reason, the type and quantity of adsorbed proteins play a crucial role in integrin activation and subsequently adhesion, cell morphology regulation, growth, and differentiation. Foregoing results showed that surfaces with positively-charged carbon nanotubes are more favorable to BSA adsorption. This might indicate a better biocompatibility of CNT-PAH over CNT-COOH and, consequently, a better cell adhesion and proliferation. To confirm this assumption, osteoblast cells were seeded on both substrates and their proliferation was studied.

Figure 5.31 shows the response of the osteoblast cells to positively- and negatively-charged carbon nanotubes after 3 days of incubation. This qualitative observation suggests that cells grow well on both substrates, however there is a considerable difference in osteoblast proliferation.

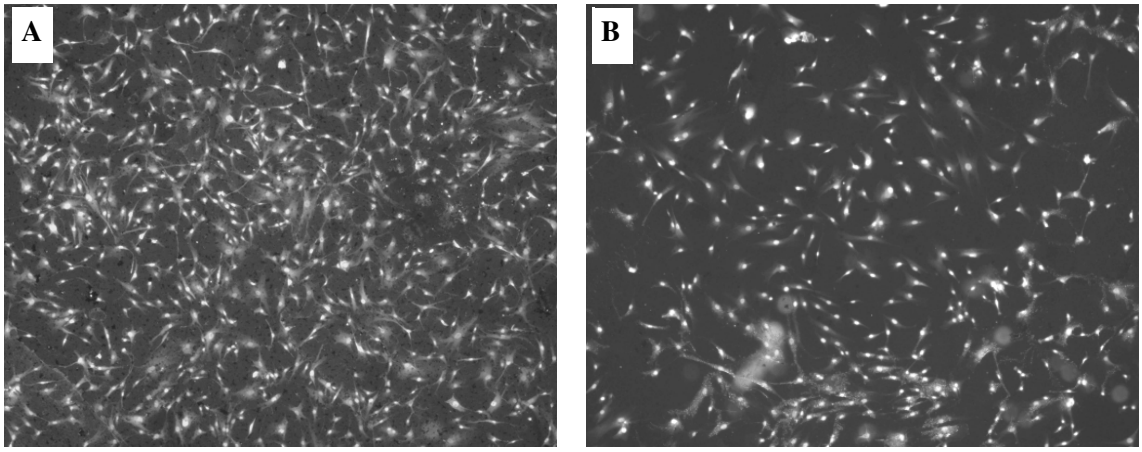

Figure 5.31: *Fluorescent microscopy pictures of osteoblast cells grown on (A) positively charged CNTs - amine group, negativelycharged carbon nanotubes - carboxylic functionality (B).*

The LbL film with positively-charged carbon nanotubes exhibits a higher number of attached cells than the multilayer with the negatively charged surface. The fluorescent microscope investigation indicates that carbon nanotubes with carboxyl functionalities are less effective in promoting osteoblast cell adhesion and, consequently, their proliferation. These observations are confirmed by quantitative results presented in Fig. 5.32. It is clearly visible that MWNTs-PAH carbon nanotubes best support HOB cell growth. Cell counts obtained from negatively charged MWNT-COOH are significantly lower, indicating that the presence of negative electric charges doesn't favor osteoblast proliferation and growth.

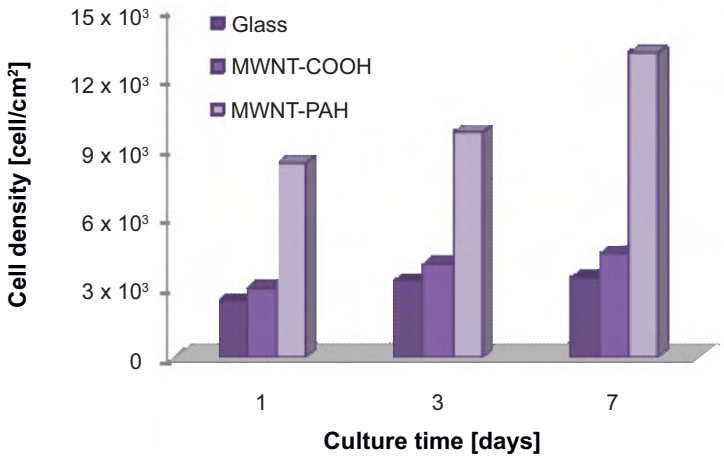

Figure 5.32: *Graphical representation of osteoblast cell proliferation on MWNTs-PAH and MWNTs-COOH after 1, 3 and 7 days.*

The thus-gained results clearly demonstrate that differences in the surface chemistry of carbon nanotubes significantly influence adhesion and proliferation of osteoblast cells. These results are consistent with a previously reported study on the viability of osteoblast-like cells and their adhesion on differently-functionalized carbon nanotubes [22].

Osteoblast cells were also seeded onto multilayer films made of PSS/PAH with an outermost PAH layer. As can be seen in Fig. 5.33, for a solely polyelectrolyte film, there are very few cells in comparison to LbL-multilayers with PAH-functionalized MWNTs or even with COOH-functionalized carbon nanotubes, where the amount of adsorbed BSA was lower than on the PSS/PAH film (see Tab. 5.4). The observed differences in osteoblast growth arise from the variation in surface roughness between the LbL multilayers. The increased surface area and nanoscale features present on MWNT-based films, presumably provided more available sites for protein adsorption and, thus, altered the amount of cellular interactions, which subsequently enhanced growth of osteoblasts.

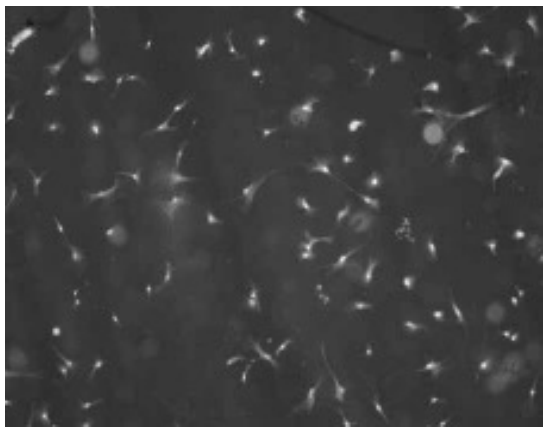

Figure 5.33: *Fluorescent microscopy image of osteoblasts cultured for 3 days on the polymeric film with an outermost PAH layer.*

The above-mentioned results from the *in vitro* studies highlight the essential role of the matrix's surface characteristics with regard to osteoblast adhesion and proliferation. Variation in surface chemistry and roughness of the material may significantly affect the response of the cells. On the basis of the investigated surface chemical properties of CNT-based LbL films, it can seen that matrices made up from carbon nanotubes functionalized with PAH are particularly effective in BSA adsorption and, consequently, in osteoblast growth and proliferation.

5.3.1.4 Osteoblast cell response to MWNT-based surfaces modified with bioactive calcium phosphate nanoparticles

The ease with which carbon nanotubes can be functionalized, together with their excellent mechanical properties, explores their potential for bone tissue engineering applications. It has been shown that adequately functionalized carbon nanotubes could successfully be used as scaffolds for the growth of artificial bone mineral (hydroxyapatite mineralization) [45]. Moreover, the presence of different chemical groups on the modified nanotubes allows for the further functionalization with bioactive objects, in this way improving the biocompatibility of the CNTs.

In this section, a novel approach for the modification of MWNT-based matrices with calcium phosphate nanoparticles is presented. Calcium phosphate nanoparticles (CP NPs) have been chosen due to their biocompatible properties. As it is well-known, calcium phosphate belongs to one of the most investigated materials for bone tissue engineering. The interest in it arises from the fact that the skeletal system contains about 70 % of inorganic material made up of calcium phosphate [46]. Due to its close chemical and crystal resemblance to bone mineral, calcium phosphate has an excellent biocompatibility. Numerous *in vivo* and *in vitro* assessments have reported that calcium phosphate supports the attachment, differentiation, and proliferation of osteoblast cells [47,48]. Based on these results, CNT matrices with bioactive nanoparticles are expected to provide a more desirable growth environment for the HOB-cells compared to the CNT matrices without attached nanoparticles.

The MWNT-based matrices fabricated from non-covalently functionalized carbon nanotubes were placed in a solution containing bioactive calcium phosphate nanoparticles (see 4.1.3). After 1 h of incubation the samples were rinsed with water, dried, and imaged by SEM. The morphologies of the CNT matrices before and after incubation in the nanoparticles solution are presented in Fig. 5.34. These micrographs show that the matrix did not change its cavity-like topography. However, carbon nanotubes, previously well visible on the surface, are mostly covered by calcium phosphate nanoparticles. The SEM study indicates the successful deposition of CP nanoparticles.

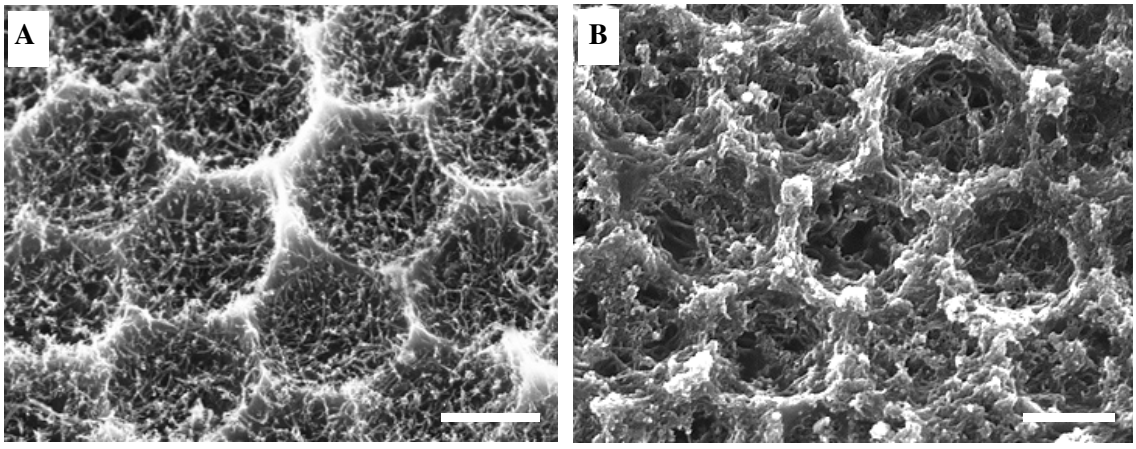

Figure 5.34: *SEM images of a CNT-based matrix before (A) and after (B) incubation in the CP NPs solution. Scale bar: 1 μm.*

Direct evidence for the attachment of CP NPs to the PAH - functionalized carbon nanotubes is given in transmission electron microscopy images. Figure 5.35 shows a TEM image of a single carbon nanotube being completely decorated with calcium phosphate nanoparticles. The nanoparticles could be attached covalently to the CNT's surface through interaction between the amine functionalities on the CNT surface and carboxylic acid groups on CP NPs stabilized with 2-carboxyethylphosphonic acid (CEAP) [46].

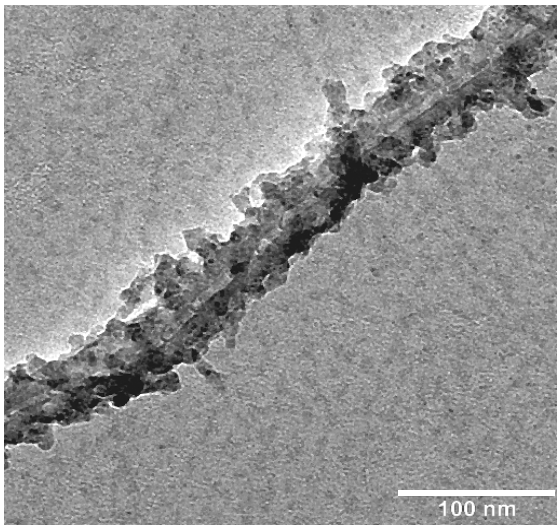

Figure 5.35: *TEM image of MWNTs homogeneously coated with calcium phosphate nanoparticles.*

Additionally, in order to verify the presence of CP NPs on carbon nanotubes, the samples were analyzed by energy dispersive X-ray spectroscopy (EDX). The obtained spectrum (Fig. 5.36) provides data to support the presence of calcium, oxygen, phosphorus and carbon, as expected for calcium phosphate nanoparticles and carbon nanotubes.

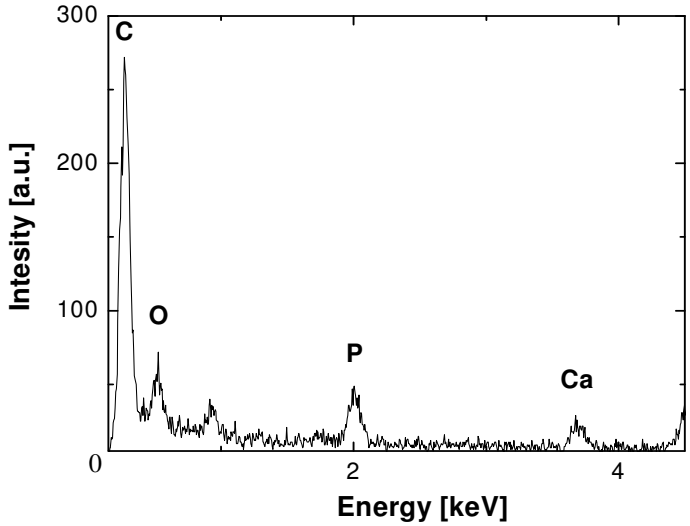

Figure 5.36: *EDX spectrum of carbon nanotubes coated with calcium phosphate nanoparticles.*

Based on the results described in the previous paragraphs and the fact that CP NPs exhibit a very close chemical resemblance to bone mineral, one can assume that MWNT-based matrices enriched with CP particles will significantly affect osteoblast behavior, i.e. enhance cell adhesion and further proliferation. To confirm this supposition, osteoblast cells were seeded onto MWNT-based matrices, which were decorated with calcium phosphate nanoparticles. As a control, a matrix without CP NPs was used.

In Figure 5.37 micrographs showing HOB-cells growing on matrices with and without bioactive nanoparticles are presented. It can be seen that after the first day there was no difference in cell density between the cells growing on modified CNT-based matrix (Fig. 5.37 A, 1d) and the cells on the control (Fig. 5.37 B, 1d). However, on the third day, the average cell area was higher on the matrix with CP NPs, reflecting the higher surface coverage by the cells.

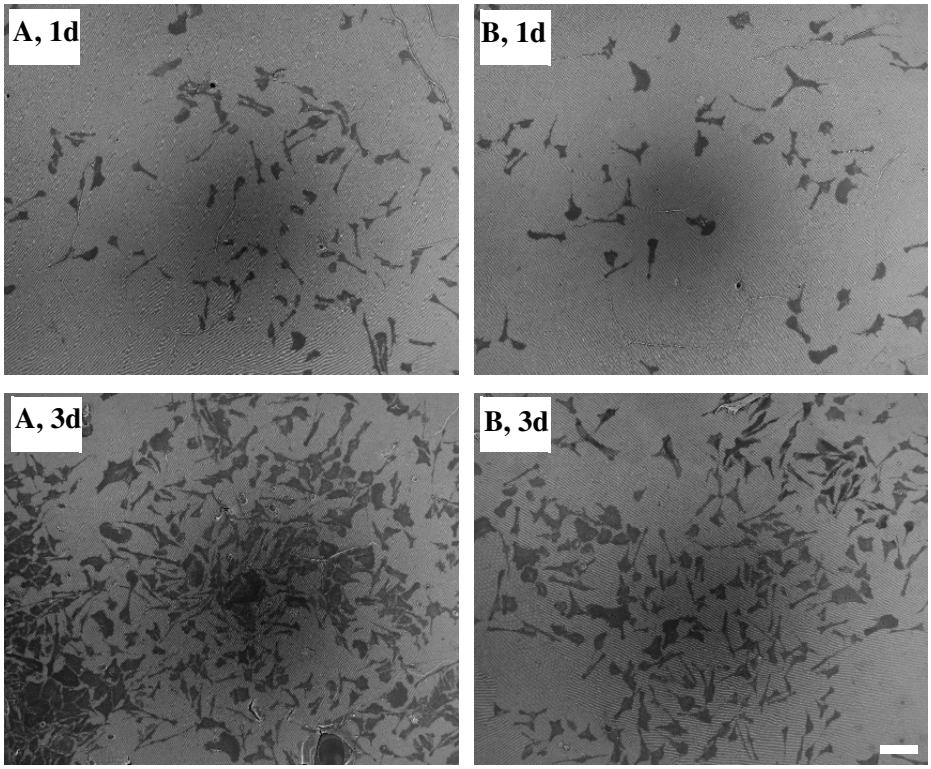

Figure 5.37: *Representative SEM pictures of osteoblast cells cultured on MWNT-based matrices functionalized with (A) and without (B) CP NPs after 1 day and 3 days. Scale bar: 100 µm.*

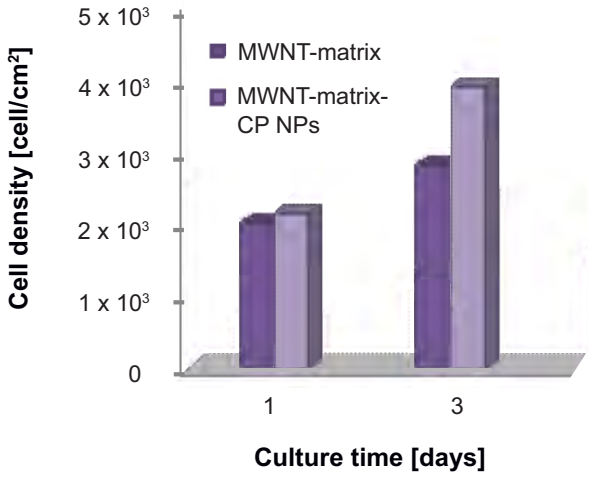

Figure 5.38: *Graphical representation of the osteoblast density on MWNT-based matrices with and without CP nanoparticles.*

The enhanced osteoblast proliferation on MWNT-based matrices modified with bioactive nanoparticles is confirmed by proliferation studies, which results are shown in Fig. 5.38. As expected, the number of osteoblasts was higher on the matrices enriched with calcium phosphate nanoparticles.

Taken together, the results presented here demonstrate that LbL assembled composites from MWNTs can be successfully modified with CP NPs, which in turn lead to effective increasement of their biocompatibility with osteoblast cells.

5.3.2 VACNTs matrices

On the basis of the cellular response to CNT-based matrices with cavity-like topography, it seemed promising to study the interaction and the interfacial dynamics of osteoblast-like cells with vertically-aligned CNTs. It is expected that especially the effect of the CNT's periodicity might be useful for the modulation of cell adhesion, growth, and migration. While many studies focusing on cell interaction and migration on patterned surfaces have shown that the morphology and orientation of the cells change in response to micro-scale topographies [49-51], relatively few reports have studied the response of the cells to nano-scale topographies and, particularly, to carbon nano-pillars. Rovensky *et al.* [52], for example, studied the behavior of mouse fibroblasts on random arrays of silicon whiskers. Other works have studied the response of human fibroblasts and endothelial cells to silicone elastomeric pillars [53,54]. Based on the results from those studies, we investigated the behavior of human osteoblast cells adhered to arrays of vertically-aligned carbon nanotubes [55].

Using the chemical vapor deposition process and nanosphere lithography, substrates with nano-pillars, i.e. carbon nanotubes with well-defined heights and interpillar gaps could be produced (see 5.1.2) and used to study the response of osteoblast cells. Cell morphology on both, a carpet of vertically-aligned CNTs and periodical VACNT-arrays as well as cell-nanotube connections have been investigated by means of SEM.

Figure 5.39 illustrates the morphology of osteoblasts growing on a CNT-carpet. Cells are flattened, well spread and attached to the tips of individual CNTs. In comparison to conventional plastic dishes, the cells clearly preferred to adhere to CNT tips. Additionally, osteoblast cells seem to exert forces upon CNTs by attaching to the tips of the nanotubes. As revealed in a higher magnification image (Fig. 5.39 C), the nanotubes appear to be stressed and deflected under cellular forces. A similar effect has been reported in a system made up of microneedles [56] and on patterned carbon nanotubes [57].

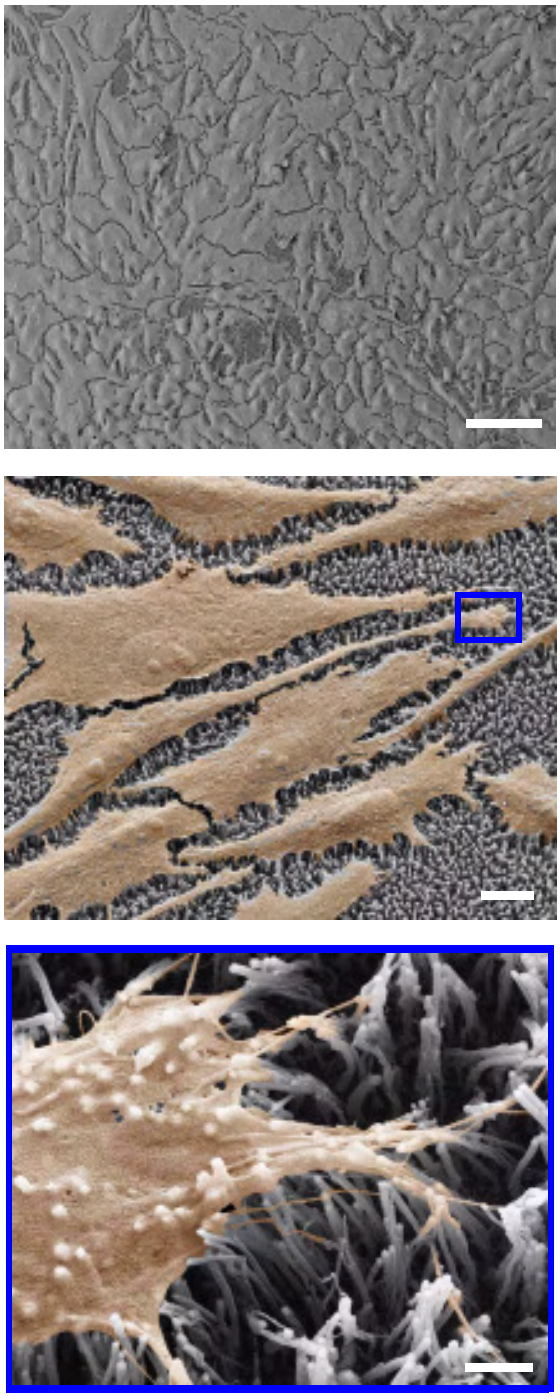

Figure 5.39: *Color-enhanced SEM images depicting the morphology of osteoblast cells growing on a carpet of vertically aligned carbon nanotubes. Cells are flattened with their visible nucleus located in the central part of the cell. Scale bar: 100 µm, 10 µm, 1 µm, respectively.*

The effect of the periodicity of VACNTs on cell attachment and morphology was also assessed. Figure 5.40 clearly demonstrates differences in cell morphology and behavior on vertically-aligned CNTs organized in a hexagonal pattern. An adaptation of the cells to these patterned CNTs appears to influence their shape and orientation. Osteoblasts respond to CNTs by changing their

morphology. As in the case of the CNT-carpet, the attachment of osteoblast cells occurs on the tips of periodically-aligned CNTs. As shown in Fig. 5.40 B, cells do not reach down to the surface between the carbon nanotubes, but remain fixed to their tips, suspended above the sapphire surface. Moreover, osteoblasts growing on this substrate produce many cell

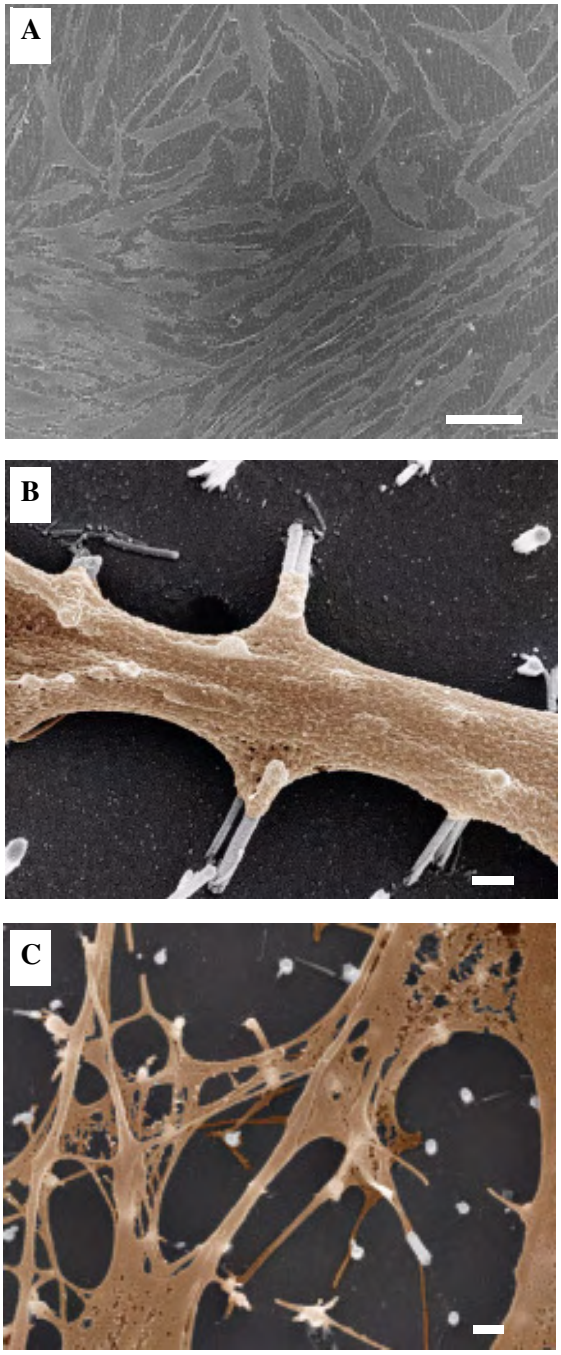

Figure 5.40: *Color-enhanced SEM images depicting guidance of osteoblast cells facilitated by periodically-distributed VACNTs (A). The fiber extending from the cell body interacts with the CNTs and deforms them to assist in its elongation and morphological changes (B). The cell extensions are consistent with the dimension and distribution of aligned nanotubes (C). Scale bar: 100 µm.*

extensions (Fig. 5.40 C). The presence of these extensions on periodic VACNTs is consistent with the observed alignment, as cell extensions are responsible for cell movement and surface sensing. The effect of surface topography on cell adhesion was also assessed by an evaluation of the focal adhesion protein development after 24 h of culture. By immunofluorescence staining, both vinculin abundance and colocalization with the cytoskeleton has been studied. Vinculin belongs to a plasma membrane-associated protein found in focal adhesions which is involved in the coupling of the actin-based microfilaments to the adhesion plaque. Due to the fact that vinculin is one of the most prominent proteins of the focal adhesions, it has been used as an ideal marker protein to label focal contacts formed in osteoblasts adhered to VACNTs [58].

The results presented in Fig. 5.41 show that vinculin (green) and actin (red) distributions differ depending on whether they are on a smooth surface (glass) or on a nanopatterned one (VACNTs). In general, cells on glass reveal a random distribution of vinculin throughout their cell bodies.

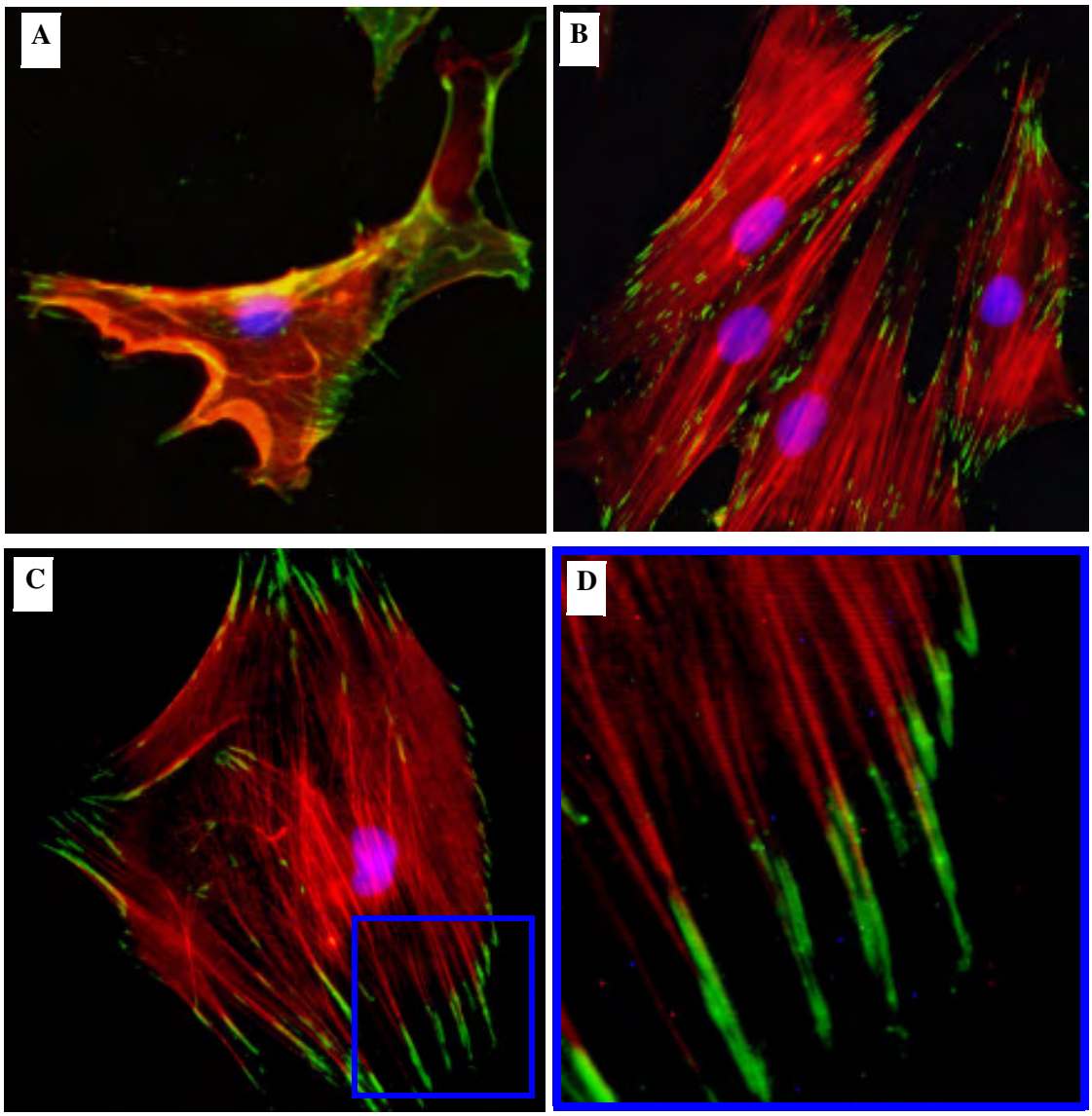

Figure 5.41: *Immunofluorescence images of osteoblast cells stained for actin (red), vinculin (green) and nucleus (blue). Cells adhering to glass (A) and VACNTs (B-D).*

Besides, actin filaments are non-organized into stress fibers. There is no colocalization of vinculin clusters with actin filaments. On the other hand, osteoblast cells, cultured on vertically-aligned CNTs, display a well developed vinculin plaque-like structure. As illustrated in Fig. 5.41 B, the cells show highly tensioned actin filaments organized into large numbers of parallel stress fibers. Additionally, the growing ends of stress fibers are anchored to vinculin clusters (Fig. 5.41 D).

The results presented in this section reveal that topographical features have a significant influence on the attachment and growth of osteoblast cells. Surface topography in terms of the distribution of VACNTs was observed to play an important role in cell shape alteration and influence the direction of their movement. Despite the fact that both surfaces were favorable to cell attachment and proliferation, osteoblast-like cells grew differently on substrates with randomly- and periodically-distributed VACNTs. It was observed that the alignment of osteoblast-like cells is significantly influenced by the periodicity of individual carbon nanotubes. Furthermore, actin and vinculin staining were used to evaluate the effect of surface topography on the distribution of cytoskeletal elements and focal contacts. Cells growing on VACNTs generated well-organized vinculin clusters at the ends of many actin stress fibers. Taken together, these well-constituted and long vinculin clusters together with the well-organized actin bundles indicate good cell adhesion.

5.4 AFM imaging of cultured osteoblast cells in contact mode

So far, the morphology of osteoblast cells has been investigated by means of SEM. This microscope has proven to be a useful tool for cellular imaging and particularly for the characterization of cell-carbon nanotube interactions. However, despite the high resolution of SEM, the submembranous structure of the cells could not be observed. To be able to explore these cellular structures, atomic force microscopy has been employed. As demonstrated by many researchers, AFM has the ability to visualize cell's topography under physiological conditions, without metal coating or fixation as required by SEM. It has been used to image a large variety of cell types, including fibroblasts [59], endothelial cells [60], osteoblasts [61] or neuronal cells [62].

In this paragraph details will be given on how AFM was used to determine a number of cellular structures and to relate these structures to the cell's mechanical properties investigated in the next chapter (see 5.5).

5.4.1 Imaging cellular structures

All AFM images were collected in liquid environment in height and deflection mode at applied vertical imaging forces between 2 and 5 nN. The images, collected in constant height mode, provide information about the surface topography and produce accurate three-dimensional (3D) images of the cells [63], whereas deflection images highlight changes in elevation (similar to a

first derivative of the height mode image), thus providing images with fine structure details but lacking quantitative height information [64].

Osteoblast cells were investigated in both a fixed and a living state. Typical images of fixed osteoblast cells are shown in Fig. 5.42. In general, fixed cells are extremely robust. Therefore, there is little, if any, effect when using height imaging forces on the specimen's integrity. Additionally, in fixed cells, the resolution is generally higher in comparison to living cells. This can be explained by the difference in softness [65].

The height image in Fig. 5.42 shows the topography of osteoblast cells. The structure observed in the center of the cell corresponds to the cell nucleus underlying the plasma membrane. A fiber-like network can also be observed, in which the filaments are oriented parallel to each other and to the long axis of the cell. This network is evident in both, height and deflection mode images. Similar structures have been observed in adherent cells and have been identified as stress fibers, i.e. bundles of actin filaments. These filaments have been widely recognized in AFM imaging by comparison with fluorescent images and by imaging the same cell after disturbance of the actin fibers with drugs such as cytochalasins [64].

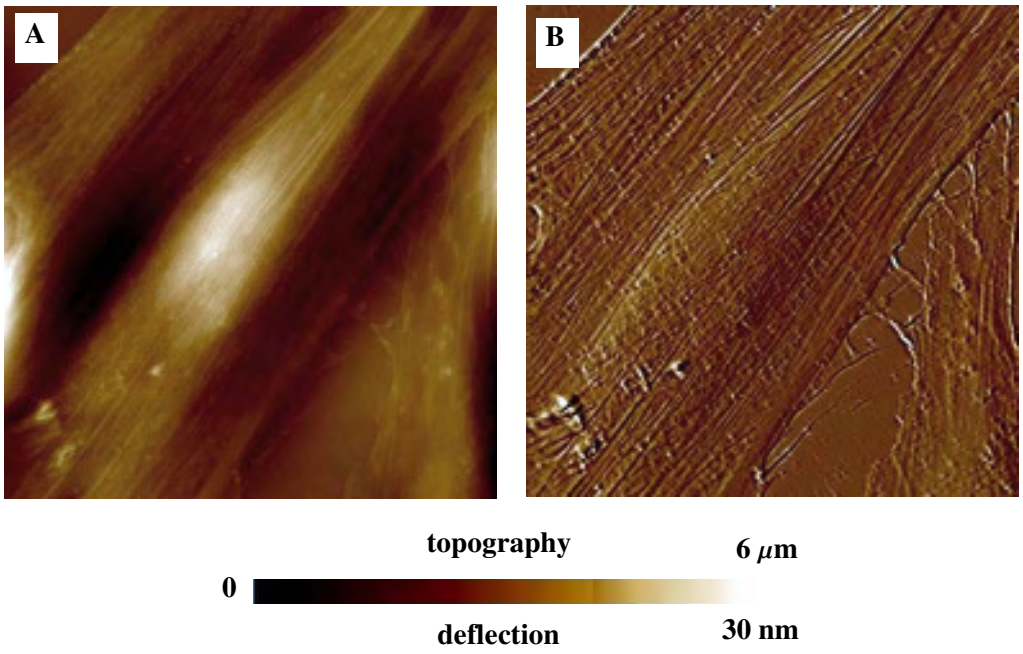

Figure 5.42: *Height (A) and deflection (B) image of cultured osteoblast cells with a visible filament structure corresponding to F-actin. Scan rate 0.7 Hz, with 384 points per line. The scan area for the images is 70 μm.*

Microtubules apparently contribute little to the filamentous structure observed by the AFM. Studies with rhodamine-phalloidin-labeled cells showed that tubulin is mostly concentrated in the perinuclear region of the cells [64]. Confocal microscopy indicated that in these cells microtubules generally lie beneath the actin filaments. Therefore, they are hidden form the AMF tip by the overlaying actin-filament network.

Unlike fixed cells, the softness of living cells resulted in cells surface deformations under the scanning tip causing a significant deterioration of the AFM image quality. To reduce cell-surface deformation and cantilever contamination, the applied cantilever loading force was in the order of 2 nN. Another helpful strategy during imaging living cells, which has been used in the presented AFM studies, is the scanning of a group of cells rather than an isolated cell. This approach allows the cells to exchange lateral forces between each other through cell-to-cell contacts, and hence provides an additional resistance to being dragged by the AFM tip during scanning.

Figure 5.43 shows representative contact images of living osteoblasts. Typical AFM-associated artifacts are visible as streaks present in the direction of the scanning movement (see arrow). These artifacts are due to a high deformation or high friction, which influence the feedback response. As in the case of the fixed cells, cytoskeleton fibers, nuclei as well as cell-to-cell contact regions and overlapping processes could be easily identified.
The measurements confirmed that the AFM can image stiff actin filaments through the plasma membrane without apparent damage to the cell. However, the mechanism by which actin filaments of living cells can be observed by AFM has not been definitively determined.

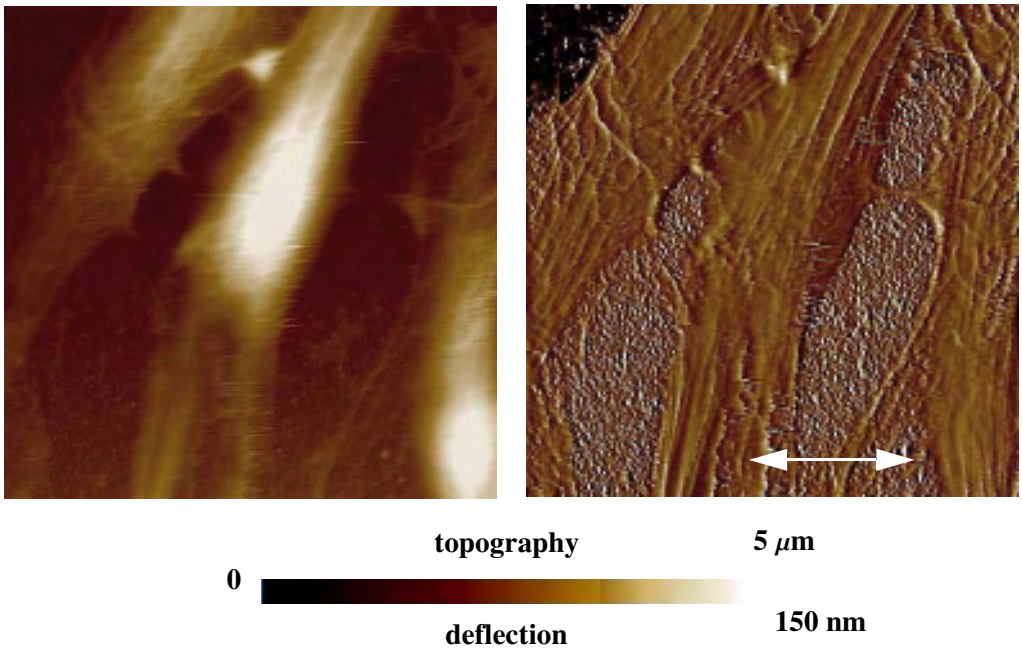

Figure 5.43: *Height (left) and deflection (right) image of cultured living osteoblast cells adhered to a carbon nanotube-based film. Scan rate 0.7 Hz, with 384 points per line. Arrow indicates the scan direction. The scan area for the images is 80* μm.

Figure 5.44 presents the two most reported mechanisms: the membrane deformation model (A) and the membrane penetration model (B). In (A), the scanning tip will follow the contours of the plasma membrane surface, creating a topographical map of the cytoskeletal elements close to the surface, whereas the second model (B) assumes that the scanning tip penetrates the membrane during imaging and makes contact with the stiffer structures below [64].

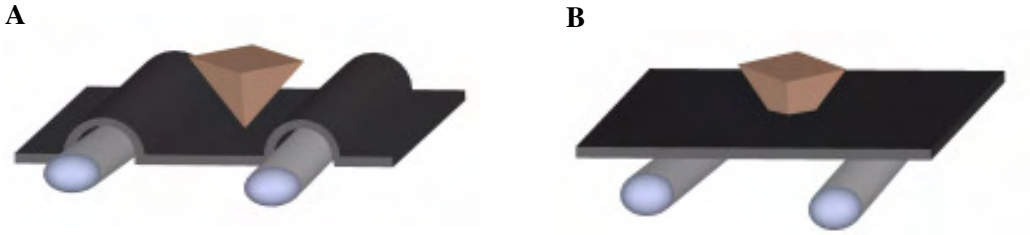

Figure 5.44: *Two possible models explaining the mechanism by which the cytoskeletal features in living cells can be observed. (A) The membrane deformation model: the plasma membrane is flexible and adapts to the contours of the underlying cytoskeleton. (B) The membrane penetration model: the scanning tip penetrates the membrane and contacts the cytoskeleton below.*

Recent results, however, rule out the tip penetration hypothesis. Haydon *et al*. [66] showed that glial cells with the intracellularily-trapped fluorescent dye could be imaged nonivasively using a membrane deformation model. The authors showed that the forces applied by the AFM tip did not cause dye leakage from the cell. These results provide an unequivocal demonstration that the standard AFM tips only deform and do not penetrate living cell membranes while vitally imaging subcellular structures.

Besides the possibility of imaging internal features of living cells, AFM can also be used to observe and record a variety of phenomena, which mainly involve internal processes. One example is cell division as exemplified in Fig. 5.45. This process is particularly evident in constant height mode, where the bright spots correspond to the divided nucleus. The deflection mode also reveals two parallel-connected osteoblast cells with globular forms of nucleus and cytoskeleton filaments.

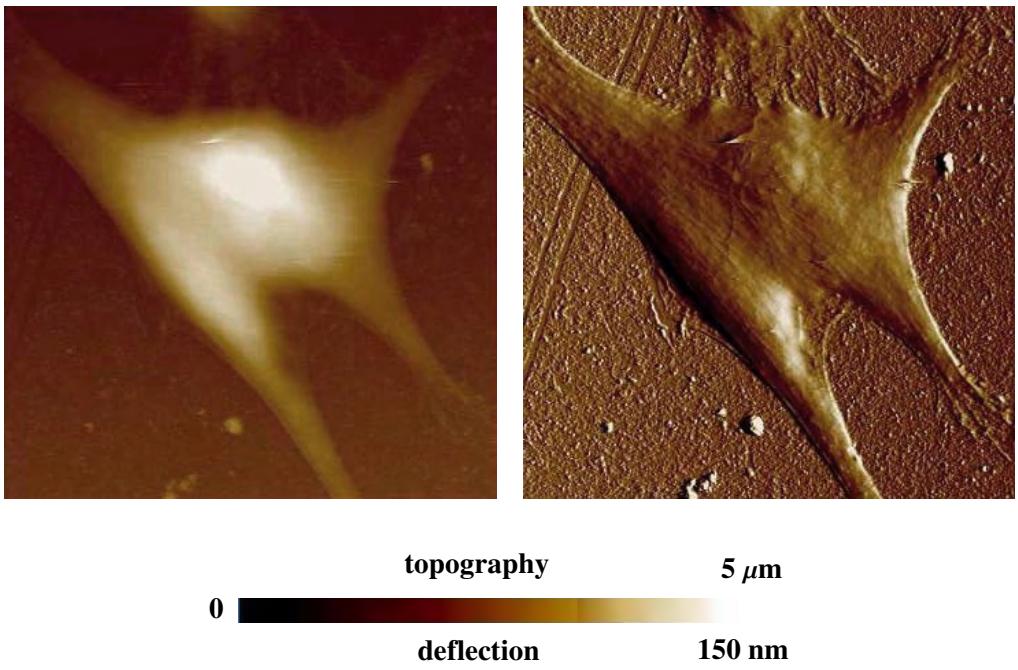

Figure 5.45: *An osteoblast cell undergoing division. The divided nucleus, in constant height mode (left), is clearly visible as the two intense spots. The phenomena are also very well visible in the corresponding deflection mode (right). The scan area for the images is 80 μm.*

AFM appears to be an excellent tool for investigating both fixed and living cells and especially their cytoskeletal architecture beneath the cell membrane. AFM examination allowed to locate the cell nucleus, the interactions of cells with each other, and even cell phenomena which involve internal processes such as cell division. The structures presented above could - most likely - be observed by AFM because of their relatively high stiffness, with the exception of the nucleus, which was visible on account of its large height.

5.4.2 Lateral resolution in AFM imaging of cells

As observed in the preceding paragraph, the quality of the living cell topographic AFM images was lower in comparison to the fixed cell. This difference in lateral resolution arises from the stiffness of the cell, poor adherence to the substrate, and from the loading force and tip geometry. Due to the softness of the living cells, the loading force applied by the cantilever results in an indentation of the tip into the cells. In the case of a soft sample, the AFM tip can cause an indentation depth of several hundred nanometers. Therefore, the contact area between the tip and the sample will be large. Consequently, the obtainable resolution will depend on the contact area, whose value can be used as a measure for the achievable resolution under definite experimental conditions. A theoretical limit for the attainable resolution can be predicted from the Hertz model [67,68]. By replacing δ in Eq. 3.15 with the expression for the contact radius for a conical tip used in this study:

$$r = \frac{2}{\pi \tan\alpha}\delta^2 \qquad \textbf{(Eq. 5.17)}$$

The diameter of the contact area between the AFM tip and the sample can be calculated from the following equation:

$$r = \sqrt{2\frac{(1-\nu^2)F}{\pi \tan(\alpha)E}} \ , \qquad \textbf{(Eq. 5.18)}$$

where F is the loading force, α is the opening angle of the cone (taken as 35^o), v is Poisson's ratio (taken as 0.5, corresponding to an incompressible material) and E is the elastic modulus of the sample.

This radius can be assumed to be the fundamental limit of resolution [65]. Therefore, the resolution can only be improved by further development of the AFM - technique and the accessibility of a softer cantilever. At present, with the softest available cantilevers (10 mN/m), state-of-the-art AFMs can achieve 10 pN force resolution.

Figure 5.46 shows the contact area between the tip and the cell plotted as a function of the elastic modulus for several loading forces. For typical values of the elastic modulus found in living cells (from 1 kPa to 100 kPa) and typical values of loading forces (between 100 pN - 10 nN), contact areas may fluctuate between a few and (even) several hundreds of nanometers.

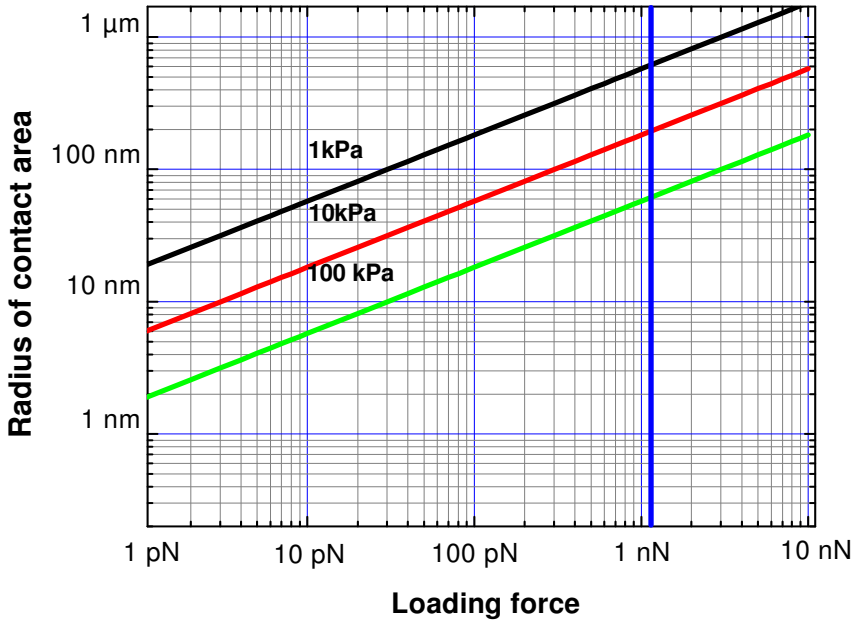

Figure 5.46: *The radius of the contact area between the AFM tip and a soft sample calculated from the Hertz model for a conical tip with an opening angle of 35 degrees. The obtained calculations may serve as a rough approximation of the resolution achievable by the AFM on living cells. The blue vertical line indicates the loading force used in AFM experiments.*

Expected optimum lateral resolution for a loading force of 1.2 nN, as used in this study, will be 600 nm, 200 nm, and 60 nm, if the softness of the cell is 1 kPa, 10 kPa, and 100 kPa, respectively.

5.5 Osteoblast cell-matrix adhesion verified by AFM

The adhesion of a cell to the surface of a substrate is the first phase of cell-substrate interaction. The quality of this adhesion plays an important role in the modulation of cell functions such as morphology, proliferation, protein production and differentiation [69]. Results presented in Chapter 5.3 have confirmed that it is the surface chemistry and the topography of the matrix, which are responsible for the variation in cell morphology, cytoskeleton organization, and proliferation. Since the cytoskeleton is believed to be responsible for the mechanical properties of the cell (see chapter 3.3.1.2), the alteration in its architecture upon adhesion to diverse substrates may lead to changes in the mechanical stiffness of the cell. Moreover, strongly adherent cells are stiffer than cells loosely attached, therefore, by measuring cell Young's modulus, a quantitative

information about the quality of cell adhesion, and concequently biocompatibility of the substrate can be obtained [70-72].

Up to now, a variety of techniques have been used to determine the mechanical properties of individual cells, e.g. micropipettes [73], magnetic tweezers [74], or microneedles [75]. Unfortunately, most of them are not commercially available. Unlike these, atomic force microscopy, apart from being commercially available, offers a high spatial resolution (~ 100 nm), which makes it an important tool for mechanobiological studies.

In this chapter the use of AFM as a tool with the ability to study the biocompatibility of various substrates by investigating the cytomechanical properties of osteoblast cells on a sub-micrometer scale is presented.

5.5.1 Young's modulus

Elastic properties of cells were evaluated from the recorded loading portion of the force-curve by fitting the Hertz model [67,68], which describes the indentation of an elastic sample using a stiff conical indenter. All experiments were conducted under fixed experimental conditions (see 4.2.3). Due to the local variation in cell elasticity, force-curves were recorded only at the central location of the cell, i.e. in the area of the cell's nucleus (see Fig. 5.47). Thanks to it, the variability in Young's moduli values derived from probing different cellular structures, could be minimized. Additionally, Young's modulus was calculated from the force-curves recorded on those cells

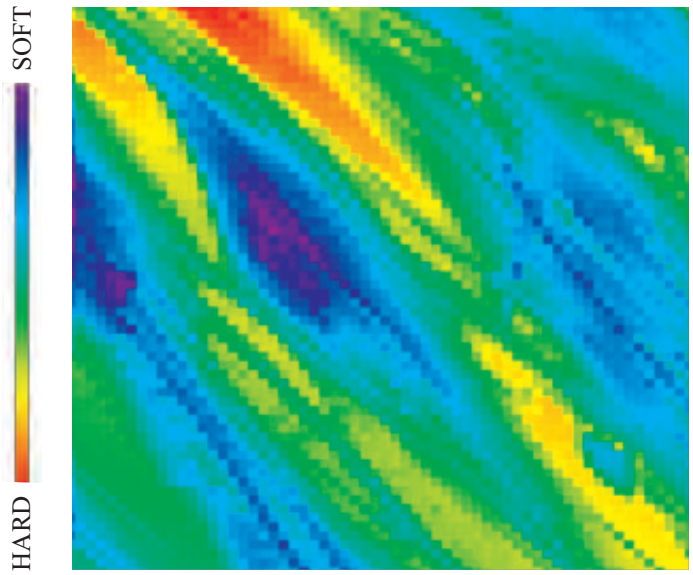

Figure 5.47: *Cell elasticity map obtained in force volume mode (generated from 64 pixel x 64 line force curves). As indicated by the pseudo-color scale (left), cells exhibit local variation in their elasticity. The softest part of the cell is found in its center, where the nucleus is placed. The force-volume image was recorded in a relative trigger mode, with a trigger treshold of 20 nm (max. applied force 1.2 nN). Scan size: 70 μm.*

whose height was over 2 µm. Because of this, any artificially high value of the elastic modulus arising from compressing the soft cell and therefore sensing the stiff substrate could be eliminated. Moreover, to reduce the hydrodynamic drag, force-curves were taken at a low rate of 0.7 Hz. As reported by Radmacher *et al.*, the soft cantilevers bend drastically at high scan rates due to hydrodynamic drag exerted by the liquid and therefore, a constant external force is added to the loading force of the cantilever [76]. To omit this force offset in the force-curve analysis, a low scan rate was used.

Figure 5.48 shows a representative force-curve recorded on a HOB cell seeded on a glass substrate. The contact part of the curve shows the typical nonlinear shape of a soft sample. Due to very gradual changes in the slope of the cantilever deflection, a correct identification of the contact point is difficult; z_c might be anywhere between 500 and 600 nm. Another characteristic feature for the unloading curve is a small adhesive force. Nevertheless, the presence of this adhesive mark does not affect the calculations of Young's modulus, since they are carried out from the loading curves.

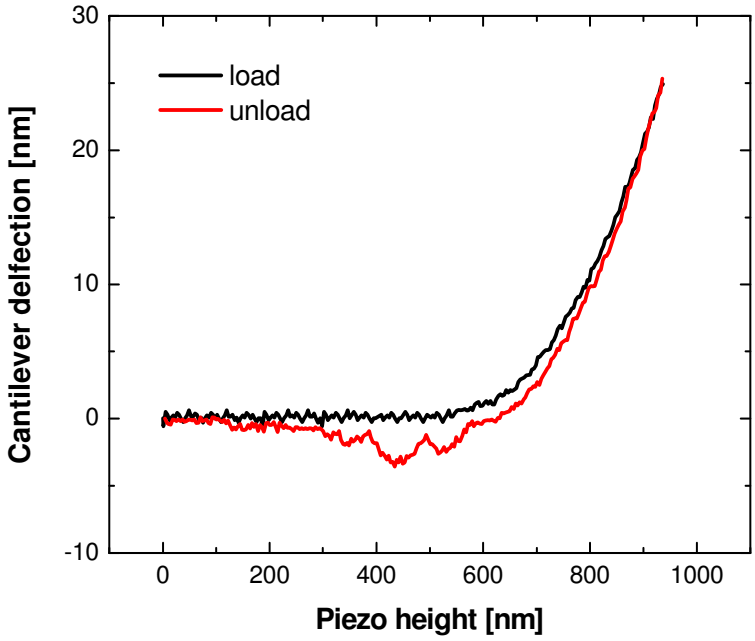

Figure 5.48: *Characteristic force-curve taken on a living cell in the area of its nucleus.*

The elastic properties of adherent osteoblast cells have been studied in a similar experimental manner as reported by Domke *et al.* [70]. The conical Hertz model has been fitted to the force-curves in various ranges of analysis. As an example, the fitted E and z_c for different ranges of cantilever deflection (i.e. in various ranges of loading force) are presented in Fig. 5.49.

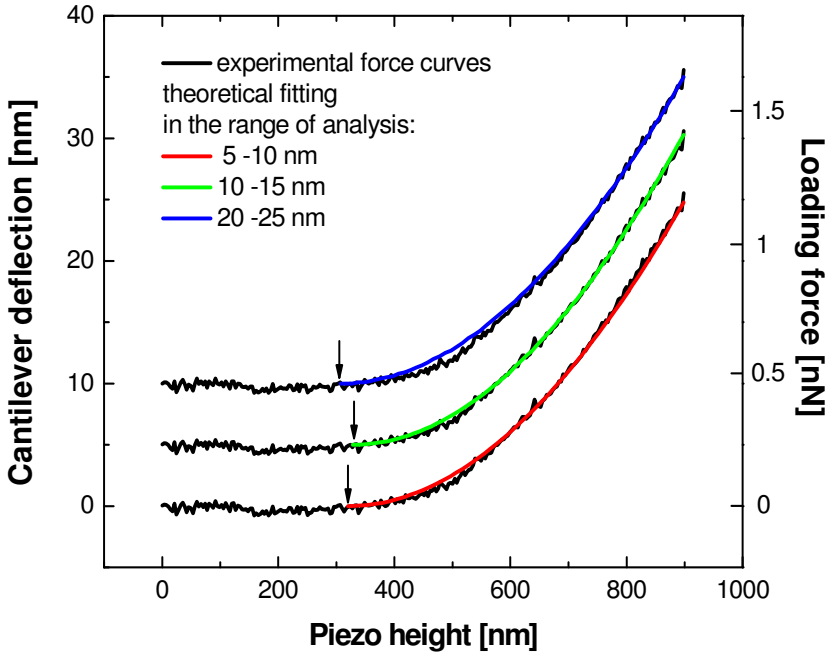

Figure 5.49: *Typical force-curve taken on a living cell and fitted in three different deflection ranges showing a good fit to the Hertz model in all applied force sections. For better visualization, the force-curve was plotted and shifted in y-direction by an offset of 5 nm each. The calculated contact point z_c is marked by an arrow.*

The theoretical Hertz curves match the data very well even outside the range of analysis. The contact points marked by arrows do not vary significantly. The calculated values are nearly independent of the range of the analysis, which is summarized in Table 5.5. This observation is consistent with the previously reported AFM studies of Radmacher *et al.* on human platelets [76]. They showed that the calculated E was independent of the range of the loading force used to fit the data for forces smaller than 0.6 nN.

Tab. 5.5: Summary of Young's modulus and contact points from the Hertz model fitting around various operating forces.

Cantilever deflection [nm] range of analysis	mean applied loading force [nN]	Young's modulus [kPa]
5 - 10	0.45	4.0
10 - 15	0.75	4.21
15 - 20	1.05	4.46
20 - 25	1.35	3.85
5 - 15	0.6	4.19

However, the situation changes if the applied loading force increases. Figure 5.50 shows a force-curve recorded on a living cell with a maximum loading force equal to 5 nN. There is a big influence of the chosen range of analysis on the calculated Young's modulus and on the contact point as calculated by the Hertz fit. The elastic modulus rises significantly when the loading force increases. This nonlinear elastic behavior of the sample at high loading forces can be explained by a large cell compression (tip feels underlying hard substrate) or by the strain/strain- hardening effect.

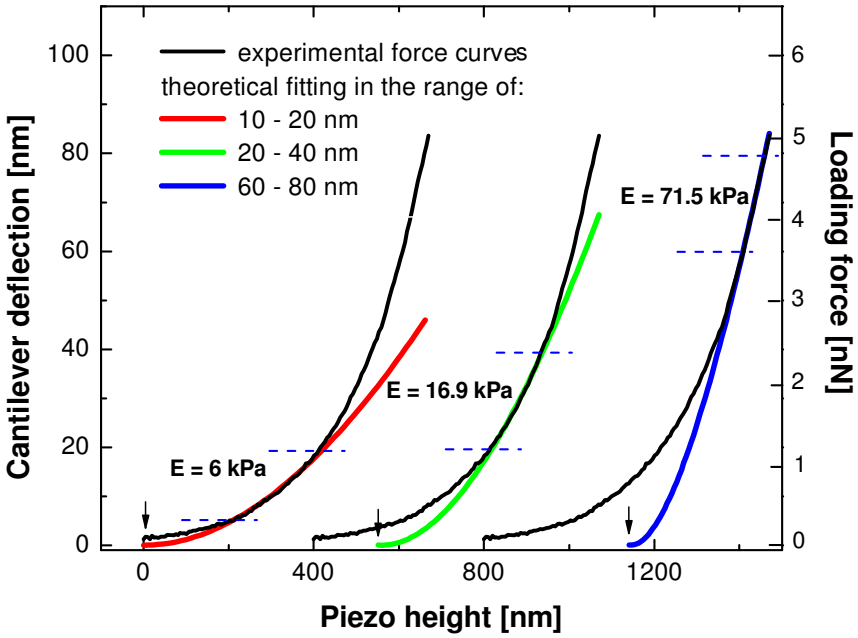

Figure 5.50: *Force-curve taken on the cell nucleus at a loading force equal to 5 nN. The experimental curve was shifted against each other in y-direction by offset of 400 nm. The calculated Young's modulus strongly depends on the chosen range of analysis. At high loading forces, the tip senses the underlying stiff substrates. Moreover, the calculated contact points (see arrows) depend significantly on the range of analysis.*

As indicated by some authors, an increase of the effective cell stiffness when high loading force is applied should be interpreted as a considerable compression of the cell, and therefore an increasing influence of the hard underlying substrate [77]. One the other hand, it is likely that a stress/strain-hardening effect is responsible for an increase of the cell stiffness rather that above explanation. It has been widely observed that cells of various types probed with different techniques exhibit a stress-hardening effect, such that cell stiffness increases progressively with increasingly applied mechanical load [78,79].

In these studies, all force-curves were analyzed at small cantilever deflection, corresponding to loading forces of 0.3 to 1.2 nN. In this range, the calculated Young's modulus was independent of the applied loading force and the elastic properties of osteoblasts plated on different substrates became comparable.

In force-curves, the deflection of the cantilever is proportional to the loading force and the deviation of the deflection from the slope obtained on the stiff substrate is the sample indentation [76]. Therefore, to calculate cell indentation, the measured deflection of the force-curve has to be subtracted from a curve recorded on a stiff substrate, where no or only negligible sample indentation takes place. Figure 5.51 illustrates characteristic force curves recorded on a living cell and on the hard substrate. The curves were shifted in such a way that the contact points overlap, showing the difference between these curves, which corresponds to cell indentation, δ. Based on this plot, δ can be computed easily, and was found to be around 400 nm for the loading force of 1 nN.

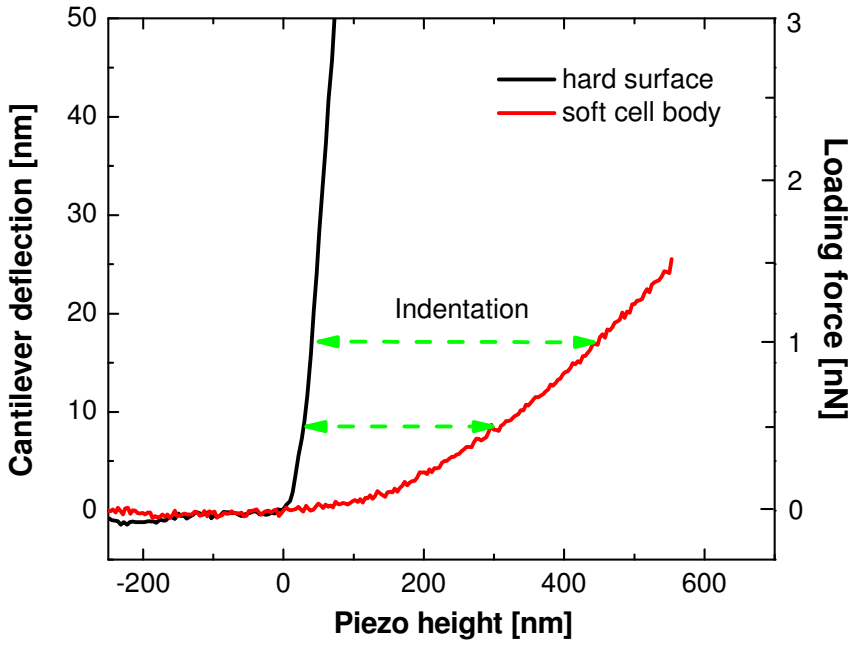

Figure 5.51: *Two typical force-curves recorded on a stiff substrate and a soft cell body. The difference between cantilever deflection gives the value of indentation occurring in the cell body.*

To compare the experimental data with the Hertz model, the indentation for this curve was calculated from the following equation [67]:

$$\delta = \sqrt{\frac{F\pi\tan(\alpha)(1-\nu^2)}{2E}} \qquad \textbf{(Eq. 5.19)}$$

The result is plotted on a double-logarithmic scale in Fig. 5.52. As can be seen, the prediction of the Hertz model with a Young's modulus of 5 kPa fits the experimental data very well.

Given the calculated δ and the measured height of the cells (h = 2.4(6) µm), the relative mean deformation of the cell can be estimated to be around 20 %.

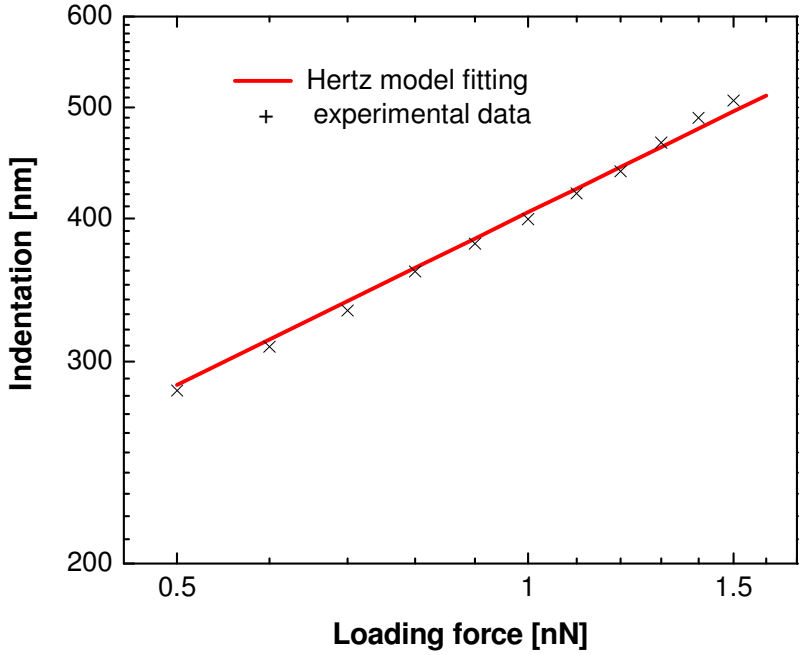

Figure 5.52: *The data were taken on the living cell. The calculated data fit the experiment over a large range of indentation for an elastic modulus of 5 kPa.*

The elasticity of human osteoblast cells has been determined by fitting the conical Hertz elastic model to different ranges of analysis that correspond to various deflection values and loading forces. The local elastic modulus was found to be independent when calculated at a range of small cantilever deflection, whereas an increased linear behavior was observed for high loading forces. This nonlinear elasticity at high values in the range of analysis has been explained by the fact of significant cell compression and, therefore, the influence of the stiff underlying substrate. The small loading force (~ 1.2 nN) caused cell indentation of up to 400 nm and the resulting Young's modulus was 3.71 kPa (for osteoblasts adhered to the glass surface).

5.5.1.1 Cellular structures contributing to the cell's mechanical behavior

As mentioned before, the mechanical properties of cells are determined in a complex way by the cell plasma membrane, the actin cortex, and the internal cytoskeleton. Taking into account the dimensions of these cellular structures as well as the cell indentation depth induced by the loading force range used in these AFM experiments, one can estimate the contribution of the cellular structures to the overall mechanical behavior of the cell. As calculated in the previous section, an applied loading force of 1.2 nN caused a cell indentation of ~ 400 nm, which far exceeds the thickness of the cell membrane (~ 10 nm). The next cellular structure probed by an AFM tip and located just below the plasma membrane is the actin cortex. This structure, consisting of highly concentrated actin filaments can extend up to about 0.5 -1 µm under the cell membrane [80].

Therefore, considering the indentation depths obtained in these studies, it is reasonable to believe that the AFM probed the mechanical properties of the actin filaments. This hypothesis is in agreement with Stamenovic *et al.* [81], who showed that, in general, actin filaments provide the cell's elastic response at relatively low strain (cell deformation < 20 %), while intermediate filaments provide the cell's mechanical strength at higher strains (> 20 %).

5.5.1.2 Comparison of Young's modulus of living and fixed osteoblast cells

As has been shown in section 5.4.2, the obtainable lateral resolution of an AFM depends on the cell's elastic modulus and can be estimated with the help of the contact area between tip and sample. Taking into account that the elastic modulus of living cells lies below 100 kPa, the obtained contact area at the softest part of the cell is larger than 100 nm. To improve the resolution, glutaraldehyde cell fixation can be applied [65]. In this fixation process, proteins are covalently cross-linked, which results in a higher stiffness of the cell.

In this section, the low-resolution images of living cells are explained by the differences in stiffness of living and glutaraldehyde-fixed HOB cells, by measuring the local elastic properties.

The figures presented below, compare force-curves (right) taken on a living and on a fixed cell. The obtained force-curves were recorded during scanning along one line over the cell's body at five different places (indicated in the AFM images, left). The force-curves where then placed on top of each other to show all the curves within one graph. Figure 5.53 shows clearly that the curves recorded on the living cell are curved with a small slope characteristic of soft materials. The curves recorded on the fixed cell (Fig. 5.54), in contrast, exhibit a steep slope, similar to the curves taken on the hard substrate (no. 1 on both plots). This similarity indicates that the stiffness of the cell has increased significantly.

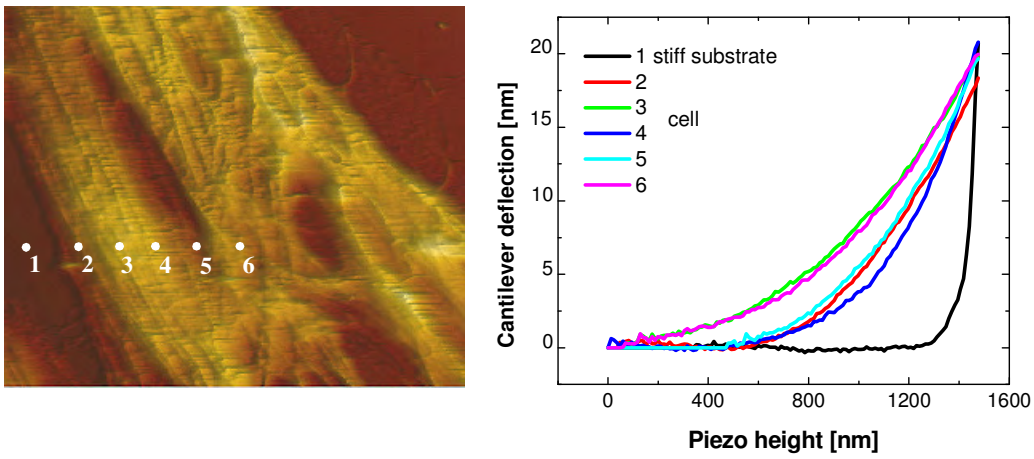

Figure 5.53: *Force-curves taken on a living cell in five different places indicates in the AFM image. Obtained force-curves show a small slope.*

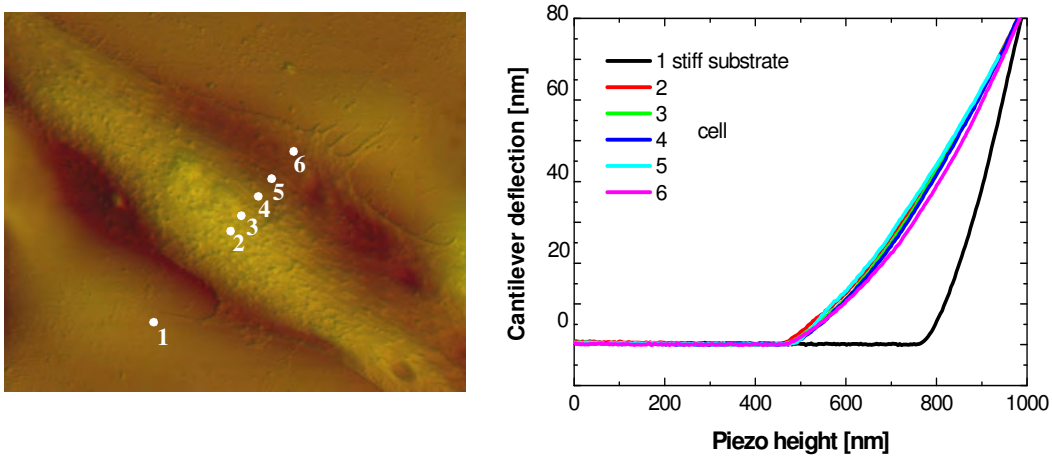

Figure 5.54: *Force-curves taken on a fixed cell in five different places indicates in the AFM image. Recorded force-curves show a small slope, and they appear similar to the one taken on a hard substrate, which is an indication of the cell's stiffness.*

The calculated elastic modulus from the fitting of the conical Hertz model to the force curve recorded in the central region of the fixed cell is shown in Fig. 5.55. In contrast to the living cell, the theoretical curve matches the data very well over the whole range of analysis. The computed elastic modulus demonstrates that glutaraldehyde fixation has drastically changed the cell's elastic properties through increasing its stiffness by several orders of magnitude: from around 5 kPa to more than 100 kPa (mean E = 139.2(16.9) kPa). Moreover, the computed Young's modulus had comparable values while indenting different areas on the cell, which indicates that, in contrast to the living cell, the stiffness of the fixed cell is constant irrespective of its inner structure.

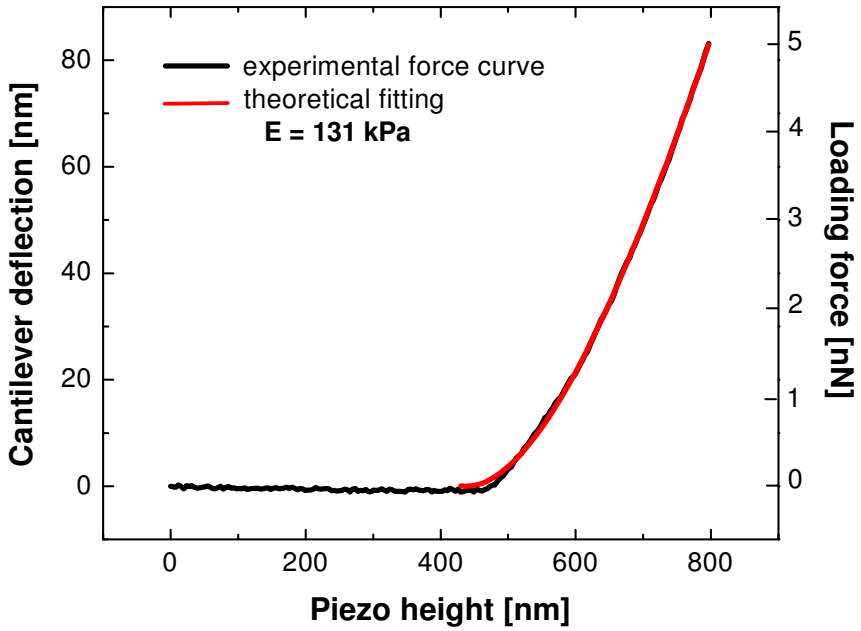

Figure 5.55: *The Hertz model applied to the experimental force-curve No. 4 (see Fig. 1.39B), which was taken on a fixed cell. The theoretical curve, superimposed on top of the experimental one, fits the experimental curve very well over the whole range of analysis.*

5.5.2 Substrate-dependent elasticity of living osteoblast-like cells

Up to now, it has been shown that AFM can successfully be used to investigate nanomechanical properties of living osteoblasts and that resulting conclusions may be extended to the cytoskeletal structures inside the cell. Taking into account the important role of the cytoskeleton in cell elasticity and considering the fact that its architecture may be influenced by the substrate the cell is adhered to, one can assume that mechanical properties of cells growing on different substrates may undergo alterations. Aiming to verify this statement, the elasticity of the osteoblast cells adhered to various substrates has been studied.

Characteristic topographies of samples used in these AFM experiments are shown in Fig. 5.56. To rule out the possibility that the cytomechanical changes observed were due to the differences in substrate chemistry, and for better understanding of the role that matrix topography plays in cell adhesion, both MWNT-based matrices were assembled from non-covalently modified nanotubes (MWNT-PAH), which assured similar surface chemistry. Another important physical factor, which may also elicit changes in cell elasticity, and that should also be taken into account while analyzing AFM data, is a stiffness of the substrates. Several studies have shown that cells can probe and respond to mechanical properties of the substrate [82,83]. For example, Pelham *et al*. reported changes in cell adhesion structures and motile behavior caused by differences in substrate flexibility [84]. Given that the CNT-based matrices used in this study were composed of the same nanotubes (MWNT-PAH) and polyelectrolytes (PSS, PAH), and that the LbL technique assured mainly parallel orientation of the CNTs to the substrate surface, one can assume that both, matrices with cavity-like and random topography, are characterized by the same substrate stiffness. Taken together, the physical effect such as surface chemistry and substrate stiffness could be separated from topographical features and the nanomechanical results for carbon nanotube matrices could be related and compared.
On the basis of the results from immunofluorescent staining (section 5.3.2), it also became interesting to study the mechanical properties of cells adhered to periodic VACNTs. However, due to difficulties in the imaging of cells attached to the tips of CNTs, osteoblast adhesion was studied on a similar honeycomb pattern created from gold quasi-triangles (Fig. 5.56 C).

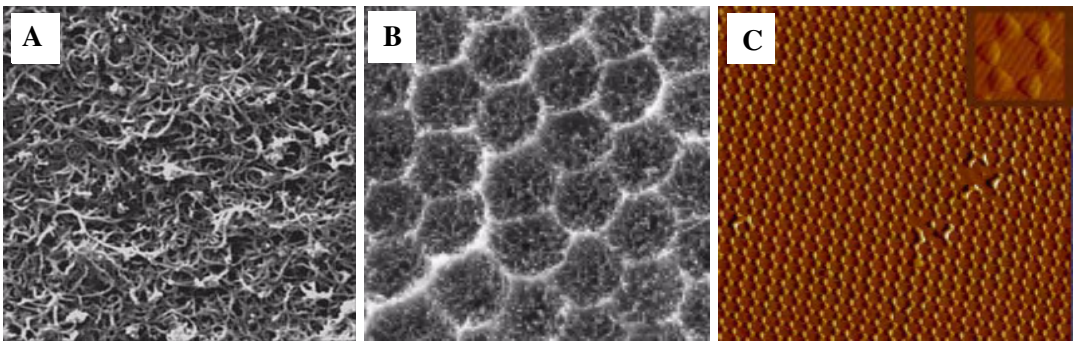

Figure 5.56: *Surface topography of the substrates used for studying cytomechanical properties of adhered cells. SEM images of CNT-based LbL films with randomly-distributed nanotubes (A) and ordered in a cavity-like structure (B). AFM deflection image of quasi-triangular gold clusters forming a honeycomb structure (C).*

Mechanical measurements were conducted in the same experimental manner as described in section 5.5.1. In particular, the force-curves were analyzed in those force ranges that result in shallow indentations of the cell (~ 400 nm). Figure 5.57 shows cell elasticity measurements (Young's modulus, *E*), collected from 100 force-curves recorded on 10 cells from each sample (each cell was probed 10 times in the area of the nucleus).

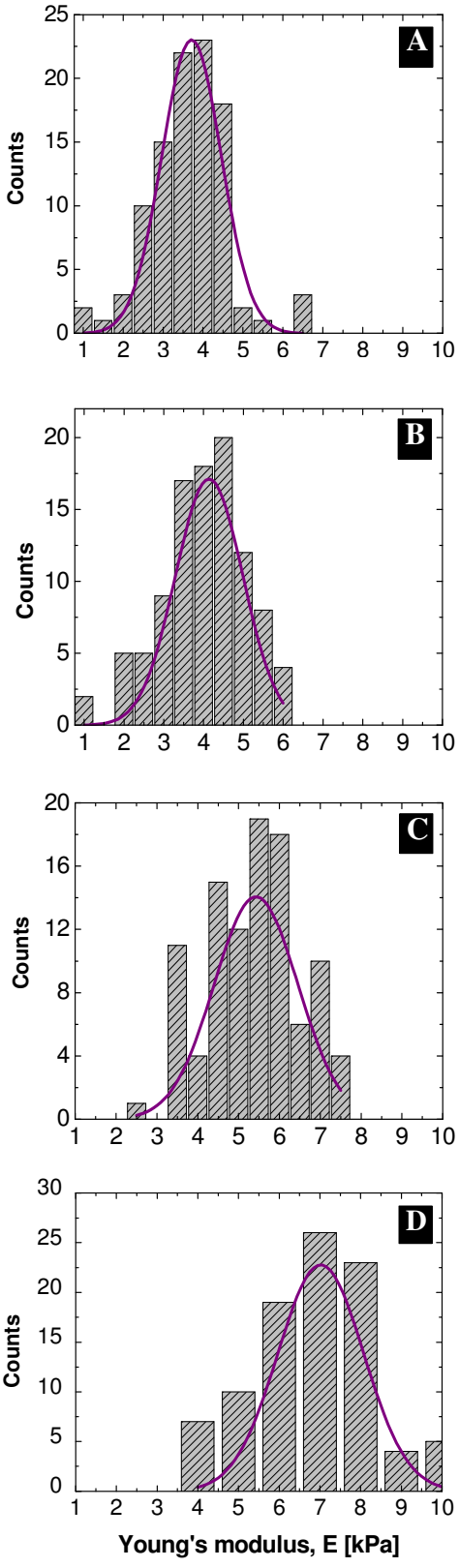

Figure 5.57: *Histograms of mean value and distribution of Young's modulus obtained for cells adhered to glass (A), CNT LbL film (B), CNT based cavity-like structure (C), and hexagonally-ordered gold quasi-triangles (D).*

The mean Young's modulus values received by fitting a Gaussian distribution to the above histograms are presented in table 5.6. The obtained results clearly demonstrate that the mean Young's modulus is altered by adhesion to different substrates. In general, the osteoblast cells plated on glass were found to have the lowest cell stiffness (3.71 ± 1.48 kPa), whereas the cells adhered to the CNT-based substrates expressed an increased average Young's modulus. This expected difference may arise from the surface roughness and partially from differences in surface chemistry. It is known that surface roughness increases protein adsorption and hence cell adhesion. This result is in agreement with observations made by Domke *et al*. [70] who showed that cell stiffness rises with increasing surface roughness of the respective substrates. Interestingly, those cells adhered to the cavity-like structures exhibited a higher stiffness (E = 5.43 ± 2.05 kPa) than osteoblasts plated on randomly-distributed CNTs (E = 4.14 ± 1.69 kPa). Since the substrates are characterized by the same stiffness and surface chemistry, the obtained results point out that a regular topography may have a greater influence on osteoblast cell adhesion than an irregular one.

Tab. 5.6: Mean Young's modulus calculated for osteoblast cells cultured on different substrates. Errors correspond to the full width at half maximum of the Gaussian peak.

SUBSTRATE TYPE	F [nN]	E [kPa]
Glass	1.2	3.71(1.48)
CNT Matrix - Cavity-like topography		5.43(2.05)
CNT Film - Nanotubes randomly distributed		4.14(1.69)
Honeycomb structure		7.02(2.11)

Elastic measurements for osteoblast cells plated on a hexagonally-ordered quasi-triangular structure seem to confirm this assumption. Substrates with highly regular topography were found to significantly enhance cell adhesion, resulting in the highest cell stiffness (7.02 ± 2.11 kPa) compared to the rest of the substrates used in these studies. It should be mentioned that besides surface topography, high cell stiffness, observed for cells attached to the honeycomb structure, may also originate from the biocompatible nature of the gold quasi-triangles, and the difference in the stiffness of the substrate.

Considerable differences between E values for cells adhered to glass and quasi-triangle substrates can be explained by observations from immunofluorescent staining (Fig. 5.58) of focal adhesion of vinculin protein within the cells. According to Goldman *et al.* [85], vinculin promotes cell adhesion and spreading by stabilizing focal adhesions and transferring mechanical stress that drives cytoskeletal remodeling, thereby affecting the elastic properties of the cell. Since osteoblast cells adhered to gold triangles exhibit very prominent focal adhesions, which contain well-

developed vinculin plaque-like clusters (Fig. 5.58 A), it is reasonable to assume that the high stiffness of these cells is directly correlated to a highly expressed vinculin protein. Consequently, the decrease in focal adhesion formation within osteoblasts plated on a glass substrate is reflected by a low stiffness of these cells (Fig. 5.58 B).

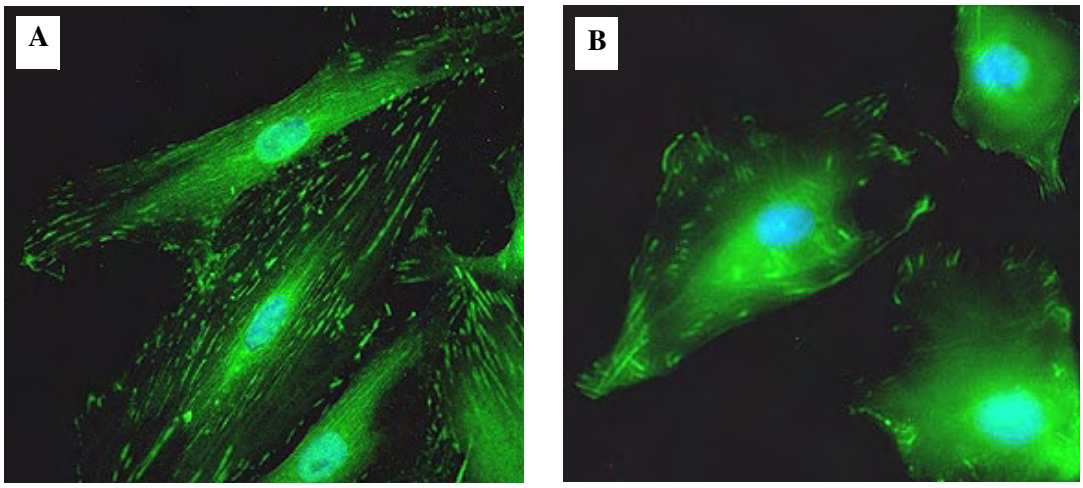

Figure 5.58: *Typical vinculin expression of HOB cells adhered to hexagonally-structured gold triangles (A) and glass substrates (B). Cells adhered to the ordered structure exhibit well developed vinculin clusters visible throughout the entire cell body, while the osteoblasts attached to glass show focal contacts mostly limited to their periphery.*

The observed variations in the mean Young's modulus of osteoblast cells adhered to different substrates are most likely due to cytoskeleton organization. This claim may be additionally supported by AFM nanomechanical analysis of cancer cells. Various authors have shown that quantitatively determined differences in the elastic properties between normal and cancerous cells are attributed to possible changes in cytoskeleton organization due to oncogenic transformation [80]. Therefore, the obtained cell stiffness of cancer cells was more than 70 % lower than for healthy cells [86]. Another quantitative as well as qualitative study showed the reduction of chicken cardiocyte cell elasticity after degradation of the actin filament network caused by a cytoskeleton-disrupting drug, cytochalasin B [87].

In general, the mean Young's modulus values obtained in these studies fit the range of the reported data of cell stiffness measured by AFM. Table 5.7 presents E values calculated with the conical Hertz model. Any discrepancies in these values may arise from the chosen range of force-curve analysis as well as from the growth conditions, i.e. the type of substrate and adhesive factors used for cell growth.

Tab. 5.7: Values for the mean elastic modulus taken from AFM studies on different cell types. Young's modulus was calculated using the conical Hertz model. F and δ are maximum loading force and cell indentation, respectively.

CELL TYPE	**F [nN]**	δ[μm]	**E[kPa]**	**REFERENCE**
Osteoblasts (HOB-C)	1.2	0.42	5.43	our data
Osteoblasts (SaOS2)	0.88	0.3	9	[70]
Fibroblasts (NIH3T3)	0.3	0.2	4	[88]
platelets	0.45	0.15	6	[76]
epithelial (CV-1)	0.05	0.01	400	[89]
Osteoblasts (MC3T3-E1)	3	0.5	2	[71]
Cardiocytes	6	0.55	30	[90]
mesothelial	1	0.4	1.86	[86]

Results presented in this paragraph have shown that AFM has a great potential for testing the biocompatibility of various materials by investigating the adhesion behavior of cells *in vitro*. The performed nanomechanical measurements indicate that CNT-based matrices with a unique cavity-like topography provide a better cell adhesion compared to the glass substrates and randomly-distributed carbon nanotubes.

References

[1] A. Kosiorek, W. Kandulski, P. Chudzinski, K. Kempa, M. Giersig, "Shadow nanosphere lithography: symulation and experiment". *Nano Lett*. **4**, 1359 (2004)

[2] M.S. Schmidt, T. Nielsen, D.N. Madsen, A. Kristensen, P. Boggild, "Nano-scale silicon structures by using carbon nanotubes as reactive ion masks". *Nanotechnology* **16**, 750 (2005)

[3] T.A. El-Aguizy, J.H. Jeong, Y.B. Teon, W.Z. Li, Z.F. Ren, S.G. Kim, "Transplanting carbon nanotubes". *Appl. Phys. Lett*. **85**, 5995 (2004)

[4] H. Bubert, S. Haiber, W. Brandl, G. Marginean, M. Heintze, V. Bruser, "Characterization of the uppermost layer of plasma treated carbon nanotubes". *Diamond and Related Materials* **12**, 811 (2003)

[5] C.U. Pittman, G-R. He, B. Wu, S.D. Gardner, "Chemical modification of carbon fiber surfaces by nitric and acid oxidation followed by reaction with tatraethylenepentamine". *Carbon* **35**, 317 (1997)

[6] I. Firkowska, M. Olek, N. Pazos-Perez, J. Rojas-Chapana, M. Giersig, "Highly ordered MWNT-based matrixes: topography at the nanoscale conceived for tissue engineering". *Langmuir* **22**, 5427 (2006)

[7] Y. Wang, X. Wang, J. Rybczynski, D.Z. Wang, K. Kempa, Z.F. Ren, "Triangular lattice of carbon nanotube arrays for negative index of refraction and subwavelength lensing effect". *Appl. Phys. Lett.* **86** (2005)

[8] A.A. Mamedov, N.A. Kotov, M. Prato, D.M. Guldi, J.P. Wicksted, A. Hirsch, "Molecular design of strong single-wall carbon nanotube/polyelectrolyte multilayer composites". *Nature Materials* **1**, 190 (2002)

[9] K.J. Loch, J.P. Lynch, N.A. Kotov, "Conformable single-walled carbon nanotube thin film strain sensors for structural monitoring". *Proceedings of the 5th International Workshop on Structural Health Monitoring, standford CA, USA, Sept. 12-14*, (2005)

[10] M.K. Gheith, V.A. Sinani, J.P. Wicksted, R.L. Matts, N.A. Kotov, "Single-walled carbon nanotube polyelectrolyte multilayers and freestanding films as a biocompatible platform for neuroprosthetic implants". *Adv. Mater*. **17**, 2663 (2005)

[11] M. Olek, K. Kempa, S. Jurga, M. Giersig, "Nanomechanical properties of silica-coated multiwall carbon nanotubes-poly(methyl methacrylate) composite". *Langmuir* **21**, 3146 (2005)

[12] P.V. Pavoor, A. Bellare, A. Strom, D.H. Yang, R.E. Cohen, "Mechanical characterization of polyelectrolyte multilayers using quasi-static nanoindentation". *Macromolecules* **37**, 4865 (2004)

[13] M. Olek, J. Ostrander, S. Jurga, H. Mohwald, N. Kotov, K. Kempa, M. Giersig, "Layer-by-Layer assembly composites from multi wall carbon nanotubes with different morphologies". *Nano. Lett.* **4**, 1889 (2004).

[14] G. Wei, J.A. Barnard, "Nanotrobological studies of thin CrNx, CrO_x and CN_x overcoats for magnetic recording applications". *J. Appl. Phys*. **91**, 7565 (2002).

[15] M.J. Dalby, M.O. Riehle, D.S. Sutherland, H. Agheli, and A.S.G. Curtis, "Fibroblast response to a controlled nanoenviroment produced by colloidal lithography". *J. Biomed. Mat. Res*. **69**A, 314 (2004)

[16] R.G. Flemming, C.J. Murphy, G.A. Abrams, S.L. Goodman, and P.F. Nealey, "Effects of synthetic micro- and nano-structured surfaces on cell behaviour". *Biomaterial*s **20**, 573 (1999)

[17] M.J. Dalby, M.O. Riehle, S.J. Yarwood, C.D.W. Wilkinson, and A.S.G. Curtis, "Nucleus alignment and cell signalling in fibroblast: Response to a micro-graved topography". *Experimental Cell Research* **284**, 274 (2003)

[18] H. Zreiqat, M.S. Valenzuela, B.B. Nissan, R. Roest, Ch. Knabe, R.J. Radlanski, H. Renz, P.J. Evans, "The effect of surface chemistry modification of titanium alloy on signalling pathways in human osteoblasts". *Biomaterials* **25**, 7579 (2005)

[19] D. Cui, F. Tian, C.S. Ozkan, M. Wang, W. Gao, "Effect of single wall carbon nanotubes on human HEK293 cells". *Toxicology Lett*. **155**, 73 (2005)

[20] S.K. Manna**,** S. Sarkar, J. Barr, K. Wise, E.V. Barrera, O. Jejelowo, A.C. Rice-Ficht, G.T. Ramesh, "Single-walled carbon nanotubes induces oxidative stress and activates nuclear transcription factor-κB in human kerationcytes". Nano Lett. **5**, 1676 (2005)

[21] C-W. Lam, J.T. James, R. McCluskey, R.L. Hunter, "Pulmonary toxicity of single-wall carbon nanotubes in mice 7 and 9 days after intratracheal instillation". *Toxicological Sciences*, **77**, 126 (2004)

[22] L.P. Zanello, B. Zhao, H. Hu, R.C. Haddon, "Bone cell proliferation on carbon nanotubes". *Nano Lett.* **6,** 562 (2006)

[23] K. Anselme, "Osteoblast adhesion on biomaterials". *Biomat*. **21**, 667 (2000)

[24] R.A. MacDonald, B.F., Laurenzi, G. Viswanathan, P.M. Ajayan, J.P. Stegemann, "Collagen-carbon nanotube composite materals as scaffolds in tissue engineering". *J. Biomed. Mater. Res. A* **74**, 489 (2005)

[25] K. Anselme, M. Bigerelle, B. Noel, E. Dufrsne, D. Judas, A. Iost, P. Hardouin, "Qualitative and quantitative study of human osteoblast adhesion on materials with various surface roughnesses". J. Biomed. Mat. Res. Part A, 49, 155 (1999)

[26] R.L. Price, K.M. Haberstroh, T.J. Webster, "Improved osteoblast viability in the presence of smaller nanometer dimensioned carbon fibres". *Nanotechnology* **15**, 892 (2004)

[27] H. Hu, Y. Ni, V. Montana, R.C. Haddon, V. Parpura, "Chemicaly functionalized carbon nanotubes as substrate for neuronal growth". *Nano Lett*. **4**, 507 (2004)

[28] Z. Schwartz, S.H. Lohmann, J. Oefinger, L.F. Bonewald, D.D. Dean, B.D. Boyan, "Implant surface characteristic modulate differential behaviour of cells in the osteoblast lineage". *Adv. Dent. Res* **13**, 38 (1999)

[29] F.B. Bagambisa, H.F. Kappert, W. Schilli, "Cellular and molecular biological events at the implant interface". *J. Craniomaxilloface Surg*. **22**, 12 (1994)

[30] M.P. Mattson, R.C. Haddon, A.M. Rao, "Molecular functionalization of carbon nanotubes and use as substrate for neuronal growth". *J. Mol. Neurosci*. **14**, 175 (2000)

[31] S. Sirivisoot, C. Yao, X. Xiao, B.W. Sheldon, T.J. Webster, "Greater osteoblast functions on multiwalled carbon nanotubes grown from anodized nanotubular titanium for orthopedic application". *Nanotechnology* **18**, 365102 (2007)

[32] K. Webb, V. Hladly, P.A. Tresco, "Relationships among cell attachment, spreading, cytoskeletal organization, and migration rate for anchor-dependent cells on model surfaces". *J. Biomed. Mater. Res*. **49**, 362 (2000)

[33] B.D. Boyan, T.W. Hummert, D.D. Dean, Z. Schwartz, "Role of material surface in regulating bone and cartilage cell resopnse". *Biomaterials* **17**, 137 (1996)

[34] H. Liu, T.J. Webster, "Nanomedicine for implants: A review of studies and necessary experimental tools". *Biomaterials* **28**, 254 (2007)

[35] D.S. Salloum, J.B Schlenoff, "Protein adsorption on polyelectrolyte multilayers" *Biomacromolecules* **5**, 1089 (2004)

[36] P. Swanand, A. Sandberg, E. Heckert, W. Self, and S. Seal, "Protein adsorption and cellular uptake of cerium oxide nanoparticles as a function of zeta potential". *Biomaterials* **28**, 4600 (2007).

[37] H. Ohshima, K. Furusawa, "Electrical Phenomena at Interfaces, Second Edition: Fundamentals, Measurements and Applications". *Surfactant Science* **76**, CRC Press (1998)

[38] Y. Liu, L. Gao, "A study of the electrical properties of carbon nanotube-$NiFe_2O_4$ composites: Effect on the surface treatment of the carbon nanotubes". *Carbon* **43**, 47 (2005)

[39] C.A.. Haynes, W. Norde, "Globular proteins at solid-liguid interfaces". C*olloids Surf. B: Biointerfaces* **2**, 517 (1994)

[40] M.M. Bradford, "A rapid and sensitive method for the quantification of microgram quantities of proteins utilising the principle of protein-dye-binding". *Anal. Biochem.* **72**, 248 (1976)

[41] D.S. Salloum, J.B. Schlenoff, "Protein adsorption modalities on polyelectrolyte multilayers". *Biomacromolecules* **5**, 1089 (2004)

[42] M. Muller, T. Rieser, P.L. Dubin, K. Lunkwitz, " Selective interaction between proteins and the outermost surface of polyelectrolyte multilayers: influence of the polyanion type, pH and salt". *Macromolecular Rapid Communicationn* **22**, 390 (2001)

[43] P. Schwinte, V. Ball, B. Szalontai, Y. Haikel, J.-C. Voegel, and P. Schaal, "Secondary Structure of Proteins Adsorbed onto or Embedded in Polyelectrolyte Multilayers". *Biomacromolecules* **3**, 1135 (2002)

[44] M.C. Siebers, P.J. Brugge, X.F. Walboomers, J.A. Jansen "Integrins as linker proteins between osteoblasts and bone replacing materials". *Biomaterials* **26**, 137 (2005)

[45] B. Zhao, H. Hu, S.K. Mandal, R.C. Haddon, "A bone mimic based on the self-assembly of hydroxyapatite on chemically functionalized single-walled carbon nanotubes". *Chem. Mater.* **17**, 3235 (2005)

[46] C. Andres, V. Sinani, D. Lee, Y. Gun'ko, N. Kotov, "Anisotropic calcium phosphate nanoparticles coated with 2-carboxyethylphosphonic acid". *J. Mater. Chem.* **16**, 3964 (2006)

[47] P.V. Phan, M. Grzanna, J. Chu, A. Polotsky, A. El-Ghannam, D. Van Heerden, D.S. Hungerford, C.G. Frondoza, "The effect of silicon-containing calcium-phosphate particles on human osteoblast in vitro". *J. Biomed. Mat. Res. Part A,* **67**, 1001 (2003)

[48] T.J. Webster, C. Ergun, R.H. Doremus, R.W. Siegel, R. Bizios, "Enhanced functions of osteoblasts on nanophase ceramics". *Biomaterials* **21**, 1803 (2000)

[49] J.L. Charest, L.E. Bryant, A.J. Garcia, W.P. King, "Hot embossing for micropatterned cell substrates". *Biomaterials* **19,** 4767 (2004)

[50] K. Anselme, M. Bigerelle, B. Noel, A. Lost, P. Hardouin, "Effect of grooved titanium substratum on human osteoblastic cell growth". *J. Biomed. Mat. Res. Part A*, **60**, 529 (2002)

[51] R.G. Flemming, C.J. Murphy, G.A. Abrams, S.L. Goodman, P.F. Nealey, "Effects of synthetic micro- and nano-structured surfaces on cell behavior". *Biomaterials* **20**, 573 (1999).

[52] Y.A. Rovensky, A.D. Bershadsky, E.I. Givargizov, L.N. Obolenskaya, J.M. Vasilev, "Spreading of mouse fibroblast on the sustrate with the multiple spikes". *Exp. Cell. Res.* **197**, 107 (1997)

[53] A.F. von Recum, T.G. van Kooten, "The influence of micrography on cellular response and the implications for silicone implants". *J. Biomat. Sci. Poly*. Ed. **7**, 181 (1995)

[54] T.G. van Kooten, A.F. von Recum, "Cell adhesion to textured silicone surfaces: The influence of time of adhesion and texture on focal contact and fibronectin fibril formation". *Tissue. Eng*. **5**, 223 (1999)

[55] S. Giannona, I. Firkowska, J. Rojas-Chapana, M. Giersig, "Vertically aligned carbon nanotubes as cytocompatible material for enhanced adhesion and proliferation of osteoblast-like cells". *J. Nanosci. and Nanotechnol*. **7**, 1679 (2007)

[56] J.L. Tan, J. Tien, D.M. Pirone, D.S. Gray, K. Bhadriraju, C. Chen, "Cells lying on a bed of microneedles: An approach to isolate mechanical force". *Proc. Natl. Acad. Sci.* **100**, 1484 (2003)

[57] X. Zhang, S. Prasad, S., Niyogi, A. Morgan, M. Ozkan, C.S. Ozkan, "Guided neurite growth on patterned carbon nanotubes". *Sensors and Actuators B*, **106**, 843 (2005)

[58] E. Zamir, B. Geiger, Molecular complexity and dynamics of cell-matrix adhesions". *J. Cell Sci.* **114**, 3583 (2001)

[59] Y.G. Kuznetsov, A.J. Malkin, A. McPherson, "Atomic force microscopy studies of living cells: visualization of motility, division, aggregation, transformation, and apoptosis". *J. Struct. Biol.* **120**, 180 (1997)

[60] Y. Shen, J.L. Sun, A. Zhang, J. Hu, L.X. Xu, "Shape recovering of live endothelial cell under atomic force microscopy imaging". *Engineering in Medicine and Biology Society* **1**, 2603 (2004)

[61] A.Simon, T.Cohen-Bouhacina, M.C. Porte, J.P. Aime, J. Amedee, R. Bareille, and C. Baquey, "Characterization of dynamic cellular adhesion of osteoblasts using atomic force microscopy". *Cytometry Part A* **54**, 36 (2003)

[62] H.A. McNally, R.B. Borgens, "Three-dimensional imaging of living and dying neurons with atomic force microscopy". *J. Neurocytology* **33**, 251 (2004)

[63] D.S. Sakaguchi, "The developoment of retinal ganglion cells deprived of their targets". *Dev. Biol.* **134**, 103 (1989)

[64] E. Henderson, P.G. Haydon, D.S. Sakaguchi, "Actin filament dynamics in living gial cells imaged by atomic force microscopy". *Science* **257**, 1944 (1992)

[65] F. Braet, C. Rotsch, E. Wisse, M. Radmacher, "Comparison of fixed and living liver endothelial cells by atomic force microscopy". *Appl. Phys. A*, **66**, 575 (1998)

[66] P.G. Haydon, R. Lartius, V. Parpura, S.P. Merchese-Ragona, "Membrane deformation of living glial cells using atomic force microscopy". *J. Microscopy* **182**, 114 (1996)

[67] I.N. Sneddon, "The relaxation between load and penetration in the axis symmetric Boussinesq problem for a punch of arbitrary profile". *Int. J. Engng. Sci*. **3**, 47 (1965)

[68] K.L. Johnson "Contact Mechanics". Cambridge University Press (1985)

[69] A. Krause, E.A. Cowles, G. Gronowicz, "Integrin-mediated signaling in osteoblasts on titanium implant materials". *J. Biomed. Mat. Res*. **52**, 738 (2000).

[70] J. Domke, S. Dannohl, W.J. Parak, O. Muller, W.A. Aicher, M. Radmacher, "Substrate dependent differences in morphology and elasticity of living osteoblast investigated by atomic force microscopy". *Colloids Surf. B. Biointerfaces*. **19**, 367 (2000)

[71] E. Takai, K.D. Costa, A. Shaheen, C.T. Hung, X.E. Guo, "Osteoblast elastic modulus measured by atomis force microscopy is substrates dependent". *Ann. Biomed. Engineer*. **33**, 963 (2005)

[72] H.W. Wung, V.T. Moy, "Mechanical properties of 1929 cell measured by atomic force microscopy: Effects of anticytoskeletal drugs and membrane crosslinking". *Scanning* **20**, 389 (1998)

[73] O. Thoumine, O. Cardos, J.J. Meister, "Changes in the mechanical properties of fibroblasts during spreading: a micromanipulation study". *Eur. Biophys. J*. **28**, 222 (1999)

[74] A.R. Bausch, W. Moller, E. Sackmann, "Measurement of local viscoesticity and forces in living cells by magnetic tweezers". *Biophys. J*. **76**, 573 (1999)

[75] S.R. Heidemann, S. Kaech, R.E. Bauxbaum, A. Matus, "Direct observations of the machanical behaviors of the cytoskeleton in living fibroblasts". *J. Cell. Biol.* **145**, 109 (1999)

[76] M. Radmacher, M. Fritz, C.M. Kacher, J.P. Cleveland, P.K. Hansma, "Measuring the viscoelastic properties of human platelets with the atomic force microscopy". *J. Biophy*. **70**, 556 (1996)

[77] M. Radmacher, "Measuring the elastic properties of biological samples with the AFM". *IEE. Eng. Med. Biol.* **16**, 47 (1997)

[78] M.R.K. Mofrad, R.D. Kamm, "Cytoskeletal mechanics. Models and Measurements" *Cambridge University Press* NY (2006)

[79] C. Zhu, G. Bao, N. Wang, "Cell mechanics: mechanical response, cell adhesion, and molecular deformation. *Annu. Rev. Biomed. Eng*. **2**, 189 (2000)

[80] M. Lekka, P. Laidler, D. Gill, J. Lekki, Z. Stachura, A.Z. Hrynkiewicz, "Elasticity of normal and cancerous human bladder cell studied by scanning force microscopy". *Eur. Biophys. J*. **28**, 312 (1999)

[81] D. Stamenovic, N. Wang, "Engineering approaches to cytoskeletal mechanics". *J. Appl. Physiol.* **89**, 2085 (2000)

[82] D.E. Disher, P. Janmey, Y-L. Wang, "Tissue cells feel and respond to the stiffness of their substrate", *Science* **310**, 1139 (2005)

[83] A. Engler, L. Bacakova, C, Newman, A. Hategan, M. Griffin, D.E. Discher, "Substrate compliance versus ligand density in cell on gel responses". *J. Biophys.* **86**, 617 (2004)

[84] R.J. Pelham, Y-L. Wang, "Cell locomotion and focal adhesions are regulated by substrate flexibility". *Proc. Natl. Acad. Sci. USA* **94**, 133661 (1997)

[85] W.H. Goldmann, R. Galneder, M. Ludwig, W. Xu, E.D. Adamson, N. Wang, R.M. Ezzell, "Differences in Elasticity of vinculin-deficient F9 cells measured by magnetometry and atomic force microscopy". *Exp. Cell. Research* **239**, 235 (1998).

[86] S.E. Cross, Y-S. Jin, J. Rao, J.K. Gimzewski, "Nanomechanical analysis of cells from cancer patients". *Nature* **2**, 780 (2007)

[87] E.A-Hassan, W.F. Heinz, M.D. Antonik, N.P. D'Costa, S. Nageswaran, C-A. Schoenenberger, J.H. Hoh, "Relative microelastic mapping of living cells by atomic force microscopy". *Biophys. J*. **74**, 1564 (1998)

[88] H. Haga, S. Sasaki, K. Kawabata, E. Ito, T. Ushki, T. Sambongi, "Elasticity mapping of living fibroblasts by AFM and immunofluorescence observation of the cytoskeleton". *Ultramicroscopy* **82**, 253 (2000)

[89] C. Le Grimellec, E. Lesniewska, M-C. Giocindi, E. Finot, V. Vie, "Imaging of the surface of living cells by low-force contact-mode atomic force microscopy". *Biophys. J*. **75**, 695 (1998)

[90] U.G. Hofmann, Ch. Rotsch, W.J. Parak, M. Radmacher, "Investigating the cytoskeleton of chicken cardiocytes with the atomic force microscopy". *J. Struct. Biol.* **119**, 84 (1997)

Chapter 6
Summary

In this thesis, carbon nanotubes were used to create model systems, to explore the cellular response to carbon nanotube-based materials. The nanostructured constructs were used to investigate the influence of nanoscaled dimensions on human osteoblast-like cell behavior, with particular interest in the effects of local topography and surface chemistry. It is shown that cells sense and react to the MWNTs matrices by responding with excellent adhesion, proliferation and metabolic activity. The results presented here indicate that carbon nanotubes can mimic the nanofeatures of the native extracellular matrix and therefore, have an immense potential for application in tissue engineering.

The realization of the potential of carbon nanotubes in bioapplications requires their chemical functionalization, which in turn impart the solubility of CNTs in various solvents. In this study, highly stable aqueous suspensions of MWNTs were obtained by employing both covalent and non-covalent surface functionalization strategies. Using oxidation and polymer wrapping, two differently modified CNTs, i.e. with carboxyl and amine groups, were obtained. The presence of these groups allowed further processing of CNTs into polymer matrices and helped to explore the influence of CNTs surface chemistry on cellular bahavior.

Aiming at the creation of unique architectures comprising biomimetic characteristics, MWNT-based constructs were engineered using different techniques.

For the first time, we report on the fabrication of highly ordered, lightweight matrices with multiwall carbon nanotubes by means of nanosphere lithography and layer-by-layer assembly. The constructs were created on a monolayer of hexagonally ordered polystyrene microspheres. The complete matrices consist of successive layers of polyelectrolytes and carbon nanotubes with a strong interfacial bonding mediated by electrostatic attraction, van der Waals adhesion and mechanical interlocking. The implemented method allows for controlled shaping and guarantees the chemical stability of the self-assembled monolayers. Additionally, the considerable mechanical performance of the constructs is assured by the high concentration and homogenous distribution of the nanotubes within a polymer matrix. The composites - as freestanding matrices - are characterized by a controlled geometry, topography, and chemical composition.

The mechanical properties of MWNT-based matrices were investigated by nanoindentation and nanoscratch tests. The data obtained from nanoindentation experiments show that the presence of carbon nanotubes within the polymeric matrix does not considerably improve the mechanical properties of the respective composite. In general, the elastic modulus and hardness have been found to reflect the mechanical response of the surrounding matrix. Therefore, the mechanical performance of the produced matrices could be altered significantly by changing the polymer composition. The highest values for E_r and H were found for MWNT-based matrices composed of PAH/PSS polyelectrolytes and were 2.23(43) GPa and 0.062(17) GPa, respectively.
Since CNTs exhibit extraordinary axial strength, which plays an important role in the tensile reinforcement action of the composite, their high flexibility and curvy morphology cause modest improvement in the hardness of the polymeric matrices.

The results obtained in nanoscratch tests reveal that carbon nanotube-based matrices display a significant adhesion and friction. The value of the coefficient of friction of the MWNT-PEI/PSS and PEI/PSS has been found to be 0.66(6) and 0.33(6), respectively. The considerable improvement in the scratch resistance arises from the fact that the LbL method, used in the matrices fabrication, ensures a high concentration of CNTs as well as strong interconnectivity between carbon nanotubes and the polymer.

The biocompatibility of MWNT-based structures and cell-surface interaction were assessed using human osteoblast-like cells (HOB-C). In general, we have found excellent cells respond to the micro- and nanotopographical cues present on the surface of MWNT-based matrices. SEM investigation revealed that cells were well-spread and displayed flat morphologies, which strongly suggest the presence of tight junctions and adhesion mechanisms in the nanostructured matrix. Additionally, carbon nanotube constructs exhibited a larger cell area in comparison to the control surface. The adequate cell shape has found its reflection in the cell proliferation rate. The data obtained from the MTT assay showed a significant increase in cell growth for MWNT-based matrices when compared to the glass control surface. This high cell metabolic activity confirms that regular topography with nanosized features has significant effects on cellular behavior. In other words, the carbon nanotubes constructs seem to be suitable, biocompatible cell matrices.

Since the surface chemistry, as well as topography, can influence protein adsorption and biological behavior of cells, we studied the dependence of the carbon nanotube's surface chemistry on bovine serum albumin (BSA) protein adsorption, and subsequently on cell proliferation. The qualitative estimation of BSA adsorption obtained from protein-Coomassie UV-vis absorption spectra together with quantitative information from Bradford protein assay, revealed that surfaces of opposite charge to that of the protein are more effective in promoting protein adsorption. Therefore, a significant difference in BSA adsorption could be observed between multilayered films composed of differently functionalized carbon nanotubes. In general, films made from MWNTs modified with amine groups adsorbed a higher amount of BSA (0.054 ± 0.011 mg/cm^2) compared to MWNTs with carboxyl groups on the surface (0.033 ± 0.008 mg/cm^2).

The interaction and the interfacial dynamics of osteoblast-like cells were also studied on vertically-aligned CNTs. In particular, we focused on manipulating the growth of HOB cells with periodic arrays of carbon nanotubes. From morphological investigations we observed that VACNTs arrays, with a spacing of the nanotubes in the nanometer range, dramatically enhanced cell surface activity. Cell-culture assays on these substrates reveal that the high number of attachment sites (nanotube's tips) promote cell-attachment via cell extensions much better than non-nanostructured substrates. The formation of these cell extensions was closely associated with biomechanical forces exerted by cells on individual nanotubes. Moreover, the immunofluorescent staining for vinculin and actin showed that in contrast to a smooth surface (glass), osteoblast cells cultured on vertically-aligned CNTs display a well developed vinculin plaque-like structure, and highly tensioned actin filaments organized into large numbers of parallel stress fibers. These results indicate an excellent cell adhesion and, together with morphological studies, provide evidence that cells are able to "sense" the nano-geometry of their surrounding environment.

Finally, we have used atomic force microscopy (AFM) to investigate the biocompatibility of CNT-based constructs by studying the adhesion behavior of osteoblast-like cells. Exploiting the ability of AFM to image cells under physiological conditions we were able to determine the cytomechanical properties of living osteoblasts cultured on substrates with randomly-distributed CNTs, cavity-like assembled nanotubes, and smooth glass surface. Experimental data show that the elastic modulus of the osteoblast cells is modulated by the substrate to which they adhere. We have found that the osteoblasts plated on non-nanostructured substrate (glass) have the lowest cell stiffness (3.71 $\pm$1.48 kPa), whereas cells adhered to the cavity-like topography expressed an increased average Young's modulus ($E = 5.43 \pm 2.05$ kPa). Moreover, we observed that an irregular topography has a weaker influence on osteoblast adhesion, which results in a decreased elastic modulus in the case of cells cultured on randomly distributed carbon nanotubes. We believe, that the observed change in the mean Young's modulus is most likely due to actin cytoskeleton organization, which undergo an alternation under the influence of various topographies and surface chemistry.

The correlation of cytomechanical measurements with proliferation and immunofluorescence analysis suggests that nanomechanical measurements of adherent cells have the potential for testing the biocompatibility of materials for tissue engineering application.

The results, presented in this thesis, demonstrate that carbon nanotubes can be successfully employed to fabricate micro-nano-featured matrices for biomedical use. Moreover, these engineered MWNTs structures can be used as favorable substrates for the adhesion and proliferation of osteoblast cells. Although the conducted experiments indicate a non-toxic nature of carbon nanotube-based matrices, there is still much work to be done in establishing their biocompatibility. Therefore, in order to provide a more complete picture of their realistic application in tissue engineering, further *in vivo* studies are required. Last but not least, we believe that the knowledge gained from these studies is of great importance not only for fundamental cell studies, but also for the further design of novel biomaterials.

ACKNOWLEDGMENTS

I would like to end this thesis by acknowledgments the people who contributed to the accomplishment of this work. In the first place, I would like to convey my sincere gratitude to my supervisor Prof. Dr. Michael Giersig for introducing me to the exciting world of nanotechnology and for giving me the opportunity to work in Nanoparticle Technology group at the research center caesar. His guidance and extensive knowledge inspired and enriched my growth as a researcher.

I am particularly thankful to Prof. Dr. Manfred Fiebig for accepting to be a co-referee and for using his precious time to read this thesis and for his critical comments about it.

I gratefully acknowledge Dr. Jose Rojas-Chapana for his valuable advices, supervision during the very early stage of my research, his help in various, not only research related matters, and willingness to teach me Spanish. *Jose, muchas gracias por todo!*

Special thanks go to Dr. Georgios Ctistis for his encouragement, essential correction and constructive comments on this thesis. *Georgios, I am thankful in every possible way!*

I would like to also thank Dr. Michael Hilgendorff who taught me how to work in the chemical lab, and who also took effort in reading and providing me with valuable comments on this thesis.

There are three people I need to mention especially, Dr. Thomas Büsgen, Julia Troszczynska, and Dr. Maciej Olek. I would like to thank them for being very good friends, for their advices, our coffee-conversations and discussions, as well as exiting time we spent together after work. *Thanks guys for your friendship!*

My sincerely thanks go to all current and former members of the NPA's group, who shared with me their scientific knowledge and created a pleasant working atmosphere. In particular, I would like to thank Dr. Suna Giannona and Eva Godehardt (*danke für die Zellkultur!*), Dr. Witold Kandulski, Jolanta Kremer, Ewa Musielak, Claudia Schneider, Piotr Patoka, and Anna Przybyla.

I express my deep gratitude to my parents Zofia Firkowska and Waldemar Firkowski. Their continuous and unconditional support in all I have done till now are the keys of all my achievements. *Dziekuje wam za wszystko!*

Finally, and most importantly I would like to thank Nicolas for his love, support and simply for being with me throughout the journey of this thesis. *Nico*, *te quiero mucho!*

LIST OF FIGURES

PUBLICATIONS AND CONFERENCES

5 PUBLICATIONS IN REFEERED JOURNALS

- **I. Firkowska,** E. Godehardt, M. Giersig, "Interaction between human osteoblast cells and inorganic two-dimensional scaffolds based on multiwalled carbon nanotubes: a quantitative AFM study". *Adv. Funct. Mater.* Accepted

- **I. Firkowska**, S. Giannona, J. Rojas-Chapana, K. Luecke, O. Brustle, M. Giersig, "Biocompatible nanomaterials and nanodevices promising for biomedical applications". In: "Nanomaterials for application in medicine and biology". eds. M. Giersig, G.B. Khomutov, Springer, 1-16 Dordrecht (2008)

- S. Giannona, **I. Firkowska**, J. Rojas-Chapana, M. Giersig, "Vertically aligned carbon nanotubes as cytocompatible material for enhanced adhesion and proliferation of osteoblast-like cells". *J. Nanosci. and Nanotechnol.* **7**, 1679 (2007)

- **I. Firkowska**, M. Olek, N. Pazos-Perez, J. Rojas-Chapana, M. Giersig, "Highly ordered MWNT-based matrices: Topography at the nanoscale conceived for tissue engineering". *Langmuir* **22**, 4527 (2006)

- J. Rojas-Chapana, J. Troszczynska, **I. Firkowska**, C. Morsczeck, M. Giersig, Multiwalled carbon nanotubes for plasmid delivery into Escherichia Coli cells". *Lab on a Chip* **5**, 536 (2005)

3 ORAL PRESENTATIONS AND 1 POSTER

- **I. Firkowska**, E. Godehardt and M. Giersig, "Investigation of biocompatibility of carbon nanotube-based matrices by study the adhesion behavior of osteoblast-like cells". E-MRS Conference, Warsaw, Poland, Sept. 15-19, 2008

- **I. Firkowska**, S. Giannona, J. Rojas-Chapana and M. Giersig, "Bioinspired nano-architectures based on chemically functionalized carbon nanotubes", *TNT Conference*, San Sebastian, Spain, 2007 (*poster*)

- **I. Firkowska**, S. Giannona, J. Rojas-Chapana and M. Giersig, "Qualitative Evaluation of the Response of Human Osteoblast Cells to Nanotopography Surfaces Based on Carbon Nanotubes", *NSTI Conference*, Boston, USA; May 7-11, 2006

- **I. Firkowska**, S. Giannona, J. Rojas-Chapana and M. Giersig, "Development of free-standing films based on carbon nanotubes for tissue engineering", *Euromat Conference*, Prague, Czech Republic, 2005

Erklärung

Hiermit erkläre ich ehrenwörtlich, daß ich die Dissertation “Carbon Nanotube Substrates for Tissue Engineering Applications. Analysis of surface nanotopography, cellular adhesion, and elasticity” selbständig angefertigt und keine anderen als die von mir angegebenen Quellen und Hilfsmittel verwendet habe.

Bonn, September 2008 Izabela Firkowska